MICROELECTROMECHANICAL SYSTEM-BASED WIRELESS MICROSYSTEM FOR BRAIN INTERFACING

by

Lingyao Chen

A dissertation submitted to the faculty of
The University of Utah
in partial fulfillment of the requirements for the degree of

Doctor of Philosophy

Department of Electrical and Computing Engineering

The University of Utah

December 2013

The University of Utah Graduate School

STATEMENT OF DISSERTATION APPROVAL

The dissertation of **Lingyao Chen**

has been approved by the following supervisory committee members:

Massood Tabib-Azar	, Chair	**9/27/2013** Date Approved
Carlos Mastrangelo	, Member	**10/4/2013** Date Approved
Douglas A. Christensen	, Member	**10/4/2013** Date Approved
Rajesh Menon	, Member	**9/27/2013** Date Approved
Bruce Gale	, Member	**9/30/2013** Date Approved

and by **Gianluca Lazzi** , Chair of

the Department of **Electrical and Computer Engineering**

and by David B. Kieda, Dean of The Graduate School.

ABSTRACT

This thesis presents the design, fabrication and characterization of a microelectromechanical system (MEMS) based complete wireless microsystem for brain interfacing, with very high quality factor and low power consumption. Components of the neuron sensing system include TiW fixed-fixed bridge resonator, MEMS oscillator based action-potential-to-RF module, and high-efficiency RF coil link for power and data transmissions.

First, TiW fixed-fixed bridge resonator on glass substrate was fabricated and characterized, with resonance frequency of 100 - 500 kHz, and a quality factor up to 2,000 inside 10 mT vacuum. The effect of surface conditions on resonator's quality factor was studied with 10s of nm Al_2O_3 layer deposition with ALD (atomic layer deposition). It was found that MEMS resonator's quality factor decreased with increasing surface roughness.

Second, action-potential-to-RF module was realized with MEMS oscillator based on TiW bridge resonator. Oscillation signal with frequency of 442 kHz and phase noise of -84.75 dBc/Hz at 1 kHz offset was obtained. DC biasing of the MEMS oscillator was modulated with neural signal so that the output RF waveform carries the neural signal information.

Third, high-efficiency RF coil link for power and data communications was designed and realized. Based on the coupled mode theory (CMT), intermediate resonance coil was introduced and increased voltage transfer efficiency by up to 5 times.

Finally, a complete neural interfacing system was demonstrated with board-level integration. The system consists of both internal and external systems, with wireless powering, wireless data transfer, artificial neuron signal generation, neural signal modulation and demodulation, and computer interface displaying restored neuron signal.

To my parents, mentors, colleagues and friends who have supported me through the journey.

TABLE OF CONTENTS

ABSTRACT iii

ACKNOWLEDGEMENTS viii

1 INTRODUCTION 1

1.1 CMOS Based Neural Interfacing System 2
1.2 Novel MEMS Based Neural Interfacing System 4
1.3 References 8

2 SYSTEM ARCHITECTURE 13

2.1 System Objectives and Architecture 13
2.2 References 19

3 MEMS RESONATOR FABRICATION AND CHARACTERIZATION 20

3.1 Overview 20
3.2 TiW Fixed-Fixed Bridge Fabrication 22
3.3 TiW Fixed-Fixed Bridge Characterization 23
3.4 TiW Fixed-Fixed Bridge Based MEMS Filter 26
3.5 Surface Effect on Q Factor of TiW MEMS Resonator 27
3.6 References 43

4 ACTION-POTENTIAL-TO-RF MODULE 49

4.1 Overview 49
4.2 Action-Potential-to-RF Module with MEMS Oscillator 50
4.3 Tunnel Diode Oscillation Circuit 53
4.4 Action-Potential-to-RF Module with Tunnel Diode Oscillation Circuit 55
4.5 Dynamic Analysis of Relaxation Oscillation Based MEMS DC-to-RF Converters 56
4.6 Experimental Results of MEMS DC-to-RF Converters 61
4.7 References 82

5 RF COIL LINK FOR POWER AND DATA COMMUNICATIONS 85

5.1 Overview 85
5.2 RF Link with Two Coils 87
5.3 RF Link with Three Coils 89
5.4 References 97

6 THE COMPLETE WIRELESS SYSTEM 99

6.1 Wirelessly Powered Neural Interfacing System Based on Tunnel Diode Oscillator 99
6.2 Neural Interfacing System Based on MEMS Oscillator 103
6.3 References 115

7 CONCLUSIONS 116

8 FURTHER WORK 118

8.1 Next-Generation MEMS Device for Action-Potential-to-RF Module 118
8.2 Tunneling Current Based MEMS Amplifier 120
8.3 In Vivo Brain Interfacing System Implantation 122
8.4 References 132

APPENDIX. EXPRESSIONS DERIVATIONS OF MAGNETIC FLUX THROUGH A COIL BY A MAGNETIC DIPOLE 133

ACKNOWLEDGEMENTS

To my supervisor, Prof. Massood Tabib-Azar: I would like to express my greatest gratitude for your constant help and inspiration, in both how to do good research, and how to be a successful man. Thank you for making all this work possible. Thank you.

To my parents: Thank you for raising me up and for your mental support of me, who has been studying away from home. Thank you for your love and care.

To my friends: Thank you for accompanying me through my life in the graduate school. You were always there to comfort my sadness and share my happiness. Thank you guys, for being beside me during this journey.

I want to specially thank Mr. Pradeep Pai for his help in MEMS device fabrication.

CHAPTER 1

INTRODUCTION

Understanding the working principle of the central nervous system of the human body is one of the most difficult problems researchers are facing today. Scientists have been hoping to get a clear picture of the brain, of its working mechanism down to the cellular level. This would help push the limit of both therapeutic and diagnostic brain science that is currently available. A lot of work is being done to decipher the brain signals responsible for muscle control which can provide better control in prosthetics, or even communicate with external electronics. Both noninvasive and invasive techniques have been used in the past.

A widely used noninvasive approach to diagnose and understand brain activities is electroencephalography (EEG), which places numerous electrodes on the scalp to record the brain's electrical signals. This method is relatively easy to implement, but suffers from low signal-to-noise ratio (SNR), low spatial resolution, and complicated and messy wire connections. In order to better understand the human brain's working principles, direct neuron interfacing is required.

A machine-brain interfacing system, unlike EEG, provides a way to look inside the human brain's operating mechanism by implanting a highly integrated system inside the human [1-4]. On one hand, neural signals, for example, neuron action potential signals,

can be sensed by the system and transmitted to the outside world [5-11], to help formatting a complete brain working architecture, and enable controlling of prosthetic human parts (Fig. 1.1), computers or even the outside world. On the other hand, the system can stimulate certain neuron cells to realize neural prostheses, for example auditory and visual prostheses, to restore sight and hearing to people with disabilities [12-19].

Research on the human nervous system dates back to Franklin some 250 years ago, who used electrical stimulation to revive paralyzed limbs. Then from the 1950s, scientists began to use metal wire electrodes for extracellular neural recording, trying to understand working principles of the nervous system on the cellular level. While progress has been achieved in the understanding of behavior of a single neuron and small sensing area, comprehending the system level mechanics requires sensing and stimulating neurons of different parts of the human brain simultaneously [1]. Technologies to enable system level sensing and stimulating were not ready in the 50s. However, with the rapid development of microelectronics design and fabrication process, the technologies are ready to push the limit of brain interfacing. Implantable neural microsystems based on modern integrated circuit and wireless technology are now emerging and are hot topics.

1.1 CMOS Based Neural Interfacing System

An implantable neural microsystem is mainly composed of microelectrodes, neural signal processing circuitry and power and data transmission.

A specifically designed microelectrode is needed to effectively interface with neurons for sensing or stimulation [20]. Utah electrode array (UEA, Fig. 1.2) is one of the most

successful electrodes. Developed by Normann et al. [21-22], UEA is a three-dimensional, 10 × 10 array of tapered silicon electrodes. UEA enables both sensing and stimulation of the central nervous system, acting as the base for lots of neural interfacing system.

An implanted neural interfacing device needs power and a data communication channel with the outside world. A system with implanted battery is a straight forward solution [24-25]. However, the system is bulky and heavy with the battery installed, not to mention the requirement for surgery to replace a dead battery. For bidirectional control and data communication, wired connection is one approach [26]. However, transcutaneous wires are subject to infection, noise interferences and inability for a free, mobile subject. Therefore, microsystems with wireless powering and wireless communication channels become the standard for neural interfacing research.

There has been lots of work and efforts devoted into building effective and efficient wireless neuron interfacing systems. Najafi et al. [5-16, 27-32] realized both battery powered and wireless powered microsystems, for neural signal sensing (Fig. 1.3) and stimulating. They developed the CMOS based 64-channel neural processing unit (NPU) to achieve signal preconditioning, amplifying and band-pass filtering [5]. Harrison et al. [33-38] realized an integrated circuit (INI chip, Fig. 1.4) based wireless neuron recording system with the Utah Electrode Array for neuron signal accessing. The INI chip contains a neural amplifier, ADC, FSK circuits, microcontrollers and so on, based on CMOS technology. The system has been tested with cat auditory cortex and flying insects. They have also studied long term stability and recording longevity of the UEA based implanted neural interface [39].

1.2 Novel MEMS Based Neural Interfacing System

The two challenges of the implanted neural interfacing system are: 1) stringent limitation on power consumption (high power consumption can easily kill neuron cells) and 2) limit on internal system dimensions. Wireless communication systems, like the neural interfacing system, require frequency selective components of very high quality factor Q and exceptional stability. The above-mentioned works are all based on the CMOS system, and frequency selectivity of oscillation output in the CMOS based neuron interfacing system is determined by LC circuit, which has a very low quality factor, not to mention the size the LC components occupy. Therefore, in order to increase the quality factor Q, decrease device footprint and power consumption, a neural interfacing system with a microelectromechanical system can be a better solution.

Microelectromechanical system (MEMS) first appeared in the 1980s, which combines mechanical moving parts with electronics, and manufactured from microfabrication processes. It takes advantage of coupling and interaction between domains such as electrical, mechanical, thermal, optical and even magnetic. MEMS based frequency selective components (e.g., filters and oscillators) have been proven to have a much higher quality factor Q (therefore much higher stability), and consume very low power (virtually zero leakage current due to mechanical separation). Furthermore, MEMS devices are compatible with CMOS integration, and possess very small device size [40-45]. Hence, a microelectromechanical system is the best candidate for neural interfacing system development.

To take advantage of MEMS technology, this dissertation realized a complete MEMS system for neuron signal sensing, featuring 1) design and fabrication of MEMS resonator

of TiW fixed-fixed bridge on glass substrate, with the effect of surface conditions on its quality factor studied; 2) novel neuron action-potential-to-RF module, based on MEMS feedback oscillator with high quality factor Q and small device footprint; 3) high-efficiency inductive powering link utilizing intermediate resonant coil. The system is capable of retrieving neuron firing information from multiple channels spread across the brain, and transmitting the data simultaneously without interference.

Fig. 1.1 Possible brain to machine interfacing with prosthetic arms.

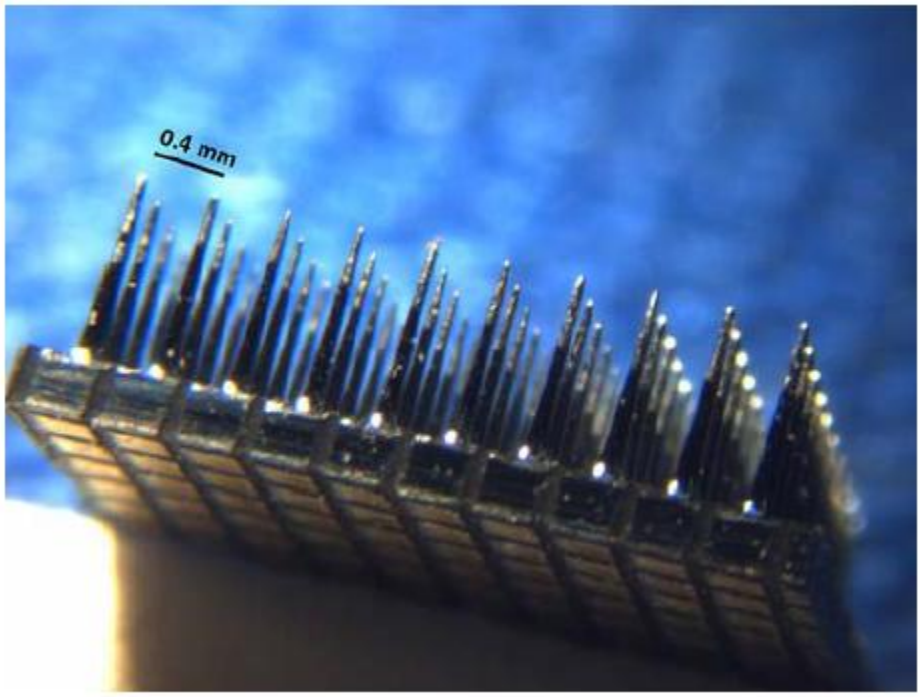

Fig. 1.2. Picture of the Utah Electrode Array (UEA). Copyright © 2009 SPRINGER [23]

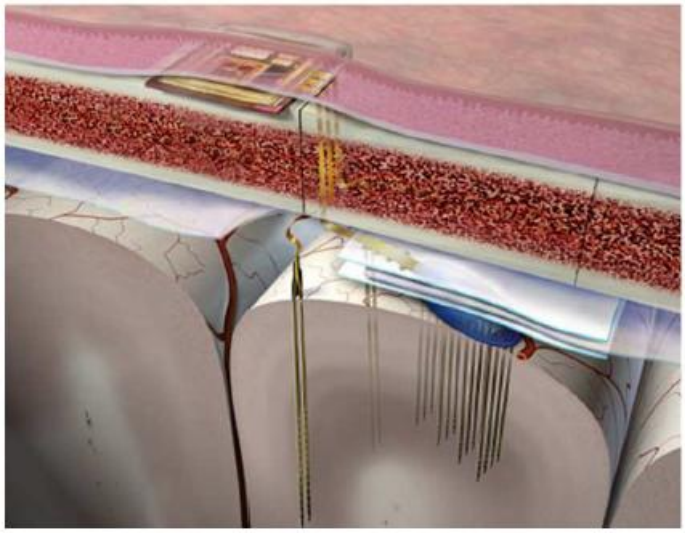

Fig. 1.3. The neural recording microsystem and its implant configuration by Najafi et al. Copyright © 2009 IEEE [5]

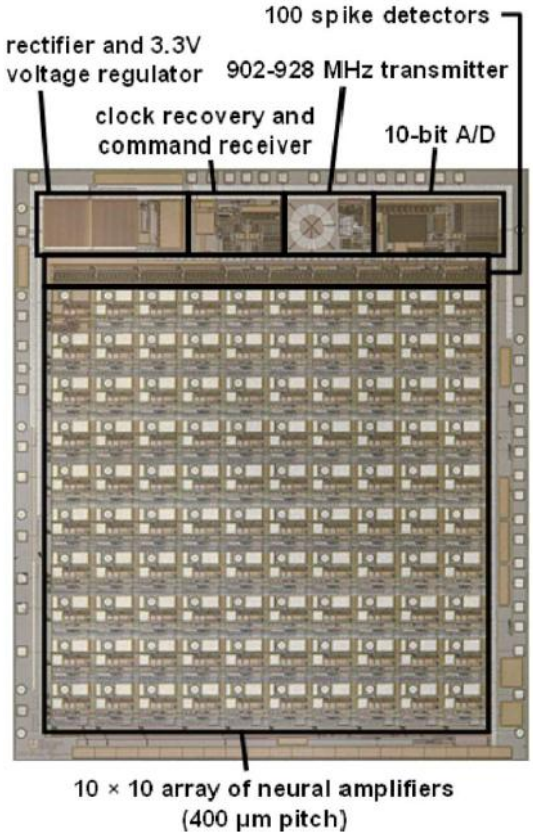

Fig. 1.4. INI3 neural recording chip by Harrison et al. Copyright © 2009 IEEE [34]

1.3 References

[1] K.D. Wise, A.M. Sodagar, Y. Yao, M.N. Gulari, G.E. Perlin and K. Najafi, "Microelectrodes, microelectronics, and implantable neural microsystems," *Proceedings of the IEEE*, Vol. 96, No. 7, pp. 1184-1202, 2008.

[2] K.D. Wise, D.J. Anderson, J.F. Hetke, K, D.R. Kipke and K. Najafi, "Wireless implantable microsystems: high-density electronic interfaces to the nervous system," *Proceedings of the IEEE*, Vol. 92, No. 1, pp. 76-97, 2004.

[3] K.D. Wise, "Wireless integrated microsystems: coming breakthroughs in health care," *Technical Digest - International Electron Devices Meeting, IEDM*, San Francisco, CA, USA, pp. 419-422, 2006.

[4] K.D. Wise, "Wireless integrated microsystems: wearable and implantable devices for improved health care," *TRANSDUCERS 2009 - 15th International Conference on Solid-State Sensors, Actuators and Microsystems*, Denver, CO, USA, pp. 1-8, 2009.

[5] A.M. Sodagar, G.E. Perlin, Y. Yao, K. Najafi and K.D. Wise, "An implantable 64-channel wireless microsystem for single-unit neural recording," *IEEE Journal of Solid-State Circuits*, Vol. 44, No. 9, pp. 2591-2604, 2009.

[6] T. Akin, K. Najafi and R.M. Bradley, "A wireless implantable multichannel digital neural recording system for a micromachined sieve electrode," *IEEE Journal of Solid-State Circuits*, Vol. 33, Issue 1, pp. 109-118, 1998.

[7] A. Borna and K. Najafi, "A low power, low voltage, user-programmable, wireless interface for reliable neural recording," *2011 IEEE Biomedical Circuits and Systems Conference*, San Diego, CA, USA, pp. 77-81, 2011.

[8] A. Borna, T. Marzullob, G. Gage and K. Najafi, "A small, light-weight, low-power, multichannel wireless neural recording microsystem," *Proceedings of the Annual International Conference of the IEEE Engineering in Medicine and Biology Society*, Minneapolis, MN, USA, pp. 5413-5416, 2009.

[9] A.M. Sodagar, G.E. Perlin, Y. Yao, K.D. Wise and K. Najafi, "An implantable microsystem for wireless multi-channel cortical recording," *TRANSDUCERS 2007 - 14th International Conference on Solid-State Sensors, Actuators and Microsystems*, Lyon, France, Vol. 1, pp. 69-72, 2007.

[10] A.M. Sodagar, G. E. Perlin, Y. Yao, K. Najafi and K. D. Wise, "Chronic neural recording with a 64-channel cortical microsystem," *Proceedings of the 3rd International IEEE EMBS Conference on Neural Engineering*, Kohala Coast, HI, USA, pp. 402-405, 2007.

[11] A.M. Sodaga, K.D. Wise and K. Najafi, "A wireless implantable microsystem for multichannel neural recording," *IEEE Transactions on Microwave Theory and Techniques*, Vol. 57, No. 10, pp. 2565-2573, 2009.

[12] M. Ghovanloo and K. Najafi, "A wireless implantable multicahnnel microstimulating system-on-a-chip with modular architecture," *IEEE Transactions on Neural Systems and Rehabilitation Engineering*, Vol. 15, No. 3, pp. 449-457, 2007.

[13] M. Ghovanloo and K. Najafi, "A modular 32-site wireless neural stimulation microsystem," *IEEE Journal of Solid-State Circuits*, Vol. 39, No. 12, pp. 2457-2466, 2004.

[14] B. Ziaie, M.D. Nardin, A.R. Coghlan and K. Najafi, "A single-channel implantable microstimulator for functional neuromuscular stimulation," *IEEE Transactions on Biomedical Engineering*, Vol. 44, No. 10, 1997.

[15] K. Najafi and M. Ghovanloo, "A multichannel monolithic wireless microstimulator," *Proceedings of the Annual International Conference of the IEEE Engineering in Medicine and Biology Society*, San Francisco CA, USA, pp. 4197-4200, 2004.

[16] M. Ghovanloo, K.J. Otto, D.R. Kipke and K. Najafi, "In vitro and in vivo testing of a wireless multichannel stimulating telemetry microsystem," *Proceedings of the Annual International Conference of the IEEE Engineering in Medicine and Biology Society*, San Francisco, CA, USA, pp. 4294-4297, 2004.

[17] R.A. Normann, D. McDonnall, G.A. Clark, R.B. Stein and A. Branner, "Physiological activation of the hind limb muscles of the anesthetized cat using the Utah slanted electrode array," *Proceedings of the International Joint Conference on Neural Networks 2005*, Montreal, Que., Canada, Vol. 5, pp. 3103-3108, 2005.

[18] W. Wang, H. Hao, B. Ma, F. Liu, C. Hu, and L. Li, "Design and analysis of a transcutaneous telemetry device for brain stimulator," *Proceedings of the Annual International Conference of the IEEE Engineering in Medicine and Biology Society*, Minneapolis, MN, USA, pp. 2153-2156, 2009.

[19] X. Ye, P. Wang, J. Liu, S. Zhang, J. Jiang, Q. Wang, W. Chen and X. Zheng, "A portable telemetry system for brain stimulation and neuronal activity recording in freely behaving small animals," *Journal of Neuroscience Methods*, Vol. 174, pp. 186-193, 2008.

[20] D. Egert, R.L. Peterson and K. Najafi, "New class of chronic recording multichannel neural probes with post-implant self-deployed satellite recording sites," *TRANSDUCERS 2011 - 16th International Conference on Solid-State Sensors, Actuators and Microsystems*, Beijing, China, pp. 958-961, 2011.

[21] P.K., Campbell, K.E. Jones, R.J. Huber, K.W. Horch and R.A. Normann, "A silicon-based, three-dimensional neural interface: manufacturing processes for an intracortical electrode array," *IEEE Transactions on Biomedical Engineering*, Vol. 38, No. 8, pp. 758-768, 1991.

[22] R.A. Normann, P.K. Campbell and K.E. Jones, "Micromachined, silicon based electrode arrays for electrical stimulation of or recording from cerebral cortex," *Proceedings of the IEEE International Conference on Micro Electro Mechanical Systems (MEMS),* Nara, Japan, pp. 247-252, 1991.

[23] S. Kim, R. Bhandari, M. Klein, S. Negi, L. Rieth, P. Tathireddy, M. Toepper, H. Oppermann and F. Solzbacher, "Integrated wireless neural interface based on the utah electrode array," *Biomedical Microdevices*, Vol. 11, No. 2, pp. 453-466, 2009.

[24] F. Albano, Y.S. Lin, D. Blaauw, D.M. Sylvester, K.D. Wise and A.M. Sastry, "A fully integrated microbattery for an implantable microelectromechanical system," *Journal of Power Sources*, Vol. 185, No. 2, pp. 1524-1532, 2008.

[25] F. Albano, M.D. Chung, D. Blaauw, D.M. Sylvester, K.D. Wise and A.M. Sastry, "Design of an implantable power supply for an intraocular sensor, using POWER (power optimization for wireless energy requirements)," *Journal of Power Sources*, Vol. 170, No. 1, pp. 216-224, 2007.

[26] Y. Yao, M.N. Gulari, B. Casey, J.A. Wiler and K.D. Wise, "Silicon microelectrodes with flexible integrated cables for neural implant applications," *Proceedings of the 3rd International IEEE EMBS Conference on Neural Engineering*, Kohala Coast, HI, USA, pp. 398-401, 2007.

[27] A.M. Sodagar, K.D. Wise and K. Najafi, "A fully-integrated mixed-signal neural processor for implantable multi-channel cortical recording," *IEEE Transactions on Biomedical Engineering*, Vol. 54, No. 6, pp. 1075-1088, 2007.

[28] M. Ghovanloo and K. Najafi, "A wideband frequency-shift keying wireless link for inductively powered biomedical implants," *IEEE Transactions On Circuits and Systems I: Fundamental Theory and Applications*, Vol. 51, No. 12, pp. 2374-2383, 2004.

[29] P. Mohseni, K. Najafi, S. J. Eliades and X. Wang, "Wireless multichannel biopotential recording using an integrated FM telemetry circuit," *IEEE Transactions on Neural Systems and Rehabilitation Engineering*, Vol. 13, No. 3, pp. 263-271, 2005.

[30] P. Mohseni and K. Najafi, "A 1.48-mW low-phase-noise analog frequency modulator for wireless biotelemetry," *IEEE Transactions on Biomedical Engineering*, Vol. 52, No. 5, pp. 938-943, 2005.

[31] G.E. Perlin and K.D. Wise, "An ultra compact integrated front end for wireless neural recording microsystems," *Journal of Microelectromechanical Systems*, Vol. 19, No. 6, pp. 1409-1421, 2010.

[32] G.E. Perlin, A.M. Sodagar and K.D. Wise, "Neural recording front-end designs for fully implantable neuroscience applications and neural prosthetic microsystems," *Proceedings of the Annual International Conference of the IEEE Engineering in Medicine and Biology Society*, New York City, NY, USA, pp. 2982-2985, 2006.

[33] B.K. Thurgood, D.J. Warren, N.M. Ledbetter, G.A. Clark and R.R. Harrison, "A wireless integrated circuit for 100-channel charge-balanced neural stimulation," *IEEE Transactions on Biomedical Circuits and Systems*, Vol. 3, No. 6, pp. 405-414, 2009.

[34] R.R. Harrison, R.J. Kier, C.A. Chestek, V. Gilja, P. Nuyujukian, S. Ryu, B. Greger, F. Solzbacher and K.V. Shenoy, "Wireless neural recording with single low-power integrated circuit," *IEEE Transactions on Neural Systems and Rehabilitation Engineering*, Vol. 17, No. 4, pp. 322-329, 2009.

[35] R.R. Harrison, P.T. Watkins, R.J. Kier, R.O. Lovejoy, D.J. Black, B. Greger and F. Solzbacher, "A low-power integrated circuit for a wireless 100-electrode neural recording system," *IEEE Journal of Solid-State Circuits*, Vol. 42, No. 1, pp. 123-133, 2007.

[36] R.R. Harrison, H. Fotowat, R. Chan, R.J. Kier, R. Olberg, A. Leonardo and F. Gabbiani, "Wireless neural/EMG telemetry systems for small freely moving animals," *IEEE Transactions on Biomedical Circuits and Systems*, Vol. 5, No. 2, pp. 103-111, 2011.

[37] S.J. Thomas, R.R. Harrison, A. Leonardo and M.S. Reynolds, "A battery-free multichannel digital neural/EMG telemetry system for flying insects," *IEEE Transactions on Biomedical Circuits and Systems*, Vol. 6, No. 5, pp. 424-436, 2012.

[38] G.A. Clark, N.M. Ledbetter, D.J. Warren and R.R. Harrison, "Recording sensory and motor information from peripheral nerves with utah slanted electrode arrays," *Proceedings of the Annual International Conference of the IEEE Engineering in Medicine and Biology Society*, Boston, MA, USA, pp. 4641-4644, 2011.

[39] A. Sharma, L. Rieth, P. Tathireddy, R. Harrison, H. Oppermann, M. Klein, M. Topper, E. Jung, R. Normann, G. Clark and F. Solzbacher, "Long term in vitro functional stability and recording longevity of fully integrated wireless neural interfaces based on the utah slant electrode array," *Journal of Neural Engineering*, Vol. 8, No. 4, pp. 1-6, 2011.

[40] C. Nguyen, "Microelectromechanical devices for wireless communications," *Proceedings of the IEEE International Conference on Micro Electro Mechanical Systems (MEMS)*, Heidelberg, Germany, pp. 1-7, 1998.

[41] C. Nguyen, "MEMS technology for timing and frequency control," *IEEE Transactions on Ultrasonics, Ferroelectrics, and Frequency Control*, Vol. 54, No. 2, pp. 251-270, 2007.

[42] C. Nguyen, "RF MEMS in wireless architectures," *Proceedings - Design Automation Conference*, Anaheim, CA, USA, pp. 416-420, 2005.

[43] C. Nguyen, "Vibrating RF MEMS for next generation wireless applications," *Proceedings of the IEEE 2004 Custom Integrated Circuits Conference*, Orlando, FL, USA, pp. 257-264, 2004.

[44] C. Nguyen, "Integrated micromechanical circuits for RF front ends," *Proceedings of the 36th European Solid-State Device Research Conference*, Montreaux, Switzerland, pp. 7-16, 2006.

[45] C. Nguyen, "Vibrating RF MEMS technology: fuel for an integrated micromechanical circuit revolution," *TRANSDUCERS 2005 - 13th International Conference on Solid-State Sensors, Actuators and Microsystems*, Seoul, South Korea, pp. 243-246, 2005.

[46] R.A. Normann and A. Branner, "Multichannel, neural interface for the peripheral nervous system," *Proceedings of the IEEE International Conference on Systems, Man and Cybernetics*, Tokyo, Japan, Vol. 4, pp. 370-375, 1999.

[47] P.J. Rousche and R.A. Normann, "Chronic recording capability of the Utah intracortical electrode array in cat sensory cortex," *Journal of Neuroscience Methods*, Vol. 82, No. 1, pp. 1-15, 1998.

[48] K. Murari, C. M. Sauer, M. Stanacevic, G. Cauwenberghs and N. Thakor, "Wireless multichannel integrated potentiostat for distributed neurotransmitter sensing," *Proceedings of the Annual International Conference of the IEEE Engineering in Medicine and Biology Society*, Shanghai, China, pp. 7329-7332, 2005.

[49] C.K. Liang, J.J. Chen, C.L. Chung, C.L. Cheng and C.C. Wang, "An implantable bi-directional wireless transmission system for transcutaneous biological signal recording," *Physiological Measurement*, Vol. 26, No. 1, pp. 83-97, 2005.

CHAPTER 2

SYSTEM ARCHITECTURE

The analog MEMS based brain interfacing system is divided into two major parts: external systems and internal systems. Fig 2.1 shows the overview schematic of the system. The internal systems are arrays of very small transmitters deployed inside different locations inside the brain, having access to neurons in different brain parts. Each internal system operates at its own frequency channel, enabling a large number of internal systems to transmit data simultaneously. The external system, on the other hand, resides outside the brain, providing power to the internal systems, and at the same time, receiving neuron firing data from the internal systems, demodulating it and exhibit the signal on the computer interface.

2.1 System Objectives and Architecture

There are two methods to detect neuron firing signals: intracellularly and extracellularly [1]. Intracellular means “inside the cell,” in which neuron spikes will be recorded with electrodes penetrating the cell wall, giving signal amplitude of 100 mV. However, the penetrating electrode will kill the cell within a few minutes, therefore is not suitable for implantation. Extracellular means “outside the cell,” and this method puts

microelectrode a few tens of μm away, producing potential of 50 – 500 μV. This method of neuron spikes recording will be used for our brain interfacing system.

The duration of each neuron spike is usually 500 - 1000 μs, and an active neuron usually generates 10 – 100 spikes per second, i.e., 10 – 100 ms separation between adjacent pulses. Typical neuron action potential signals are shown in Fig. 2.2 (top waveform). As can be seen, a neural signal has an intrinsic negative biasing value, which is called the resting potential. During the firing phase, the neural signal rises, falls, undershoots and then restores to the resting potential. The brain interfacing system first amplifies and biases the neural signal, then uses it to modulate RF carrier signal. The RF signal, which contains neuron signal information (Fig. 2.2 bottom waveform), is then received by the external system outside the brain, and is demodulated to recover the desired neuron pulse waveform. The carrier signal frequency is unique for each internal system, which eliminates channel interferences and enables simultaneous data transceiving.

Detailed schematic of the brain interfacing system is shown in Fig. 2.3. For illustration purposes, only one internal system is depicted. The neurons are accessed with microelectrodes, and their firing signals are amplified by neuron amplifiers. Action potential to the RF module is driven by the amplified neuron firing pulses and produces neuron signal modulated RF signals. Combined RF signals from different internal systems, with different frequency channels, are inductively coupled through the data link to the external system. The signals are amplified, filtered, demodulated and then displayed on the computer interface for each internal system (i.e., each channel).

In the other part of the external system, an RF source drives a power coil, and inductively couples the power signal to the internal systems through the power link. The power signal is then regulated and powers up the neuron amplifiers. The frequency of the power link will be relatively low (tens of kHz), and the same channel is shared by all internal systems. The data link, on the other aspect, has different channels for each internal system, as discussed before, with much higher frequencies (hundreds of kHz to MHz).

The thesis is organized as the following:

- Chapter 3 talks about TiW MEMS resonator fabrication and characterization, acting as MEMS filter and the base of MEMS oscillator. The effect of surface conditions on its quality factor was studied with 10s nm Al_2O_3 layer deposition with ALD.
- Chapter 4 describes the action-potential-to-RF module, which transforms the neuron firing pulses to transmittable RF signals. One approach is based on a MEMS oscillator with a high quality factor and small device footprint. The other approach uses a tunnel diode oscillation circuit.
- Chapter 5 presents the design and realization of high-efficiency RF coil links for power and data transmission, taking advantage of the mediating resonant coils for telemetry efficiency enhancing.
- Chapter 6 presents the results of a board-level integration of the complete neural interfacing system, which consists of both internal and external systems, with wireless powering and data transfer, artificial neuron signal generation, neural

signal modulation and demodulation, and computer interface displaying restored neuron signal.

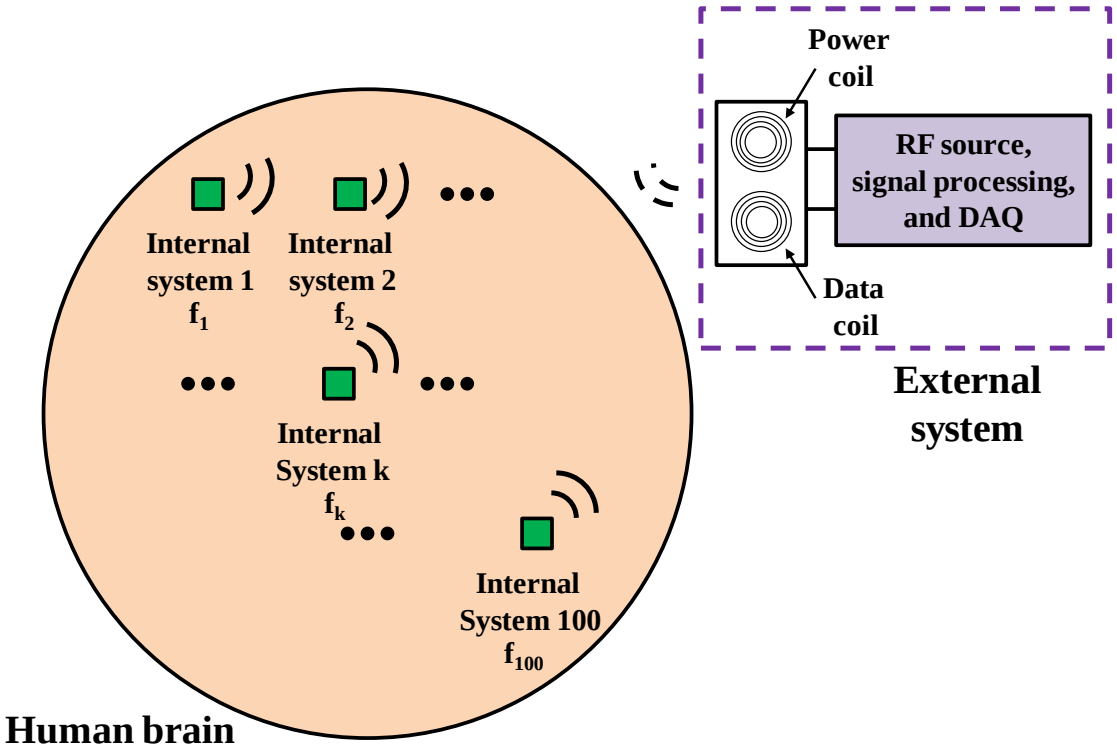

Fig. 2.1. Schematics of the overview structure of the brain interfacing system.

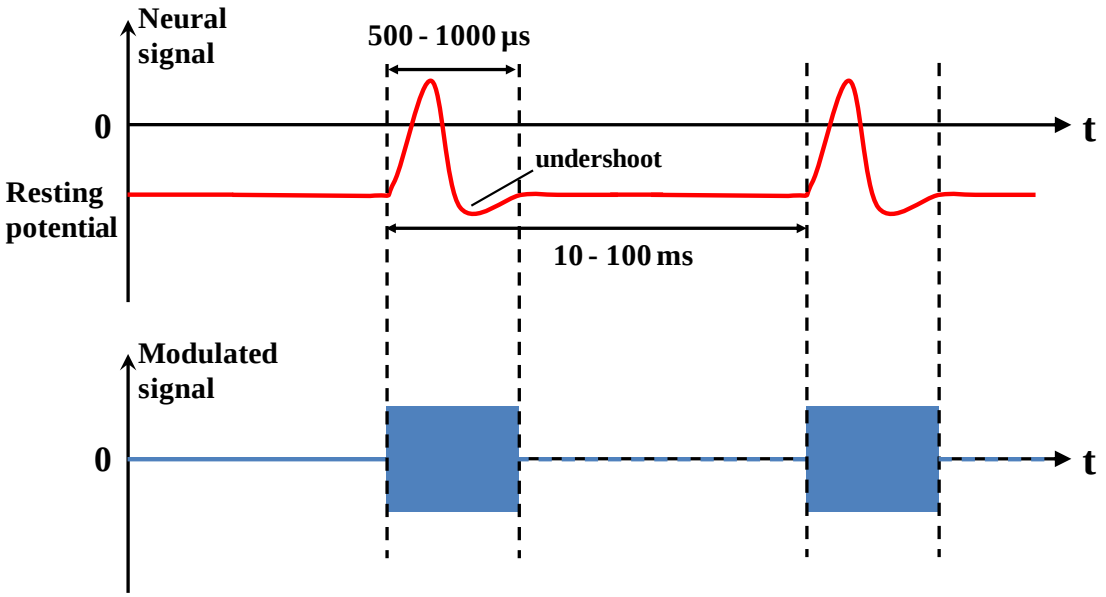

Fig. 2.2. Typical neuron firing signal and neural signal modulated RF signal.

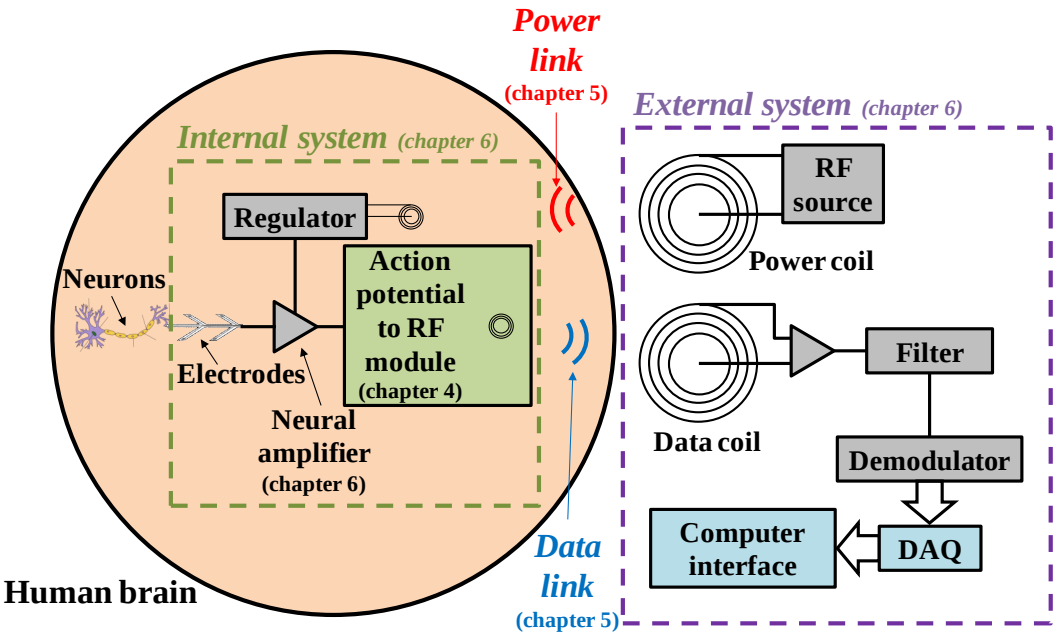

Fig. 2.3. Schematics of the structure of the brain interfacing system, with details of the insides of the internal and external systems.

2.2 References

[1] R.R. Harrison, P.T. Watkins, R.J. Kier, R.O. Lovejoy, D.J. Black, B. Greger and F. Solzbacher, "A low-power integrated circuit for a wireless 100-electrode neural recording system," *IEEE Journal of Solid-State Circuits*, Vol. 42, No. 1, pp. 123-133, 2007.

CHAPTER 3

MEMS RESONATOR FABRICATION AND CHARACTERIZATION

3.1 Overview

Electrical resonators can be found in almost all aspects of electrical devices and systems, working as filters, oscillators and timing references. Quartz resonators have dominated the regime of accurate frequency generation in the 20th century. It has excellent temperature stability and phase noise performance due to its mechanical and piezoelectric properties. However, quartz resonators suffer from their inability for Si wafer integration, lack of flexible frequency programmability and relatively high cost. MEMS technology, which appeared a few decades ago, can successfully counter all these drawbacks of quartz crystal. MEMS resonators are small, programmable, easily integrated with CMOS on silicon wafer, and inexpensive. They can achieve a much higher quality factor than quartz, and can be used as very sensitive sensors, besides acting as timing references [1].

Research on MEMS resonators has resulted in devices with a variety of different working principles. A MEMS resonator is usually made of a mechanical structure with its intrinsic resonance frequency, along with driving, sensing and DC biasing circuitry. The

most common mechanical structure is lateral air-gap fixed-fixed bridges [2]. To increase the quality factor and increase signal amplitude, very thick silicon or polysilicon bridges were fabricated with the HARPSS (high aspect-ratio combined poly and single-crystal silicon) technique to achieve deep etching, with reported Q of more than 100,000 [3-13]. Other commonly used mechanical structures are microdisk [14-23], ring [24-27] and hemisphere [28]. Materials such as silicon, SiGe, diamond, AlN, nickel are used, and a different mechanical vibration mode of the structure is utilized to realize frequency selectivity. Another major category of MEMS resonator is based on bulk acoustic wave (BAW) and Lamb wave generation, transmission and detection [29-35]. MEMS based bulk acoustic-wave resonators (BAR) and thin-film acoustic-wave resonators (FBAR) have been realized for RF frequency filtering and oscillation. A novel MEMS resonator with thermal actuation has also been demonstrated [36]. MEMS resonators that utilize charge trapping to eliminate DC voltage biasing have been realized as well [37-38].

MEMS bandpass filters have been realized based on electrically coupling of individual MEMS resonators, achieving outstanding filtering characteristics of very high quality factor and sharp roll-off, with the ability of integration on-chip [39-46].

For this dissertation work, novel TiW fixed-fixed bridge air-gap MEMS resonator on glass substrate was fabricated and characterized. The effect of surface conditions on the quality factor of the resonators was studied with atomic layer deposition (ALD). The fabricated TiW microbridge can be easily converted into MEMS filters to be used for neuron signal modulated RF signal filtering in the external module of the neuron interfacing system.

3.2 TiW Fixed-Fixed Bridge Fabrication

MEMS fixed-fixed bridges were fabricated with TiW on glass substrate. Glass substrate was used to eliminate possible silicon substrate leakage. Metal, instead of silicon, was used as the material for both bridge and electrode to make the process simple and cheap. TiW (with 90% of W and 10% of Ti) has very high density (14.5×10^3 kg/m^3), and very high Young's modulus (382 GPa), and was chosen to create very stiff microbridges, with high resonance frequency.[1]

The devices were fabricated on a 4" glass wafer. A fresh glass wafer was cleaned in a piranha bath to remove any surface contaminants. A 30 nm layer of HfO_2 was deposited on the glass wafer using the Cambridge Fiji F200 Atomic Layer Deposition system from Cambridge Nanotech. This served as an etch stop during sacrificial release. A 1 μm thick layer of PECVD SiO_2 was then deposited, using the Plasmalab 80 plus system from Oxford Instruments, on top of the HfO_2 layer as the sacrificial layer. An alloy of titanium (10%)/tungsten (90%) was used as the device layer. This material was deposited by sputtering in a T-M Vacuum sputtering system, to form 1 μm thick layer. A 100 nm thick layer of Cr was then sputtered on top of the TiW layer to form a hard mask for device layer patterning. The mask features were photolithographically transferred onto the wafer through S1813 photoresist from Shipley. The Cr layer was then patterned by wet etching using CR-17 etchant from Cyantek Corp. The device layer was patterned by dry etching in Plasmalab 80 plus RIE system using a mixture of SF_6 (10 sccm) and Ar (25 sccm) gases at a pressure of 10mT and an RF power of 200 W. The etch process had to be timed since the SiO_2 sacrificial layer also gets etched in SF_6. The devices were finally released

[1] The microbridge was fabricated by Mr. Pradeep Pai.

in BOE made up of 1:6 mixture of HF and NH_4F, respectively. To minimize the stiction problem due to surface tension, the devices were immersed in methanol after rinsing in deionized (DI) water following the BOE etch. The fabrication process is shown in Fig. 3.1.

Fig. 3.2 shows SEM images of the microbridges. Lengths of 100 μm, 200 μm, 300 μm, 500 μm and 1000 μm bridges were fabricated. For all bridges, width and thickness are fixed at 5 μm and 1 μm, respectively. Each bridge is flanked by two electrodes (same material of TiW) laterally with gap size of 1 μm (Fig. 3.2b). The bridge is floating above the glass substrate and free to move.

3.3 TiW Fixed-Fixed Bridge Characterization

Resonance characteristics of the microbridges were measured with set-up as shown in Fig. 3.3. Network analyzer (Agilent 4395A)'s RF output transmits AC signal to the left electrode of the microbridge, while a DC voltage (provided by Keithley 237 Source Measure Unit, or SMU) is applied to the bridge. The bridge is electrostatically actuated with the superposition of AC and DC signals, vibrating laterally with the AC frequency. The bridge's vibration creates a changing capacitor with the right electrode, and along with the DC supply, generates changing current. The current value is very small (~ nA) due to the very small gap capacitance. Nevertheless, the small current can be detected with a low-noise preamplifier (SR560), thanks to its 100 MΩ input impedance. The output of the amplifier is then fed back into the network analyzer for detection. The microbridges were put inside a vacuum chamber for different gas pressures. All instruments, including the vacuum chamber, share the same ground. By sweeping the AC

frequency through the network analyzer, resonance characteristics of the microbridge can be obtained.

Resonances of the microbridges were obtained for different V_{DC} biasings. Fig. 3.4 shows the resonance peaks for a 300 μm long bridge, under 10 mTorr vacuum conditions. It can be seen that bridge resonance frequency f_0 shift with V_{DC}: higher V_{DC} generates lower f_0. This confirms the theory of spring softening [47-49]. Resonant frequencies f_0 and quality factors Q were plotted as a function of V_{DC} biasing, as shown in Fig. 3.5. It can be observed that f_0 decreases almost linearly with V_{DC}, with tuning sensitivity of 0.286 kHz/V. The Q, on the other hand, has a peak at V_{DC} = 26 V. For lower V_{DC}, both sensing and driving effect of the microbridges are weakened, leading to lower Q. For higher V_{DC}, the microbridge becomes "softened," creating lower Q as well. Therefore, an optimal V_{DC} exists for maximum Q. The maximum Q is around 2,000 for this particular 300 μm long microbridge, when V_{DC} is 26 V.

According to static analysis of MEMS mechanical devices [50], the bridge's resonance frequency is

$$f_0 = \frac{1}{2\pi}\sqrt{\frac{k}{m}} = \frac{1}{2\pi}\sqrt{\frac{32EW^2}{\rho L^4}} \tag{3.1}$$

where k, m, E, ρ, W, L are the bridge's spring constant, mass, Young's modulus, density, width and length, respectively. Substituting parameters of the 300 μm bridge into the equation, it was found that its theoretical resonance frequency is 257 kHz, with no DC bias. The reasons for the discrepancy between experimental and theoretical results are 1) residual stress on the bridge due to fabrication process; 2) deviation of fabricated bridge dimension from design values.

The microbridges were tested under different vacuum conditions. Fig. 3.6 shows the results of resonant frequency and Q versus air pressures, for the same 300 μm long bridge. It can be seen that resonant frequency f_0 remains almost fixed from 10 μTorr up to one atmosphere. The Q remains almost constant from 10 μTorr to 100 mTorr, then drops to nearly 1 at one atmosphere. This means that the MEMS microbridge does not require very demanding vacuum conditions for proper functioning.

The above resonance characteristics were found to be reproducible. The 3 dB bandwidth variation is in the order of Hz, and resonance frequency variation is in the order of 100 Hz.

The resonance of the microbridges could be characterized with another method. Instead of using both electrodes for driving and sensing, only one electrode was utilized for driving and sensing. Fig. 3.7 shows the experimental set-up. A Mini-Circuits bias-tee was used to apply DC bias to the RF output of the network analyzer. The microbridge was actuated with both AC and DC upon the gap, causing it to vibrate. The changing gap capacitance along with DC biasing creates changing current, which is then amplified by the SR560 amplifier and fed back into the network analyzer.

Resonance with the same microbridge device was characterized with this set-up. Fig. 3.8 shows the resonance spectrum with different DC biasing, which is similar to the results from double electrode driving/sensing. Fig. 3.9 shows the tuning effect of DC biasing on resonant frequency f_0 and Q. It can be seen that f_0 decreases with higher V_{DC}, and Q has a peak for an optimal V_{DC}, as before. For the same 300 μm long microbridge, the optimal V_{DC} is still around 26 V, only the maximum Q is smaller than the double electrode testing.

The microbridge was again tested under different vacuum conditions, for single bridge driving/sensing. Fig. 3.10 shows the results of resonant frequency and Q versus air pressures, for the same 300 μm long bridge. As before, the resonant frequency f_0 remains almost fixed from 10 μTorr up to one atmosphere, while the Q remains almost constant from 10 μTorr to 100 mTorr, then drops to nearly 1 at one atmosphere.

3.4 TiW Fixed-Fixed Bridge Based MEMS Filter

A MEMS filter was realized with the fabricated fixed-fixed bridge (Fig. 3.11). Two signals with slightly different frequencies were added up with an op-amp adder (Fig. 3.11a), with unity gain. The combined signal was then connected to the left electrode of the MEMS device, while the center bridge and right electrode were connected to DC biasing and SR560 LNA, respectively (Fig. 3.11b). The spectra of the resulting output was shown in the spectrum analyzer. The DC biasing determines the frequency component to the transmitted through the MEMS device, acting as a bandpass filter.

The resonance of the MEMS microbridge versus V_{DC} is shown in Fig. 3.12. The output signal characteristics are shown in Fig. 3.13, in which the filtered amplitudes of the two frequency components are shown with different V_{DC} values. It can be seen that the two signals can be differentiated by tuning DC biasing to either 60.0 V or 62.6 V. Signal output for 189 kHz is a little larger than that of 190 kHz due to the larger V_{DC} for 189 kHz tuning. Insertion loss (IL) for 189 kHz signal is larger than 1 (0.11 dB), which is the result of SR560 amplification. As can be observed in Fig. 3.13, at a resonance of one frequency, signal output from the other frequency has a small peak as well. This is the result of strong coupling at bridge mechanical resonance for all signals (large mechanical

movement and smaller gap size). These results and characteristics are summarized in Table 3.1.

3.5 Surface Effect on Q Factor of TiW MEMS Resonator

Quality factor Q of the microresonators is the ratio of energy stored to energy dissipated in the system. Stable resonator performance calls for high Q, and correspondingly, lower energy dissipation. Lots of work has been done in the study of sensitivity and limitation of quality factor of MEMS devices [51-61]. Common loss mechanisms for MEMS devices include clamping loss, thermoelastic dissipation (TED), surface effects and so on [54-55, 59]. For the fabricated TiW microbridges, ratios of length/thickness and length/width are very large, meaning that clamping loss and TED can be insignificant in the total energy dissipation [54]. Surface loss, on the other hand, plays a major role in Q factor limitation. Therefore, dependence of Q on device surface conditions was studied.

Atomic layer deposition (ALD) can deposit a very dense layer of certain materials on device surfaces with precise atomic layer control. An Al_2O_3 layer was deposited on the microbridges with ALD at 300 ºC, to change their surface conditions. Surface roughness of the microbridges was characterized with Veeco AFM before and after Al_2O_3 ALD deposition, as shown in Fig. 3.14. It can be seen that after Al_2O_3 layer deposition, the surface has more bumps and asperities, and with larger heights (brighter spots in the AFM image). The RMS roughness increases from 6.96 nm to 9.20 nm after ALD, which confirms the roughness increasing. Fig. 3.15 shows the surface roughness value as a function of Al_2O_3 ALD layer thickness. For both arithmetic average and RMS values,

surface roughness increases with ALD layer thickness. A similar finding was reported earlier for certain deposition conditions [62].

Microbridge resonance was tested with different Al_2O_3 layer thicknesses of 7 nm, 14 nm and 21 nm, under 10 mTorr vacuum conditions, as shown in Fig. 3.16. For resonance frequency f_0 (Fig. 3.16a), it can be observed that for four out of five devices, f_0 increases by up to 5% after the first Al_2O_3 ALD layer deposition, which is due to the bridge's dimension change. The width of the microbridge increases with ALD deposition, while $f_0 = \frac{1}{2\pi}\sqrt{\frac{k}{m}} = \frac{1}{2\pi}\sqrt{\frac{32EW^2}{\rho L^4}}$, which is proportional to the bridge width. Also noted is that Al_2O_3 has higher Young's modulus and lower density than the bridge material of TiW, thereby, leading to a higher resonance frequency. As thicker ALD layer was deposited, mass loading began taking effect and lowered the f_0. At 21 nm Al_2O_3 thickness, f_0 decreased by 3% compared to that of 7 nm Al_2O_3 thickness, as can be seen in Fig. 3.16a. For one device, f_0 decreases after ALD deposition, which is due to the strong effect of mass loading.

For Q factor as a function of ALD layer thickness (Fig. 3.16b), the plot can be divided into two segments: 1) from no ALD to first layer of 7 nm ALD; 2) from the first layer of 7 nm ALD to further ALD deposition. For the first segment, three out of five devices have higher Q after ALD deposition. This is due to the fact that surface defects that were present on the microbridges were compensated after fine ALD layer deposition (0.1 nm per cycle), leading to smaller surface loss. For the other two devices, and also for the second segment, Q factor keeps decreasing with thicker ALD layer thickness, which is the result of increased surface roughness (as shown in Fig. 3.15), i.e., higher surface

energy dissipation. A decrease of Q by up to 50% (from maximum of 4,800) was observed at 21 nm Al_2O_3 thickness.

The effect of surface conditions on Q factor is quantized with equations in [54], assuming surface loss is the dominant loss mechanism in the microbridge:

$$Q \cong Q_{surface} = \frac{wt}{2\delta(3w+t)}\frac{E_1}{E_2^S} \tag{3.2}$$

where for the fabricated microbridge, w = 5 μm, t = 1 μm, E_1 = 382 GPa, which are all constants. Two variables in (3.2) are the surface layer thickness δ, and the dissipative Young's modulus of the Al_2O_3 layer E_2^S. Apparently, larger δ leads to smaller $Q_{surface}$. The surface layer's dissipative Young's modulus E_2^S, on the other hand, can be calculated with the data of Q factor as a function of δ.

From Fig. 3.17, it can be seen that the surface layer's dissipative Young's modulus decreases with increasing Al_2O_3 layer thickness. This implies that the surface layer has the most impact on surface Q for small thickness. As the thickness increases, its influence on Q decreases. However, the decrease of E_2^S is not as fast as the increase of surface layer thickness δ. Hence, the combination effect of E_2^S and δ still decreases Q as the surface thickness increases, as illustrated in equation (3.2).

Table 3.1. MEMS Filter Characteristics.

	189 kHz Vrms (mV)	**190 kHz Vrms (mV)**
Input to filter	163.0	163.0
V_{DC} = 62.0 V	83.7 (Rej. Ratio = 5.79 dB)	157.1 (IL = -0.32 dB)
V_{DC} = 62.6 V	165.1 (IL = 0.11 dB)	33.5 (Rej. Ratio = 13.74 dB)

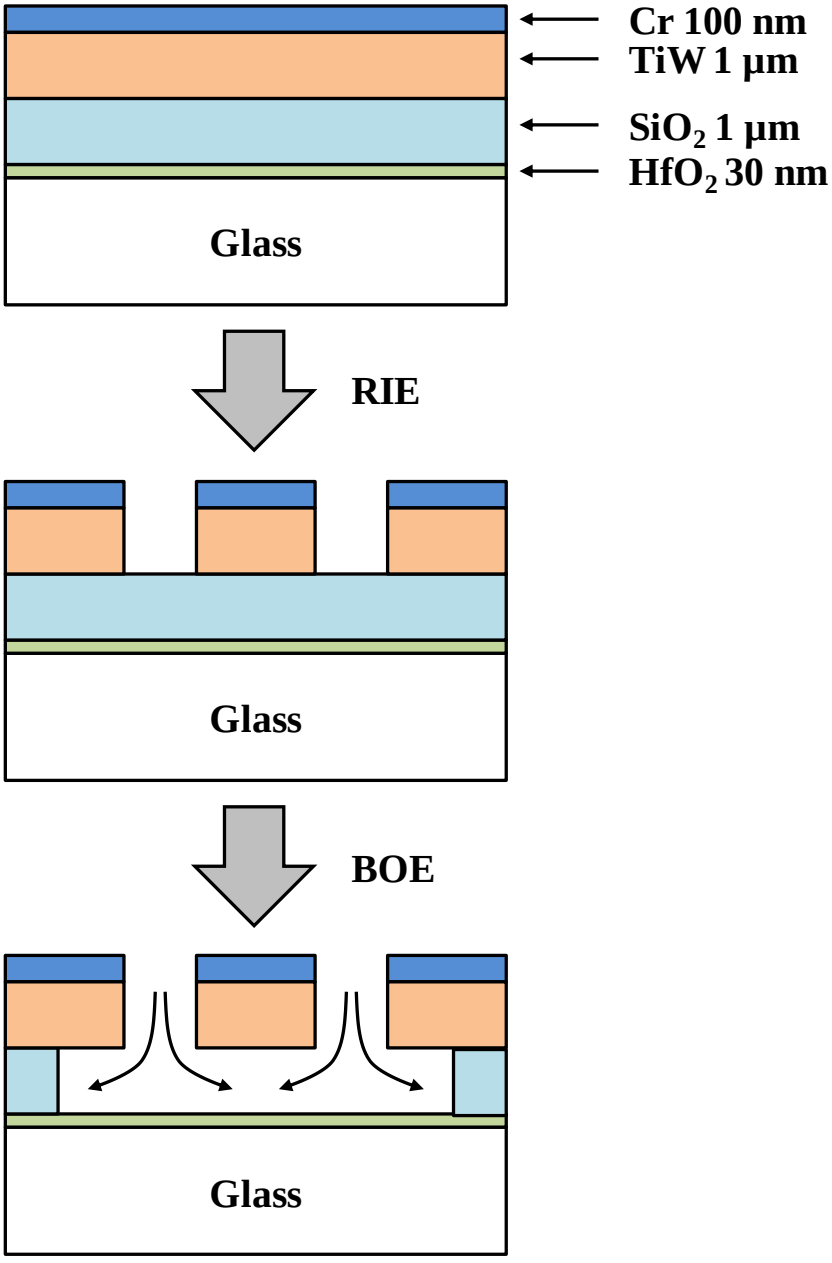

Fig. 3.1. Process flow for fabrication of TiW microbridges.

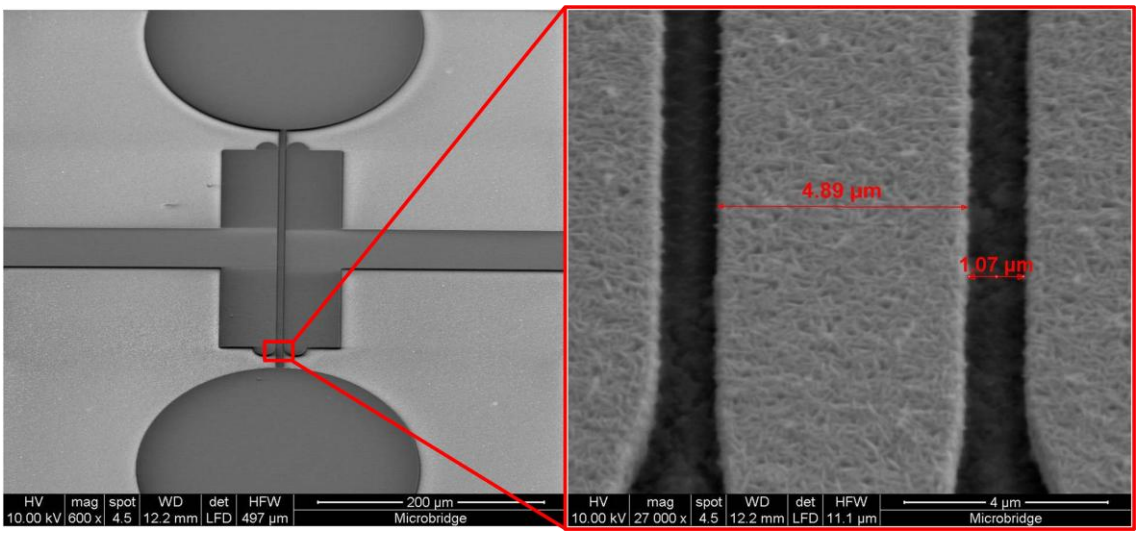

(a) (b)

Fig. 3.2. Fabricated TiW microbridges, with 300 µm long, 5 µm wide, 1 µm thick, and gap of around 1 µm shown in (a). Zoomed-in image of gap is shown in (b).

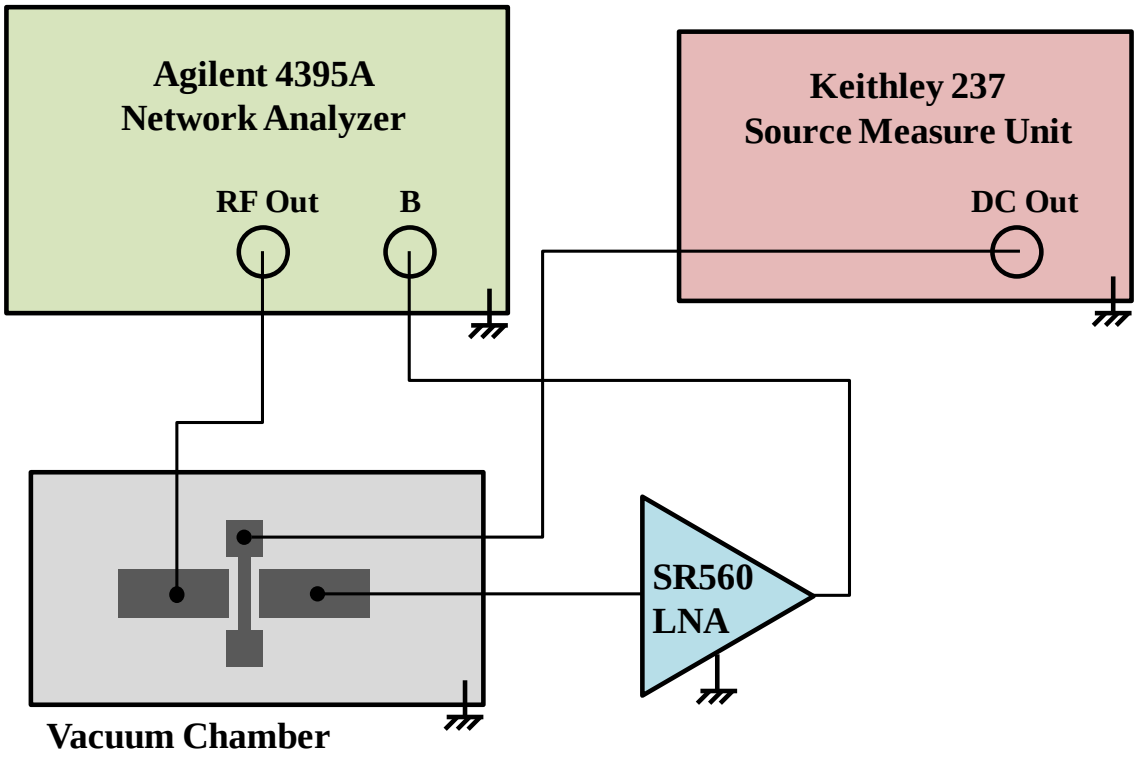

Fig. 3.3. Experiment set-up for microbridges resonance testing, with both electrodes driving/sensing.

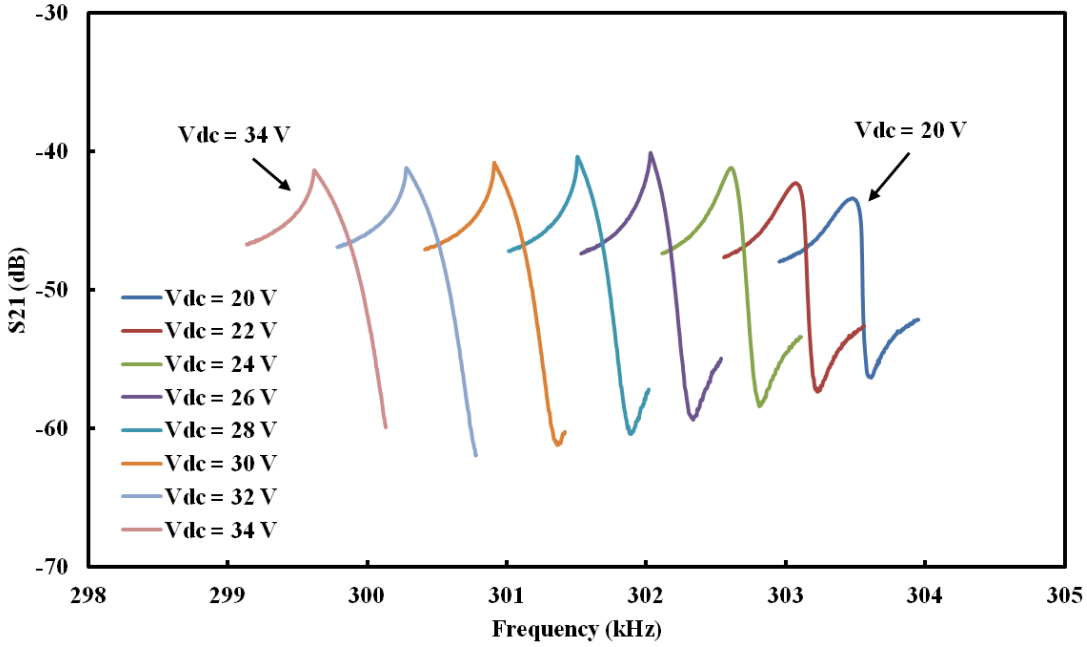

Fig. 3.4. Resonance peaks for a 300 µm long microbridge with different V_{DC} biasing under 10 mTorr. Higher V_{DC} creates lower resonance frequency.

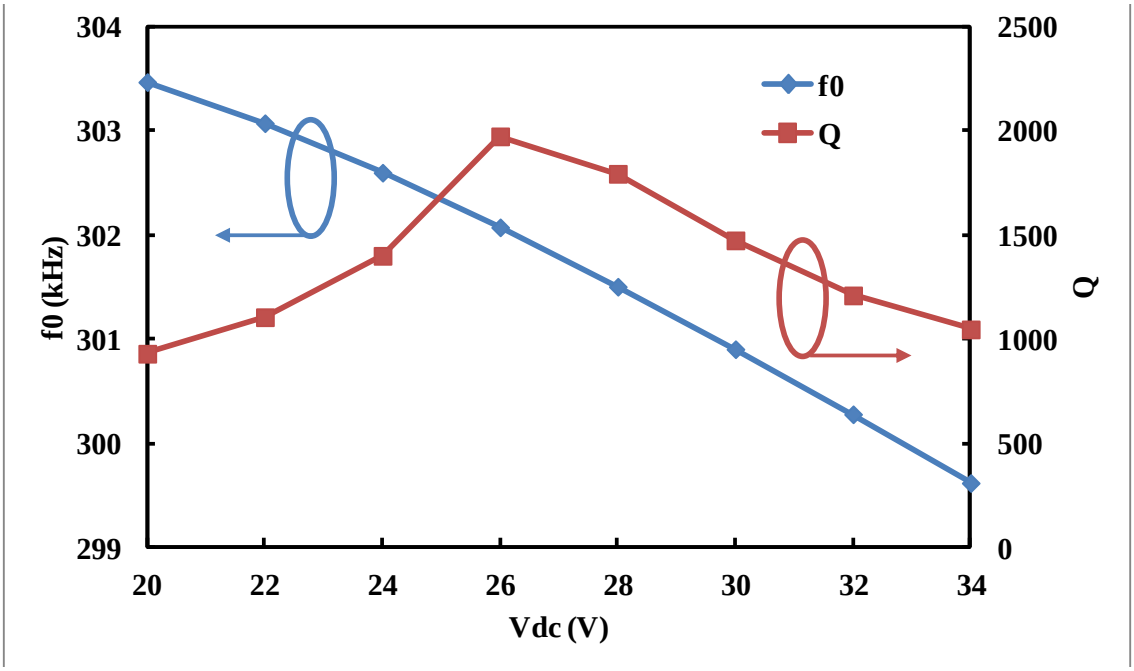

Fig. 3.5. Resonance frequencies and Q as a function of V_{DC} for the 300 µm long microbridge under 10 mTorr.

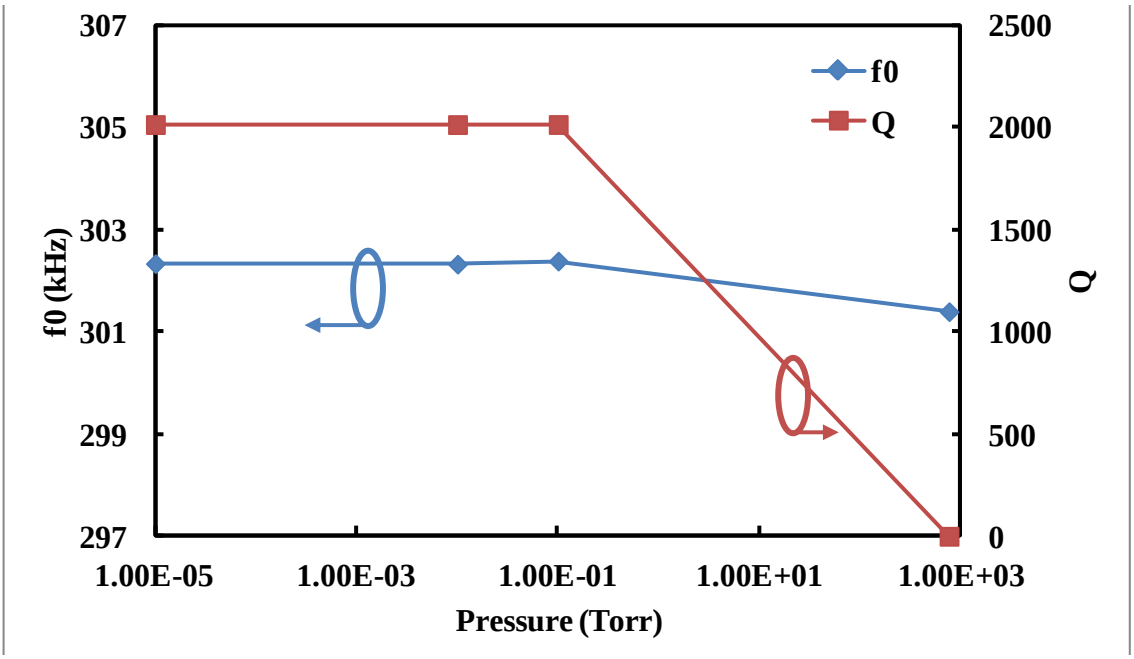

Fig. 3.6. Resonance frequencies and Q as a function of pressure for the 300 µm long microbridge, with V_{DC} biasing of 26 V.

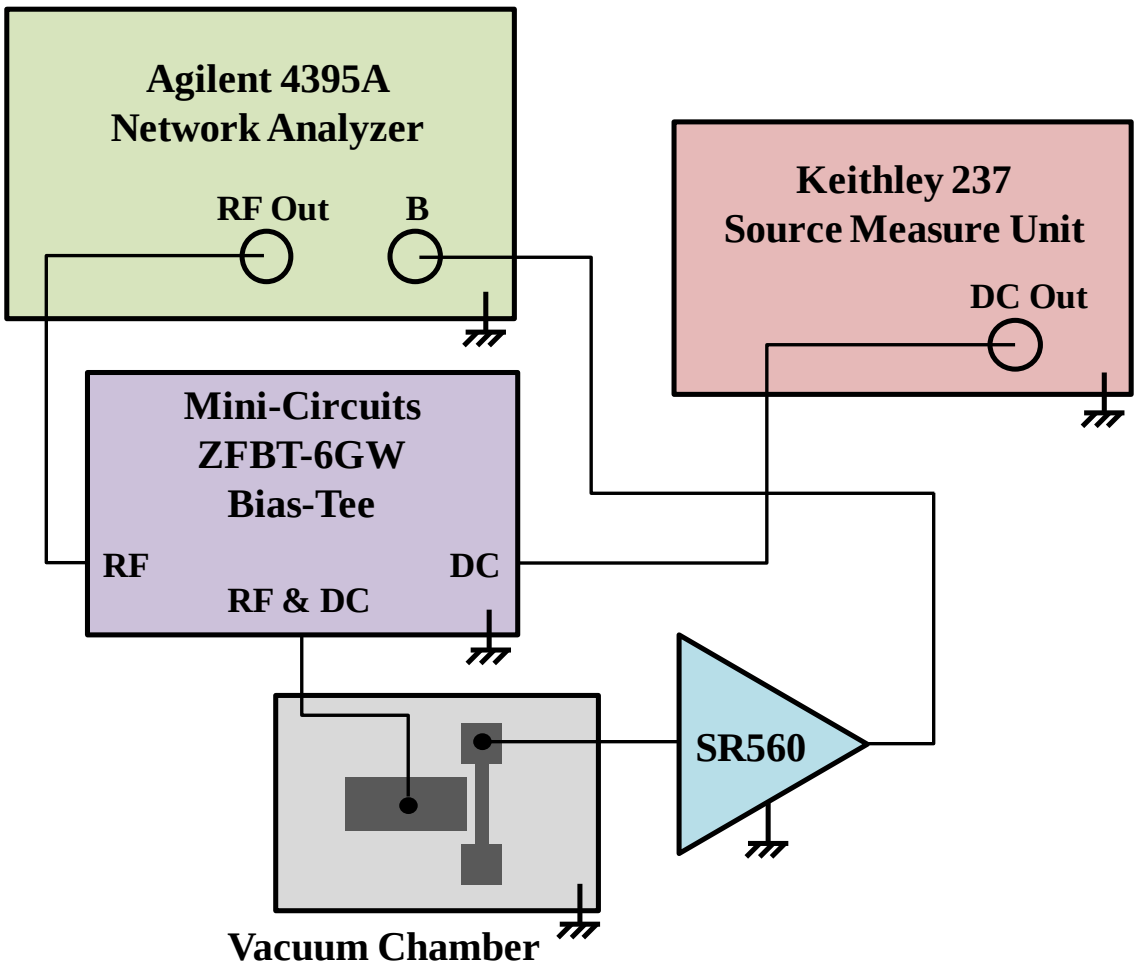

Fig. 3.7. Experiment set-up for microbridges resonance testing, with single electrode driving/sensing.

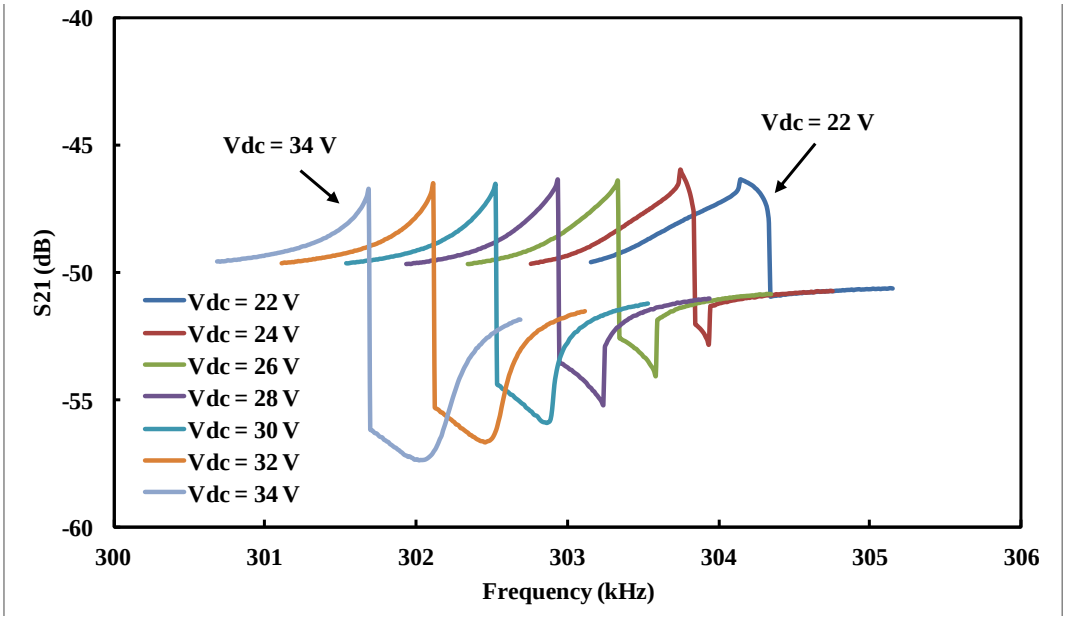

Fig. 3.8. Resonance peaks for the 300 µm long microbridge with different V_{DC} biasing under 10 mTorr, with single electrode driving/sensing. Higher V_{DC} creates lower resonance frequency.

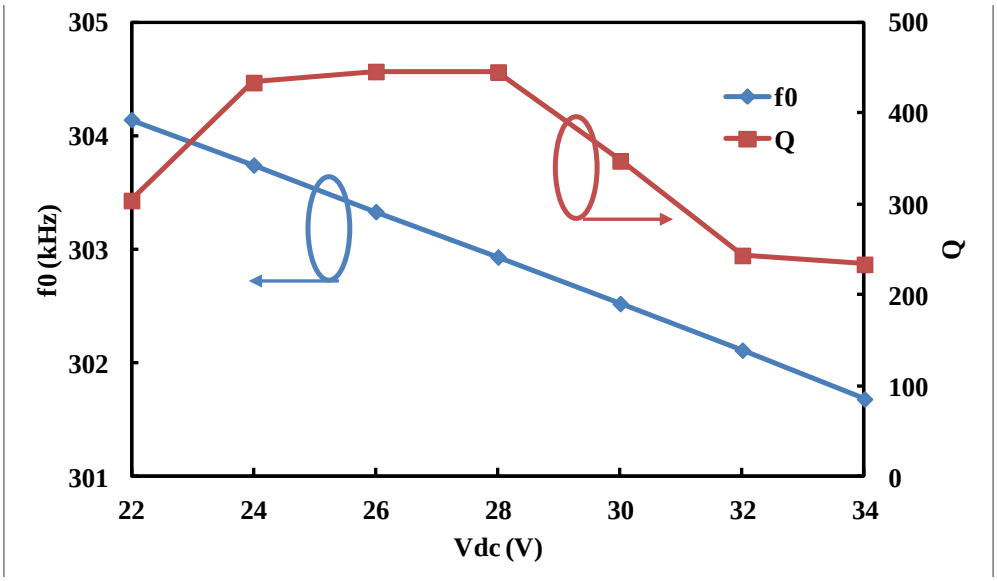

Fig. 3.9. Resonance frequencies and Q as a function of V_{DC} for the 300 µm long microbridge under 10 mTorr, with single electrode driving/sensing.

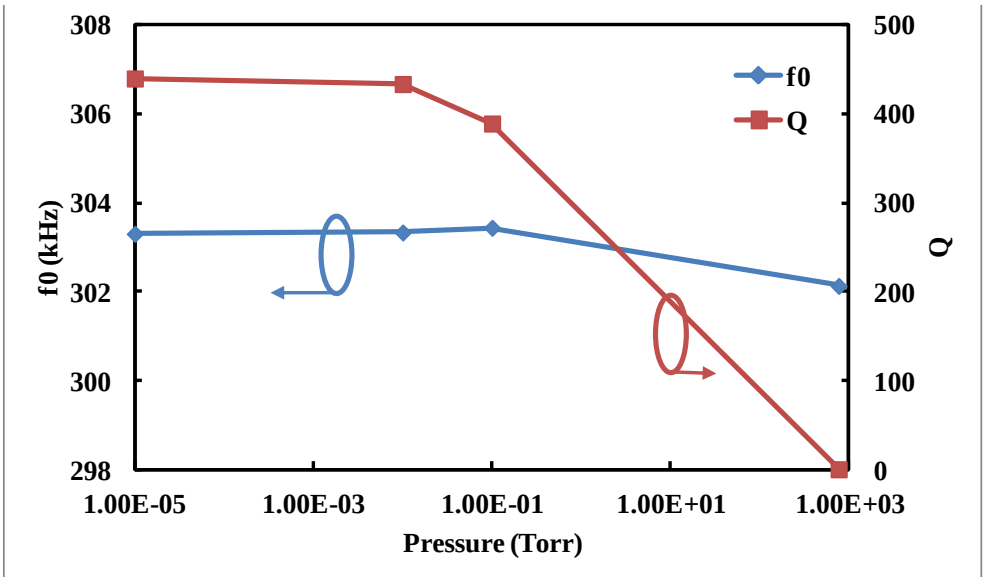

Fig. 3.10. Resonance frequencies and Q as a function of pressure for the 300 μm long microbridge, with V_{DC} biasing of 26 V and single electrode driving/sensing.

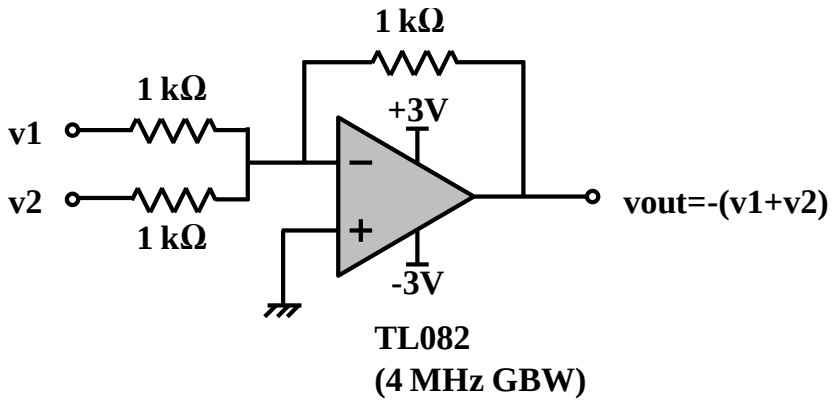

(a)

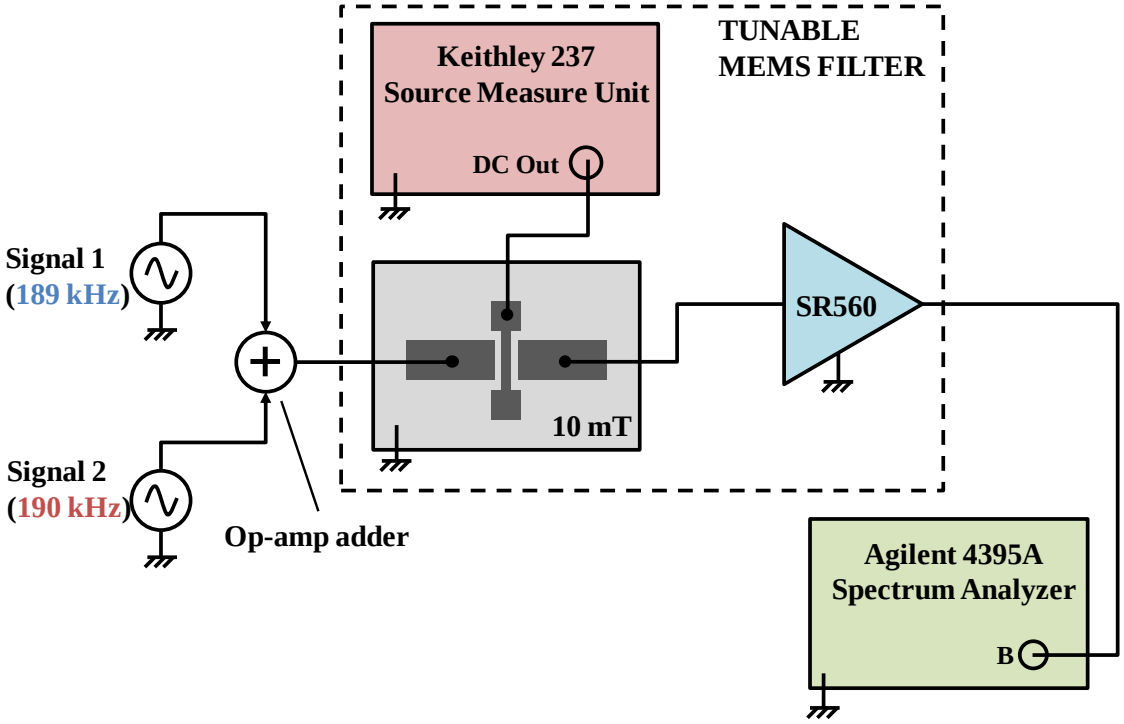

(b)

Fig. 3.11. Circuits for MEMS filter. a) Signal adder with op-amp. b) Complete set-up for MEMS filter with two input signals. SR560 LNA has 2000 gain with bandwidth of 10 k - 1 MHz.

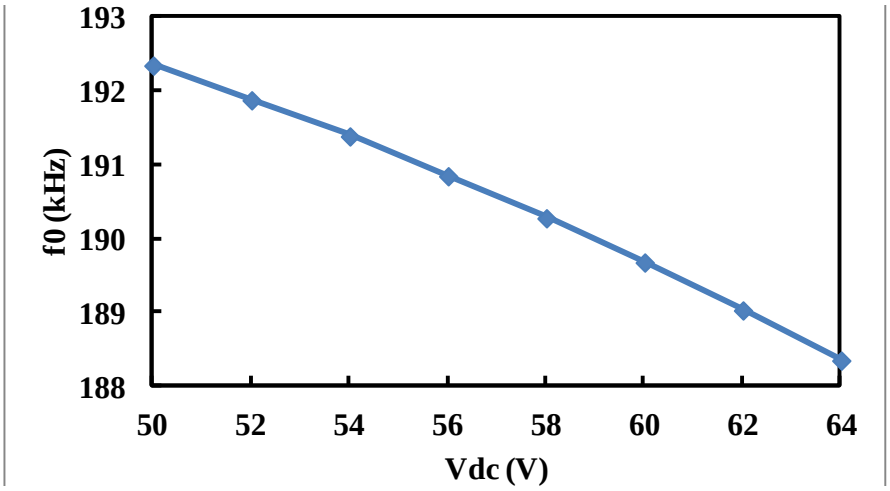

Fig. 3.12. Resonance frequencies versus V_{DC} for a microbridge under 10 mTorr.

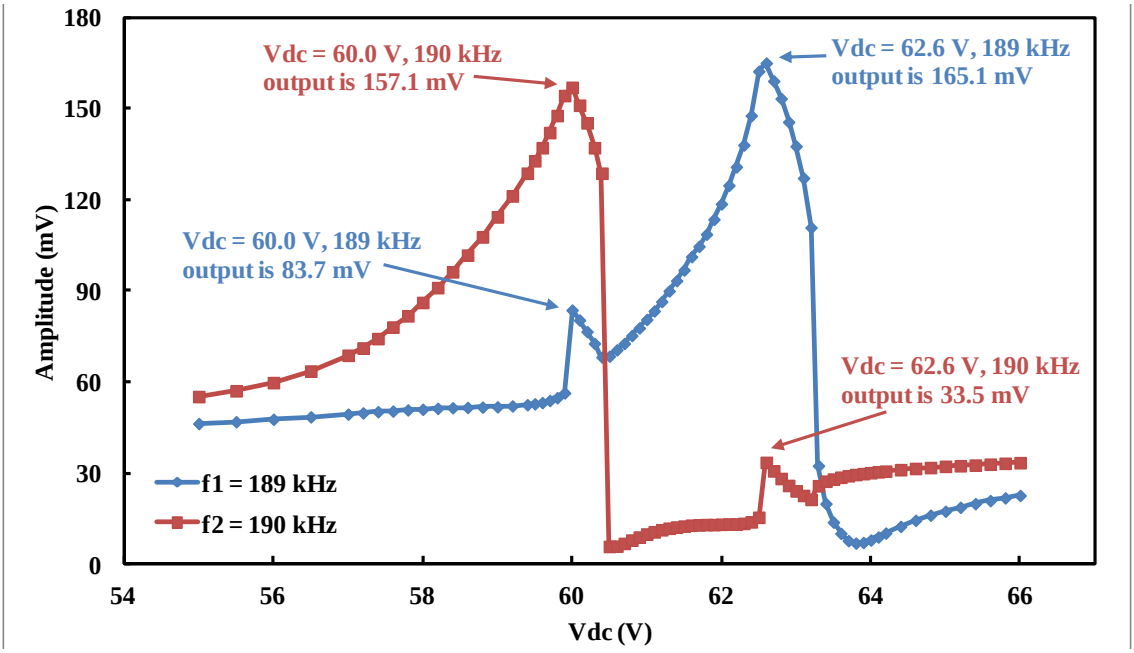

Fig. 3.13. Output signal characteristics of the MEMS filter.

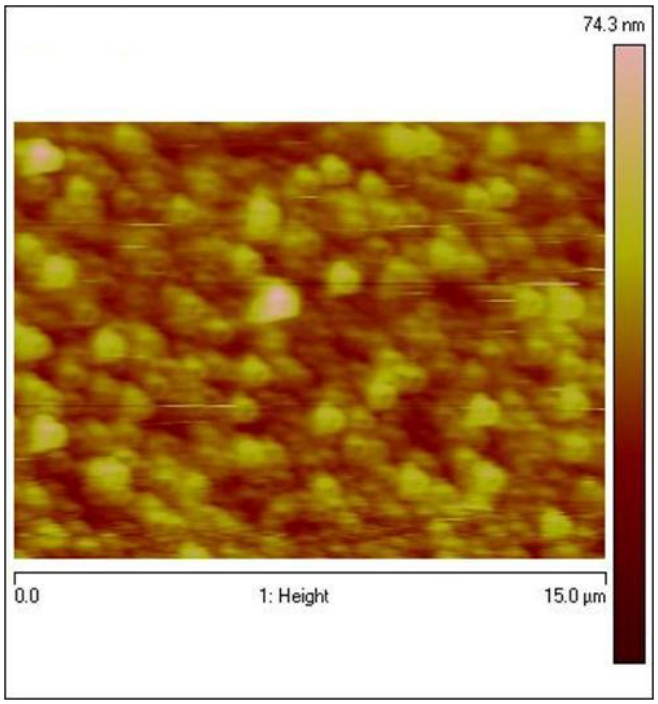

(a)

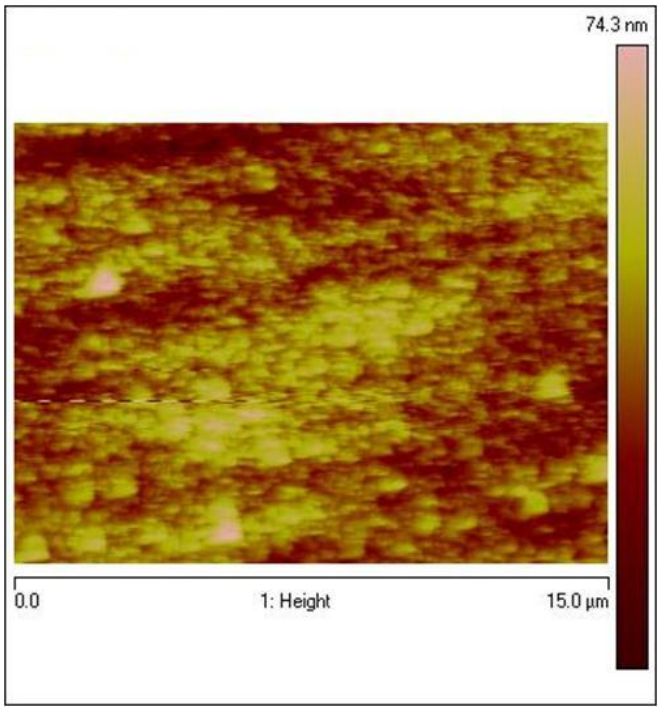

(b)

Fig. 3.14. AFM of devices' surface a) without Al_2O_3 layer (RMS roughness of 6.96 nm) and b) with 21 nm of Al_2O_3 layer (RMS roughness of 9.20 nm).

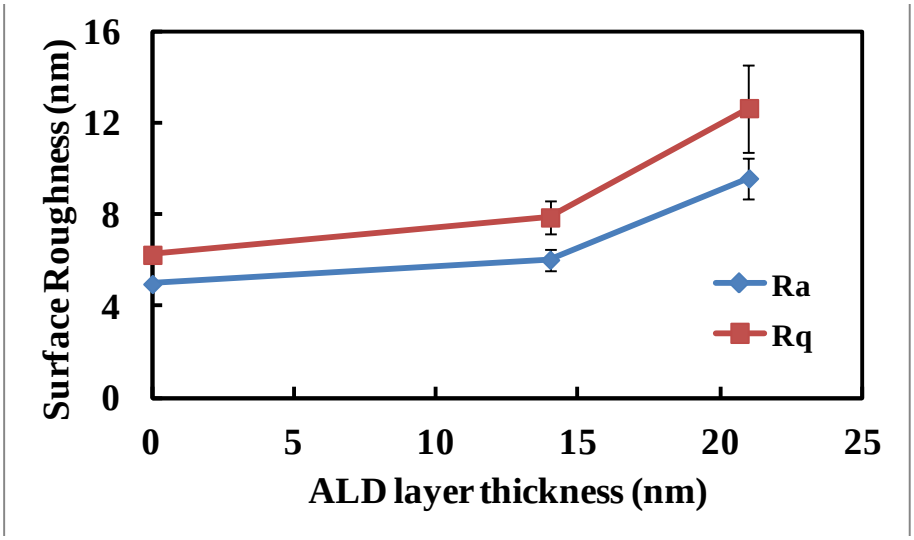

Fig. 3.15. Surface roughness value versus Al_2O_3 layer thickness, where Ra is the arithmetic average roughness, and Rq is the RMS roughness.

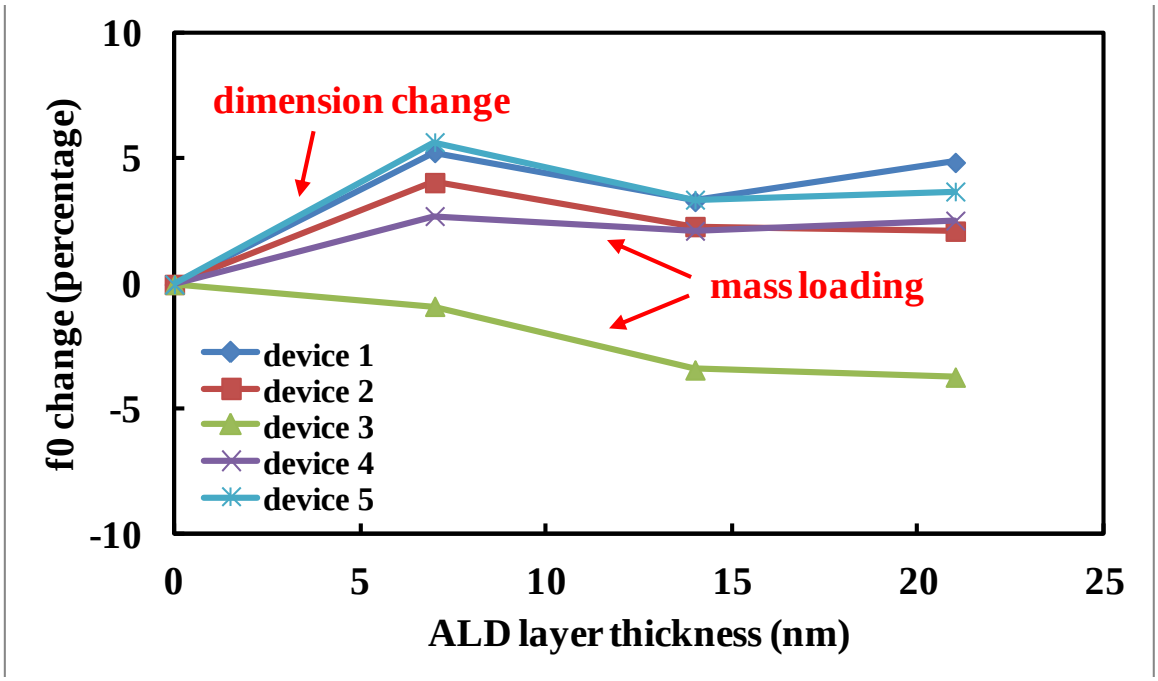

(a)

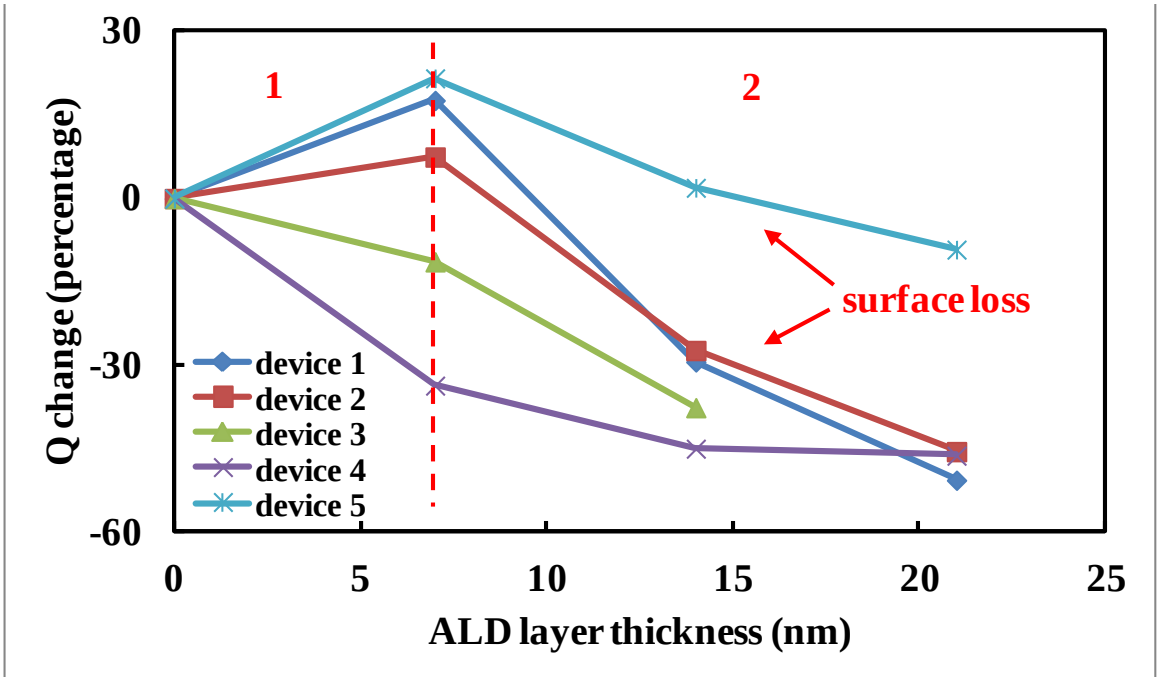

(b)

Fig. 3.16. Dependence of resonator characteristics on Al_2O_3 layer thickness. a) Resonance frequency f_0 and b) Q versus Al_2O_3 layer thicknesses under 10 mTorr.

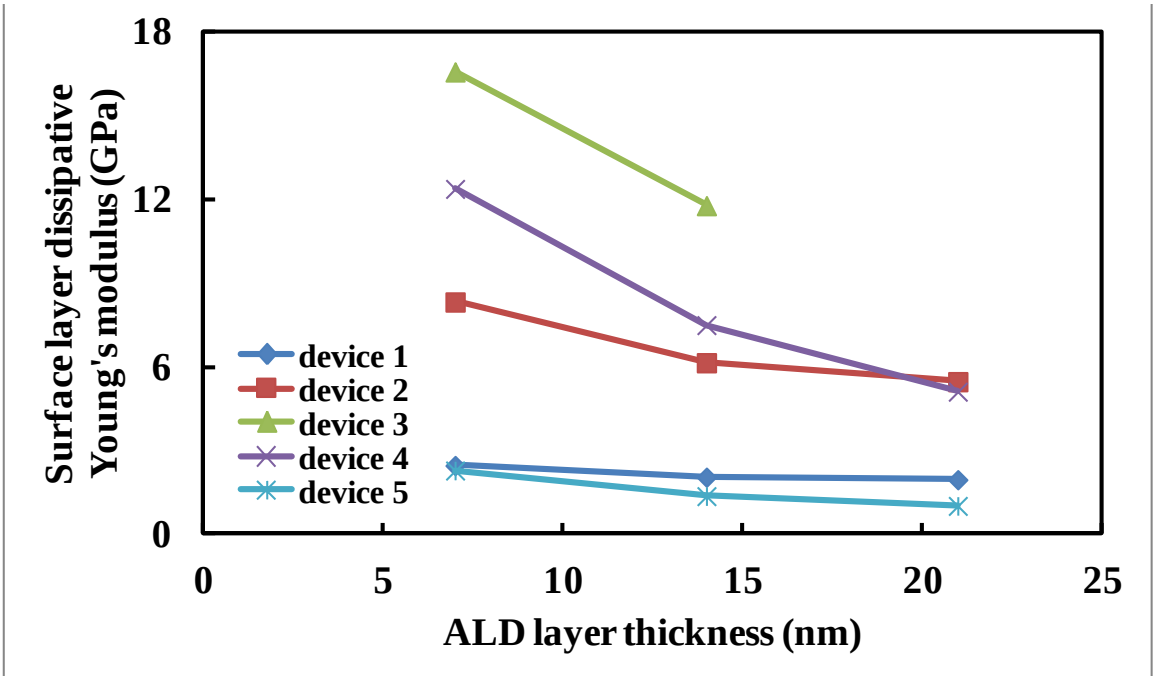

Fig. 3.17. Dissipative part of the Al_2O_3 surface layer's Young's modulus versus Al_2O_3 thickness.

3.6 References

[1] F. Ayazi, "MEMS for integrated timing and spectral processing," *Proceedings of the Custom Integrated Circuits Conference*, San Jose, CA, USA, pp. 65-72, 2009.

[2] E.P. Quevy, S.A. Bhave, H. Takeuchi, T. King and R.T. Howe, "Poly-SiGe high frequency resonators based on lithographic definition of nano-gap lateral transducers," *2004 Solid-State Sensors, Actuators, and Microsystems Workshop*, Hilton Head, SC, USA, pp. 360-363, 2004.

[3] S. Pourkamali, A. Hashimura, R. Abdolvand, G. Ho, A. Erbil and F. Ayazi, "High-Q single crystal silicon HARPSS capacitive beam resonators with sub-micron transduction gaps," *Journal of Microelectromechanical Systems*, Vol. 12, No. 4, pp. 487-496, 2003.

[4] R. Abdolvand and F. Ayazi, "An advanced reactive ion etching process for very-high aspect-ratio sub-micron wide trenches in silicon," *Sensors and Actuators: A. Physical*, Vol. 144, No. 1, pp. 109-116, 2008.

[5] F. Ayazi and K. Najafi, "High aspect-ratio polysilicon micromachining technology," *Sensors and Actuators: A. Physical*, Vol. 87, pp. 46-51, 2000.

[6] F. Ayazi and K. Najafi, "High aspect-ratio combined poly and single-crystal silicon (HARPSS) MEMS technology," *Journal of Microelectromechanical Systems*, Vol. 9, pp. 288-294, 2000.

[7] F. Ayazi, S. Pourkamali, G.K. Ho and R. Abdolvand, "High-aspect-ratio SOI vibrating micromechanical resonators and filters," *2006 IEEE MTT-S International Microwave Symposium Digest*, San Francisco, CA, USA, pp. 676-679, 2006.

[8] S. Pourkamali and F. Ayazi, "18um thick high frequency capacitive HARPSS resonators with reduced motional resistance," *2004 Solid-State Sensors, Actuators, and Microsystems Workshop*, Hilton Head, SC, USA, pp. 392-393, 2004.

[9] S. Pourkamali and F. Ayazi, "Fully single crystal silicon resonator with deep-submicron dry-etched transducer gaps," *Proceedings of the IEEE International Conference on Micro Electro Mechanical Systems (MEMS)*, Maastricht, Netherlands, pp. 813-816, 2004.

[10] S. Pourkamali and F. Ayazi, "SOI-based HF and VHF single-crystal silicon resonators with sub-100 nanometer vertical capacitive gaps," *TRANSDUCERS 2003 - 12th International Conference on Solid-State Sensors, Actuators and Microsystems*, Boston, MA, USA, pp. 837-840, 2003.

[11] S.Y. No, A. Hashimura, S. Pourkamali and F. Ayazi, "Single-crystal silicon HARPSS capacitive resonators with submicron gap-spacing," *2002 Solid-State*

Sensors, Actuators, and Microsystems Workshop, Hilton Head, SC, USA, pp. 281-284, 2002.

[12] M.A. Hopcroft, H.K. Lee, B. Kim, R. Melamud, S. Chandorkar, M. Agarwal, C.M. Jha, J. Salvia, G. Bahl, H. Mehta and T.W. Kenny, "A high-stability mems frequency reference," *TRANSDUCERS 2007 - 14th International Conference on Solid-State Sensors, Actuators and Microsystems*, Lyon, France, pp. 1307-1309, 2007.

[13] R. Abdolvand, H. Johari, G.K. Ho, A. Erbil and F. Ayazi, "Quality factor in trench-refilled polysilicon beam resonators," *Journal of Microelectromechanical Systems*, Vol.15, No.3, pp. 471- 478, 2006.

[14] Z. Hao and F. Ayazi, "Support loss in the radial bulk-mode vibrations of center-supported micromechanical disk resonators," *Sensors and Actuators: A. Physical*, Vol. 134, No. 2, pp. 582-593, 2007.

[15] Z. Hao, S. Pourkamali and F. Ayazi, "VHF single crystal silicon elliptic bulk-mode capacitive disk resonators; Part I: Design and modeling," *Journal of Microelectromechanical Systems*, Vol. 13, No. 6, pp. 1043-1053, 2004.

[16] S. Pourkamali, Z. Hao and F. Ayazi, "VHF single crystal silicon elliptic bulk-mode capacitive disk resonators; Part II: Implementation and characterization," *Journal of Microelectromechanical Systems*, Vol. 13, No. 6, pp. 1054-1062, 2004.

[17] H. Johari and F. Ayazi, "Silicon-on-insulator bulk acoustic wave disk resonators," *Proceedings - IEEE International SOI Conference*, Niagara Falls, NY, USA, pp. 153-154, 2006.

[18] J.R. Clark, W. Hsu, M.A. Abdelmoneum and C. Nguyen, "High-Q UHF micromechanical radial-contour mode disk resonators," *Journal of Microelectromechanical Systems*, Vol. 14, No. 6, pp. 1298-1310, 2005.

[19] Y. Lin, S. Li, Y. Xie, Z. Ren and C. Nguyen, "Vibrating micromechanical resonators with solid dielectric capacitive transducer gaps," *Proceedings of the IEEE International Frequency Control Symposium and Exposition*, Vancouver, BC, Canada, pp. 128-134, 2005.

[20] J. Wang, J.E. Butler, T. Feygelson and C. Nguyen, "1.51-GHz Nanocrystalline diamond micromechanical disk resonator with material-mismatched isolating support," *Proceedings of the IEEE International Conference on Micro Electro Mechanical Systems (MEMS)*, Maastricht, Netherlands, pp. 641-644, 2004.

[21] J. Wang, Z. Ren and C. Nguyen, "1.156-GHz self-aligned vibrating micromechanical disk resonator," *IEEE Transactions on Ultrasonics, Ferroelectrics, and Frequency Control*, Vol. 51, No. 12, pp. 1607-1627, 2004.

[22] E.P. Quevy, A. San Paulo, E. Basol, R.T. Howe, T. King and J. Bokor, "Back-end-of-line poly-SiGe disk resonators," *Proceedings of the IEEE International Conference on Micro Electro Mechanical Systems (MEMS)*, Istanbul, Turkey, pp. 234-237, 2006.

[23] L. Hung and C. Nguyen, "Capacitive-piezoelectric ALN resonators with q>12,000," *Proceedings of the IEEE International Conference on Micro Electro Mechanical Systems (MEMS)*, Cancun, Mexico, pp. 173-176, 2011.

[24] T.L. Naing, T. Beyazoglu, L. Wu, M. Akgul, Z. Ren, T.O. Rocheleau and C. Nguyen, "2.97-GHz CVD diamond ring resonator with Q >40,000," *2012 IEEE International Frequency Control Symposium, IFCS 2012, Proceedings*, Baltimore, MD, USA, pp. 565-570, 2012.

[25] W. Huang, S. Li, Z. Ren and C. Nguyen, "UHF nickel micromechanical spoke-supported ring resonators," *TRANSDUCERS 2007 - 14th International Conference on Solid-State Sensors, Actuators and Microsystems*, Lyon, France, pp. 323-326, 2007.

[26] Y. Xie, S. Li, Y. Lin, Z. Ren and C. Nguyen, "1.52-GHz micromechanical extensional wine-glass mode ring resonators," *IEEE Transactions on Ultrasonics, Ferroelectrics, and Frequency Control*, Vol. 55, No. 4, pp. 890-907, 2008.

[27] Y. Xie, S. Li, Y. Lin, Z. Ren and C. Nguyen, "UHF micromechanical extensional wine-glass mode ring resonators," *Technical Digest - International Electron Devices Meeting, IEDM*, Washington, DC, USA, pp. 953-956, 2003.

[28] J. Cho, J. Yan, J.A. Gregory, H. Eberhart, R.L. Peterson and K. Najafi, "High-Q fused silica birdbath and hemispherical 3-D resonators made by blow torch molding," *Proceedings of the IEEE International Conference on Micro Electro Mechanical Systems (MEMS)*, Tapei, Taiwan, pp. 177-180, 2013.

[29] T. Yen, A.P. Pisano and C. Nguyen, "High-Q capacitive-piezoelectric AlN lamb wave resonators," *Proceedings of the IEEE International Conference on Micro Electro Mechanical Systems (MEMS)*, Taipei, Taiwan, pp. 114-117, 2013.

[30] T.O. Rocheleau, T.L. Naing, Z. Ren and C. Nguyen, "Acoustic whispering gallery mode resonator with Q > 109,000 at 515MHz," *Proceedings of the IEEE International Conference on Micro Electro Mechanical Systems (MEMS)*, Paris, France, pp. 672-675, 2012.

[31] R. Abdolvand, G.K. Ho, J. Butler and F. Ayazi, "ZnO-on-nanocrystalline-diamond lateral bulk acoustic resonators," *Proceedings of the IEEE International Conference on Micro Electro Mechanical Systems (MEMS)*, Kobe, Japan, pp. 795-798, 2007.

[32] S.A. Bhave and R.T. Howe, "Silicon nitride-on-silicon bar resonator using internal electrostatic transduction," *TRANSDUCERS 2005 - 13th International*

Conference on Solid-State Sensors, Actuators and Microsystems, Seoul, South Korea, Vol. 2, pp. 2139-2142, 2005.

[33] S.A. Bhave and R.T. Howe, "Internal electrostatic transduction for bulk-mode MEMS resonators," *2004 Solid-State Sensors, Actuators, and Microsystems Workshop*, Hilton Head, SC, USA, pp. 59-60, 2004.

[34] S. Humad, R. Abdolvand, G.K. Ho, G. Piazza and F. Ayazi, "High frequency micromechanical piezo-on-silicon block resonators," *Technical Digest - International Electron Devices Meeting, IEDM*, Washington, DC, USA, pp. 957-960, 2003.

[35] G. Piazza, R. Abdolvand, G. Ho and F. Ayazi, "Voltage-tunable piezoelectrically-transduced single-crystal silicon micromechanical resonators," *Sensors and Actuators: A. Physical*, Vol. 111, pp. 71-78, 2004.

[36] A. Rahafrooz, A. Hajjam, B. Tousifar and S. Pourkamali, "Thermal actuation, a suitable mechanism for high-frequency electromechanical resonators," *Proceedings of the IEEE International Conference on Micro Electro Mechanical Systems (MEMS)*, Hong Kong, China, pp. 200-203, 2010.

[37] A.K. Samarao and F. Ayazi, "Self-polarized capacitive silicon micromechanical resonators via charge trapping," *Technical Digest - International Electron Devices Meeting, IEDM*, San Francisco, CA, USA, pp. 741-744, 2010.

[38] S. Li, Y. Lin, Y. Xie, Z. Ren and C. Nguyen, "Charge-biased vibrating micromechanical resonators," *Proceedings - IEEE Ultrasonics Symposium*, Rotterdam, Netherlands, pp. 1596-1599, 2005.

[39] S. Pourkamali, R. Abdolvand and F. Ayazi, "A 600kHz electrically coupled MEMS bandpass filter," *Proceedings of the IEEE International Conference on Micro Electro Mechanical Systems (MEMS)*, Kyoto, Japan, pp. 702-705, 2003.

[40] S. Pourkamali and F. Ayazi, "Electrically coupled MEMS bandpass filters; Part I: With coupling element," *Sensors and Actuators: A. Physical*, Vol. 122, No.2, pp. 307-316, 2005.

[41] S. Pourkamali and F. Ayazi, "Electrically coupled MEMS bandpass filters; Part II: Without coupling element," *Sensors and Actuators: A. Physical*, Vol. 122, No.2, pp. 317-325, 2005.

[42] S. Pourkamali, R. Abdolvand, G.K. Ho and F. Ayazi, "Electrostatically coupled micromechanical beam filters," *Proceedings of the IEEE International Conference on Micro Electro Mechanical Systems (MEMS)*, Maastricht, Netherlands, pp. 584-587, 2004.

[43] L. Lin, R.T. Howe and A.P. Pisano, “Microelectromechanical filters for signal processing,” *Journal of Microelectromechanical Systems*, Vol. 7, No. 3, pp. 286-294, 1998.

[44] S. Li, M.U. Demirci, Y. Lin, Z. Ren and C. Nguyen, "Bridged micromechanical filters,” *Proceedings of the 2004 IEEE International Frequency Control Symposium And Exhibition*, Montreal, Que., Canada, pp. 280-286, 2004.

[45] S. Li, Y. Lin, Z. Ren and C. Nguyen, "A micromechanical parallel-class disk-array filter,” *Proceedings of the IEEE International Frequency Control Symposium and Exposition*, Geneva, Switzerland, pp. 1356-1361, 2007.

[46] K. Wang and C. Nguyen, "High-order medium frequency micromechanical electronic filters,” *Journal of Microelectromechanical Systems*, Vol. 8, No. 4, pp. 534-557, 1999.

[47] J.R. Clark, F.D. Bannon III, A. Wong and C. Nguyen, “Parallel-resonator HF micromechanical bandpass filters,” *TRANSDUCERS 1997 - 9th International Conference on Solid-State Sensors, Actuators and Microsystems*, Chicago, IL, USA, Vol.2, pp. 1161-1164, 1997.

[48] P. Ruther, J. Bartholomeyczik, A. Buhmann, A. Trautmann, K. Steffen and O. Paul, “Microelectromechanical HF resonators fabricated using a novel SOI-based low-temperature process,” *IEEE Sensors Journal*, Vol. 5, No. 5, pp. 1112-1119, 2005.

[49] H.C. Nathanson, W.E. Newell, R.A. Wickstrom and J.R. Davis Jr., “The resonant gate transistor,” *IEEE Transactions on Electron Devices*, Vol. 14, No. 3, pp. 117-133, 1967.

[50] G.M. Rebeiz, *RF MEMS: Theory, Design, and Technology*, John Wiley & Sons, 2003.

[51] F.Ayazi, L. Sorenson and R. Tabrizian, "Energy dissipation in micromechanical resonators,” *Proceedings of the SPIE - The International Society for Optical Engineering*, Orlando, FL, USA, pp. 803119, 2011.

[52] A.K. Samarao and F. Ayazi, "Quality factor sensitivity to crystallographic misalignments in silicon micromechanical resonators,” *2010 Solid-State Sensors, Actuators, and Microsystems Workshop*, Hilton Head, SC, USA, pp. 479-482, 2010.

[53] Z. Hao and F. Ayazi, “Support loss in micromechanical disk resonators,” *Proceedings of the IEEE International Conference on Micro Electro Mechanical Systems (MEMS)*, Miami, FL, pp. 137-141, 2005.

[54] K.Y. Yasumura, T.D. Stowe, E.M. Chow, T. Pfafman, T.W. Kenny, B.C. Stipe and D. Rugar, "Quality factors in micron- and submicron-thick cantilevers," *Journal of Microelectromechanical Systems*, Vol. 9, No.1, pp. 117-125, 2000.

[55] J. Yang, T. Ono and M. Esashi, "Energy dissipation in submicrometer thick single-crystal silicon cantilevers," *Journal of Microelectromechanical Systems*, Vol. 11, No. 6, pp. 775-783, 2002.

[56] C. Seoanez, F. Guinea and A.H. Castro Neto, "Surface dissipation in nanoelectromechanical systems: unified description with the standard tunneling model and effects of metallic electrodes," *Physical Review B*, Vol. 77, No. 12, pp. 125107-1 - 14, 2008.

[57] D.F. Wang, T. Ono and M. Esashi, "Thermal treatments and gas adsorption influences on nanomechanics of ultra-thin silicon resonators for ultimate sensing," *Nanotechnology*, Vol. 15, No. 12, pp. 1851-1854, 2004.

[58] T. Kenny, "Nanometer-scale force sensing with MEMS devices," *IEEE Sensors Journal*, Vol. 1, No. 2, pp. 148-157, 2001.

[59] B. Kim, M.A. Hopcroft, R.N. Candler, C.M. Jha, M. Agarwal, R. Melamud, S.A. Chandorkar, G. Yama and T.W. Kenny, "Temperature dependence of quality factor in MEMS resonators," *Journal of Microelectromechanical Systems*, Vol. 17, No. 3, pp. 755-766, 2008.

[60] S.A. Chandorkar, M. Agarwal, R. Melamud, R.N. Candler, K.E. Goodson and T.W. Kenny, "Limits of quality factor in bulk-mode micromechanical resonators," *Proceedings of the IEEE International Conference on Micro Electro Mechanical Systems (MEMS)*, Tucson, AZ, USA, pp. 74-77, 2008.

[61] J. Yang, T. Ono and M. Esashi, "Surface effects and high quality factors in ultrathin single-crystal silicon cantilevers," *Applied Physics Letters*, Vol. 77, No. 23, pp. 3860-3862, 2000.

[62] J.W. Elam, Z.A. Sechrist and S.M. George, "ZnO/Al2O3 nanolaminates fabricated by atomic layer deposition: growth and surface roughness measurements," *Thin Solid Films*, Vol. 414, No. 1, pp. 43-55, 2002.

[63] K. Wetzig and C.M. Schneider, *Metal Based Thin Films for Electronics*, WILEY-VCH, 2003.

CHAPTER 4

ACTION-POTENTIAL-TO-RF MODULE

4.1 Overview

In order to transmit a detected neuron signal through a wireless channel, an RF signal needs to be generated that bears the characteristics of the neuron signal. In other words, the low frequency neuron signal (on the order of 100 Hz) needs to modulate a high frequency carrier signal (hundreds of kHz to MHz) so that the neuron signal waveform can be transmitted. The action potential to RF module inside the internal system takes up this role, which is an electrical oscillator that can be programmed with the neuron signal.

The most common form of linear oscillator is the feedback oscillator, which uses a frequency selective resonator to provide positive feedback along with an amplifier. MEMS oscillators have been proven to offer excellent performance with better integration on silicon substrates and very high quality factor [1-2]. Different categories of MEMS oscillators have been realized based on the type of the resonators, such as air-gap resonator [3-6], disk resonator [7-10], or acoustic wave resonator [11-14].

Another type of oscillator is relaxation oscillator, which works in the nonlinear domain. It is comprised of an energy-storing element and a switching element. The switching circuit periodically charges and discharges the energy-storing element,

producing repetitive output signals given that nonequilibrium conditions are met during each cycle. Fully micromechanical relaxation oscillator was reported [15-19] using the transfer of power between thermal, mechanical and electrical domains, without relying on amplifiers and external circuitry.

This chapter presents two novel approaches for realizing neuron signal programmable oscillators (i.e., action potential to RF module), which are integrated in the neuron interfacing system (Fig. 4.1). The first approach uses MEMS oscillator based on the TiW fixed-fixed bridge resonator, whose DC biasing can be modulated to carry neural signal information. The second approach utilizes the negative resistance property of tunnel diodes to implement a reliable neural signal modulated RF transmitter. This chapter also proposes the idea of a fully MEMS relaxation oscillator utilizing repetitive energy transfer between mechanical and electrical domains.

4.2 Action-Potential-to-RF Module with MEMS Oscillator

In this section, MEMS positive feedback self-sustained oscillator based on the TiW fixed-fixed bridge is presented, with a very high quality factor, larger tuning range and small device footprint. MEMS fabrication can be merged with standard CMOS processes and is more promising in microsystem integration.

The positive feedback set-up for the MEMS oscillator is shown in Fig. 4.2. Two electrodes of the MEMS device were connected to input and output of the SR560 LNA, while the center bridge was connected in series with a 1 GΩ resistor to the DC biasing. The LNA works in the inverted mode, with a phase shift of 180º. A 50 Ω buffer was

connected after the amplifier output, creating appropriate loop interface conditions for stable oscillation.

The working principles of the feedback oscillation can be illustrated in the loop cycle shown in Fig. 4.3. The DC source puts opposite charges on the bridge and the two flank electrodes. Without loss of generality, electrostatic force on the left gap is assumed to be slightly larger than that on the right gap. The bridge was pulled towards the left electrode, leaving left gap g_{left} smaller and right gap g_{right} larger. Left gap capacitance C_{left} becomes larger. The gap capacitor circuit works in the constant charge regime (a valid assumption since the mechanical resonance frequency is high), and therefore the left gap voltage V_{left} decreases. The left gap voltage acts as the input to the low noise amplifier (DC source is regarded as ground to the amplifier). Due to the 180º phase shift of the amplifier, the output, which is the right gap voltage V_{right}, increases. Then the right gap decreases, while the left gap increases. With similar analysis, it is found that as C_{left} decreases, V_{left} increases, and V_{right} decreases. This leads to larger g_{right} and the cycle repeats itself. Oscillation output voltage is then created by the circuit, with frequency determined by the mechanical resonance of the bridge.

Output oscillation signals at 33 V DC biasing for a 200 μm long microbridge are presented in Fig. 4.4, with 442.2 kHz oscillation shown in both time domain and frequency domain. The triangular time domain waveform originates from odd harmonics, which is larger than 1 MHz. Phase noise is calculated from the signal spectra in Fig. 4.4b, which is -84.75 dBc/Hz at 1 kHz offset. Tuning of the oscillation frequencies for the 200 μm long microbridge is shown in Fig. 4.5, along with tuning of the resonance frequencies obtained with set-up in Fig. 3.3. Tuning sensitivity of the oscillation frequency is found

to be 0.36 kHz/V. These two sets of frequencies are very close to each other for different biasing conditions, with the oscillation frequency a little higher than the resonance frequency. The reason for this is that the bridge displacement is small in the resonance testing, so the bridge is not under stress. For oscillation generation with positive feedback, however, the bridge displacement is very large, which introduces tensile stress and increases the spring constant, leading to higher oscillation frequencies.

Action-potential-to-RF module can be realized with the MEMS oscillator circuit by connecting the DC biasing with a processed neural signal. Since the oscillation frequency can be tuned with DC biasing, frequency modulated (FM) signal can be obtained from the oscillator output once the DC biasing is controlled by the neural signal. The resulting FM signal then carries the neural signal information. The FM signal carries information with its frequency, and therefore is invulnerable to distance variation, which only changes signal amplitude. This suits the requirement of the wireless data transmission system well.

Fig. 4.6 shows the original neural signal and its amplified and biased version. V_{peak} and $V_{undershoot}$ represent the peak pulse voltage and undershoot voltage of the original neural signal, respectively (Fig. 4.6a). This signal is then amplified and biased, with V_{peak}' and $V_{undershoot}$' representing the amplified voltages (Fig. 4.6b). The neural signal needs to be biased (V_{bias}) before being fed to the oscillator's DC biasing, because the MEMS feedback oscillator needs a minimum DC voltage to be turned on. For the 200 μm long microbridge, the threshold turn-on voltage is around 30 V. The neural signal frequency modulation and restoration results will be described in detail in Chapter 6.

4.3 Tunnel Diode Oscillation Circuit

A MEMS oscillator based RF transmitter has a very small device footprint and can be easily integrated with IC-compatible micromachining processes. However, it requires a sustaining amplifier, which increases system power consumption. Negative resistance, however, can be utilized to create oscillators without relying on an external amplifier. Tunnel diode is the most commonly used negative resistance device. It is fabricated with heavily doped p-n junction (degenerate doping) of very narrow width of around 10 nm. The tunneling current across the pn junction creates the negative resistance characteristics.

Fig. 4.7 shows the I-V plot of a germanium tunnel diode (1N3561), which is an N-shaped curve. The negative resistance region locates between the points of (V_P, I_P) (70 mV, 0.474 mA) and (V_V, I_V) (465 mV, 0.11 mA). Figure of merit for a tunnel diode is the ratio of Ip/Iv, which is 4.3 for this device.

A tunnel diode oscillation circuit with quartz crystal frequency control is shown in Fig. 4.8. Input to the circuit is the DC bias (V_{DC}), and the output is oscillation waveform across the inductor. Frequency of the generated oscillation is locked to the resonance frequency of the crystal. The crystal can be replaced with a capacitor, in which case the oscillation frequency is based on inductance of the coil, along with combined capacitance of the tunnel diode and quartz crystal. This oscillation circuit can be easily converted to a capacitor modulated FM signal transmitter for this case, in which the quartz resonator is replaced by a capacitive sensor [20].

The working principle of the tunnel diode oscillation circuit is shown with I-V trajectory in Fig. 4.9. Current through the inductor cannot change instantly, which leads

to a sudden jump of operating point from V_P to V_{FP} (no current change) and V_V to almost zero voltage (no current change). The cycle repeats itself, as long as V_{DC} is biased at the negative resistance region (between V_P and V_{FP}). The circuit model is shown in Fig. 4.10. Negative resistance R_{TD} of the tunnel diode enables oscillation, while resonance branch of the quartz crystal selects the oscillation frequency.

A tunnel diode oscillation circuit that generated 8 MHz signal is shown in Fig. 4.11. Germanium tunnel diode 1N3717 (parameters shown in Table 4.1) was in shunt with an 8 MHz quartz crystal resonator. Output was taken from the coil inductor, with waveform shown in Fig. 4.12. The output was also fed into a spectrum analyzer (Agilent 4395A 10 Hz - 500 MHz Spectrum Analyzer), with spectra shown in Fig. 4.13. The peak happened at 7.998875 MHz, with signal power of -16.14 dBm. Considering the 50 Ω port impedance, the output power corresponds to 49.3 mV peak amplitude. The circuit consumed power of 0.21 mW.

The effect of V_{DC} on the oscillation was characterized with circuits as shown in Fig. 4.14. The output was monitored with the Agilent spectrum analyzer. Tuning of the output peak frequency f_0 was realized using V_{DC}. Fig. 4.15 shows that f_0 increased with increasing V_{DC}, achieving tuning sensitivity of 4.19 Hz/mV. The quality factor varied with V_{DC}, and showed "digital oscillation" like fluctuations (Fig. 4.16). The reason for this is that the half-power bandwidth of the tunnel diode circuit oscillation spectrum was so small (less than 6 Hz), that it was even comparable to the spectrum analyzer's minimum resolution bandwidth (RBW) (1 Hz). Therefore the accuracy of the half-power bandwidth detection was hampered and introduced fluctuations. However, for all V_{DC} values, the Q factor was always larger than 800,000. Fig. 4.17 shows the total current

values as a function of V_{DC}. The power consumption was as low as 0.56 mW and could be further reduced using the optimization of the circuit. The reason for the tuning of f_0 with V_{DC} was due to frequency pulling. As shown in Fig. 4.10, junction capacitance of the tunnel diode C_j and load capacitance of quartz crystal C_L both changed with V_{DC}, shifting resonance frequency of the LC circuit, leading to frequency modulation of the output signal.

4.4 Action-Potential-to-RF Module with Tunnel Diode Oscillation Circuit

A module that converts neuron action potential to RF signal was realized with the tunnel diode oscillation circuit [22]. V_{DC} was replaced with amplified neuron signal, creating neuron signal modulated RF output.

To test the feasibility, artificial neuron firing signals were produced and detected by the system. An artificial neuron firing signal was produced using an electric dipole covered with an insulating layer, shown in Fig. 4.18, inside Ringer solutions (to mimic the brain environment). Square or triangular pulses of 10 ms width were applied to the input cable, creating pulses (positive and negative) 10 ms apart in the output port (another electric dipole) through capacitive coupling of the electric dipole with the Ringer solution and the output dipole. This signal was amplified (gain of 20) and used to drive the action-potential-to-RF module (through V_{AP}) and generated the modulated RF signal (Fig. 4.19). Fig. 4.20 and 4.21 show V_{AP} (original and amplified) along with oscillations generated from the tunnel diode circuit. Both positive (Fig. 4.20) and negative parts of the action potential (Fig. 4.21) were able to drive the tunnel diode circuits to create oscillations of

0.35 μs duration with different frequencies by different quartz crystal resonators (16 MHz and 8 MHz, respectively). It can be seen that the amplitude of the oscillation signal is a little larger than the input amplified neural signal. This is due to the setting of oscilloscope input impedance, which is 1 MΩ and 50 Ω for these two cases, respectively.

Here we compare the two approaches of action-potential-to-RF module. Both systems can deliver a very high quality factor oscillation output bearing neural signal information. A MEMS oscillator based transmitter has a small device footprint, easier IC-compatible fabrication processes, and larger tuning range, but may require large biasing voltage. A tunnel diode oscillator has simple circuitry, and requires low turn-on voltage, but suffers from small tuning range and difficult germanium integration. Based on the above analysis, MEMS oscillator is the preferable choice. The large biasing voltage can be reduced by careful design of the MEMS structure, which will be discussed in the Further Work chapter.

4.5 Dynamic Analysis of Relaxation Oscillation Based MEMS DC-to-RF Converters

Besides taking advantage of positive feedback circuit with sustaining amplifier, pr tunnel diode negative resistance, relaxation oscillation is another well-known method to create an RF signal. The idea was first tested with a macromodel based on piezoelectric devices.

Fig. 4.22 shows a circuit for a relaxation oscillator implemented with an audio-range piezoelectric disk. The piezo disk displaces by 10s of um when a DC voltage is applied between the two metal electrodes across it, due to the piezoelectric effect. This DC

enabled displacement is repeatable and stable. An electrode, which is in series with a 1 kΩ resistor to ground, was positioned very close to the positive plate of the piezo disk. The distance was fine controlled to be in the same range of the DC induced piezo disk displacement. As shown in Fig. 4.22, a 100 kΩ resistor was added inside the circuit for two reasons: 1) to ensure that potential on the positive plate drops to a much lower voltage ($36\ V \times \frac{1\ k\Omega}{100\ k\Omega+1\ k\Omega} = 0.36\ V$) when it touches the nearby electrode; 2) to limit the current through the circuit branch during contact. With this set-up, when the DC supply is on, piezo disk displaces by piezoelectric effect, causing its positive plate to move left. When the plate touches the nearby electrode, a short circuit is generated and the potential on the plate drops to 0.36 V, which is not sufficient for piezo disk displacement. The piezo disk then moves back, losing the contact, and V_{DC} of 36 V is then applied across the piezo disk once more. The disk moves left again and the cycle repeats itself. After delicate tuning of the relative location between the positive plate and the nearby electrode, oscillations can be generated when V_{DC} is on. The oscillation was detected with an oscilloscope of 1 MΩ input impedance. The waveform is shown in Fig. 4.23. The frequency is 5 kHz, which is the resonant frequency of the audio piezo disk.

Based on the idea of the relaxation oscillator, a novel MEMS DC-to-RF converter was proposed. The following section presents the dynamic analysis of the working principle of MEMS DC-to-RF converter.

The circuit for MEMS DC-to-RF based on fixed-fixed bridge is shown in Fig. 4.24. A constant current source is connected to the bridge, which forms a capacitor with the nearby electrode. Charges will be accumulated across the gap provided by the current source, leading to electrostatic actuation of the bridge, creating a varying capacitor.

The working principle of MEMS DC-to-RF converter can be explained as shown in Fig. 4.25. Each cycle is comprised of three phases: “charge and pull-in,” “discharge” and “release.” The phase of “discharge” upon contact is very fast; therefore the other two phases decide the oscillation frequency. In order to create sustainable self-oscillation, mechanical pulling-in and releasing time should be much smaller than electrical charging time. This criterion ensures complete oscillations with full bridge displacement. Otherwise, the bridge-electrode capacitor would charge up before the bridge can relax to its original position.

With this criterion, the “charge and pull-in” phase is dominated by electrical charging time. Using electrostatic equations

$$F_e = EQ = \frac{V}{g}Q = \frac{Q}{Cg}Q = \frac{Q^2}{Cg} = \frac{Q^2}{\varepsilon_0 A} \tag{4.1}$$

where g is the current gap size, while Q and A are the charge and area of the gap capacitor, respectively. Since the mechanical pull-in time is much shorter than electrical charging time, it can be assumed that dynamic equilibrium between electrostatic force and mechanical spring restoring force can be achieved during the pull-in time

$$F_e = \frac{Q^2}{\varepsilon_0 A} = F_s = k(g_0 - g) \tag{4.2}$$

where k is the bridge’s spring constant. We can get the relationship between Q and g

$$Q = \sqrt{\varepsilon_0 A k(g_0 - g)} \tag{4.3}$$

The well known condition for bridge pull-in is $g = 2/3 \times g_0$, after which the bridge pulls onto the electrode due to positive feedback. Substitute this into (4.3), and we get

$$Q_{pull-in} = \sqrt{\frac{1}{3}\varepsilon_0 A k g_0} \tag{4.4}$$

This is the charge that is needed to pull in the bridge to the electrode. Note that a current source is used to accumulate the charge, and the time for pull-in can be obtained

$$t_{charge} = \frac{Q_{pull-in}}{I_0} = \frac{\sqrt{\frac{1}{3}\varepsilon_0 A k g_0}}{I_0} \tag{4.5}$$

where I_0 is the value of the current source. Equation (4.5) gives the time for the "charge and pull-in" phase. For TiW bridge of 300 μm long, 5 μm wide, 1 μm thick, 1 μm gap and current source of 10 nA, t_{charge} is 22 μs.

Mechanical pull-in and release time can be calculated using a second-order model of the MEMS bridge. For pull-in, we have

$$m\frac{d^2x}{dt^2} + b\frac{dx}{dt} + kx = F_e \tag{4.6}$$

where m, b, k and F_e are the bridge mass, damping factor, bridge spring constant and electrostatic force, respectively. With initial conditions of

$$\begin{cases} t = 0, x = g_0 \\ t = 0, \dfrac{dx}{dt} = 0 \end{cases}$$

meaning that initial bridge position is g_0 and bridge velocity is zero, we can get bridge displacement with ringing down oscillations. Note that the bridge snaps to the electrode beyond the position of 2/3 × g_0, we can get the bridge position versus time as shown in Fig. 4.26a for certain bridge parameters. The time for the bridge to mechanically pull in is

$$t_{pull-in} = \frac{1}{4}\frac{1}{f_0} \tag{4.7}$$

where f_0 is the bridge's mechanical resonance frequency. For the bridge shown in Fig. 4.26a, $t_{pull\text{-}in}$ is 0.97 μs, corresponding to f_0 of 257 kHz. The mechanical pull-in time $t_{pull\text{-}in}$ is much smaller than electrical charging time t_{charge}, meaning that t_{charge} dominates the

time for "charge and pull-in" phase, and guarantees dynamic equilibrium of the bridge pull-in actuation as mentioned above.

Similarly, for mechanical releasing, we have

$$m\frac{d^2x}{dt^2} + b\frac{dx}{dt} + kx = 0 \tag{4.8}$$

with initial conditions of

$$\begin{cases} t = 0, x = 0 \\ t = 0, \dfrac{dx}{dt} = 0 \end{cases}$$

We can get bridge displacement with ringing down oscillations. Consider that the bridge operates at the nonlinear regime and the spring softening effect, the ring-down and overshooting of the bridge movement are very small (though the Q may be high). The bridge position versus time is shown in Fig. 4.26b. The time for the bridge to mechanically release is

$$t_{release} = \frac{1}{4}\frac{1}{f_0} \tag{4.9}$$

which is the same as mechanical pull-in. The mechanical releasing time is much smaller than electrical charging time, meaning that the bridge is able to relax to its original positions before electrical charging takes place, which ensures sustainable complete oscillations.

From the above analysis, we found that to maintain sustainable oscillations, electrical charging time should be much larger than both mechanical pull-in and releasing time. Therefore, the criterion for oscillation is

$$\frac{\sqrt{\frac{1}{3}\varepsilon_0 A k g_0}}{I_0} \gg \frac{1}{4}\frac{1}{f_0} \tag{4.10}$$

Fig. 4.27 shows circuit parameters versus time for sustainable oscillations. It can be seen that mechanical release time is much smaller than electrical charging time.

4.6 Experimental Results of MEMS DC-to-RF Converters

The concept of DC-to-RF conversion was tested with the fabricated MEMS TiW fixed-fixed bridges. The set-up (Fig. 4.28) consists of a series circuit of DC source (Keithley 237 SMU), voltage/current limiting resistor (40 MΩ), contact resistances of probing tips (Rc of 5 Ω), the MEMS device, and an oscilloscope. Keithley 237 operated in the voltage source mode with current compliance limitation, working as a current source for bridge actuation. As it was turned on, charges began accumulating across the gap of the bridge, pulling the bridge towards the electrode with electrostatic actuation. When the bridge got very close to the electrode, tunneling current set in and discharged the electrode-bridge capacitor instantly. This reduced the electrostatic force and the bridge relaxed back to its equilibrium location, and the cycle repeated itself (Fig. 4.29). This cycle is stable provided that the time constants associated with electrode-bridge discharging, electrode charging and the bridge motion are carefully selected. A self-sustained pulsed oscillation waveform can be detected from the oscilloscope (Fig. 4.30), with frequency of 3.7 Hz. One reason for the low frequency of oscillation is contact damaging and stiction by localized heating. This can be solved by lowering actuation voltage by reducing gap size, to limit heating. Very low power (nW), kHz-GHz frequency range RF oscillators can be realized with these devices. For example, carbon nanotube (CNT) has very large Young's modulus (1 TPa) and can be grown self-aligned as a MEMS bridge with up to GHz resonance frequency depending on its length.

Table 4.1. Tunnel diode 1N3717 parameters.

I_P (mA)	I_V (mA)	I_P/I_V	V_P (mV)	V_V (mV)	V_{FP} (mV)
4.7	0.485	9.69	59	352	511

Capacitance (pF)	Series Inductance (nH)	Series Resistance (Ω)	Negative Resistance (Ω)	Material
25	0.5	0.52	24	Germanium

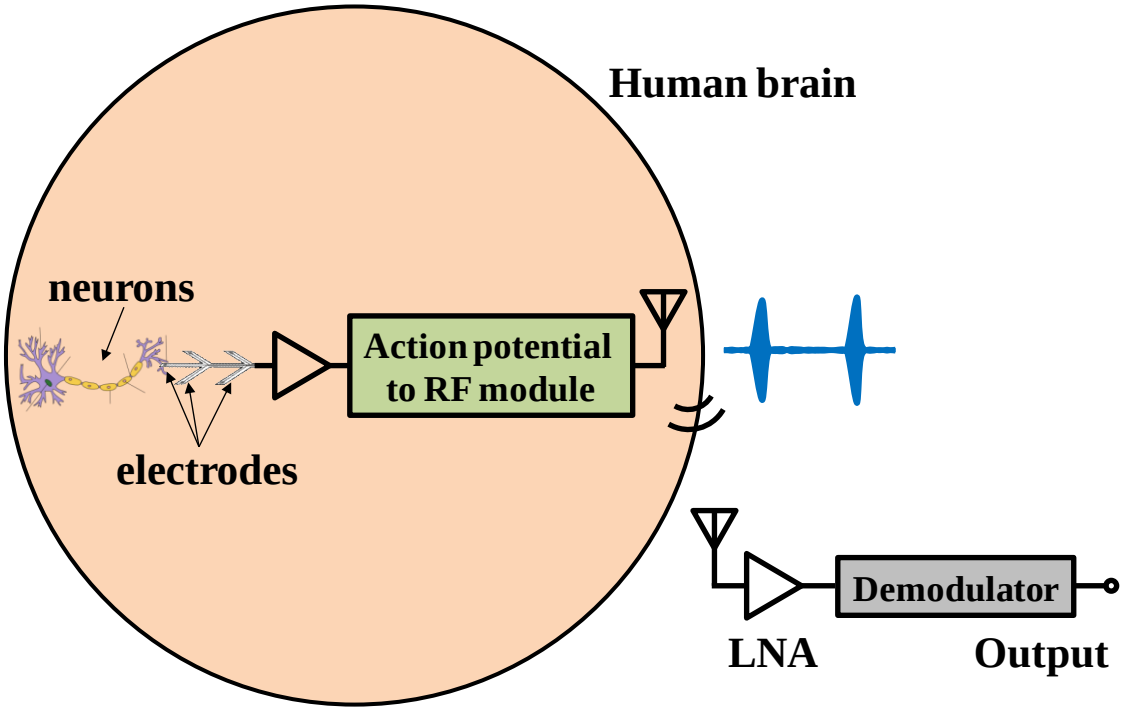

Fig. 4.1. Diagram of action potential to RF module inside the neuron interfacing system.

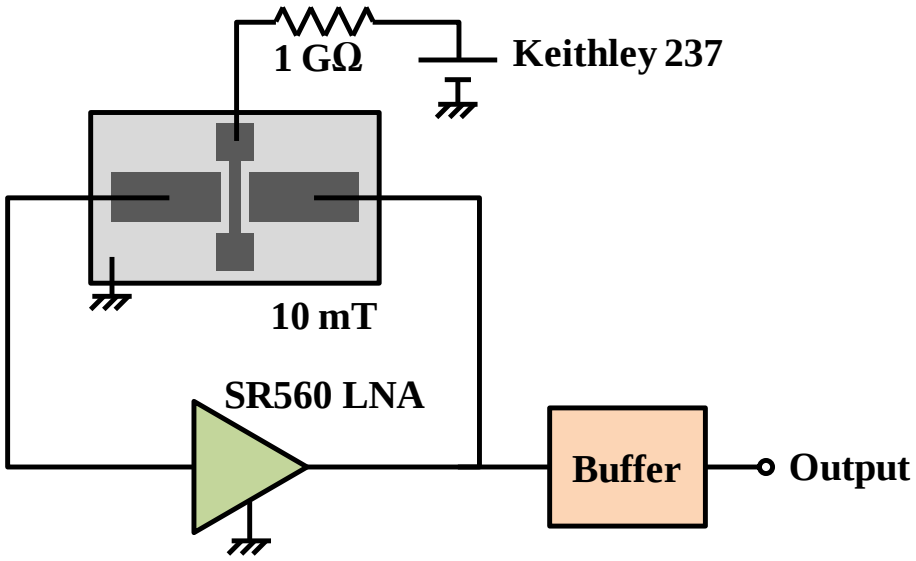

Fig. 4.2. Positive feedback set-up for MEMS oscillator with self-sustaining amplifier.

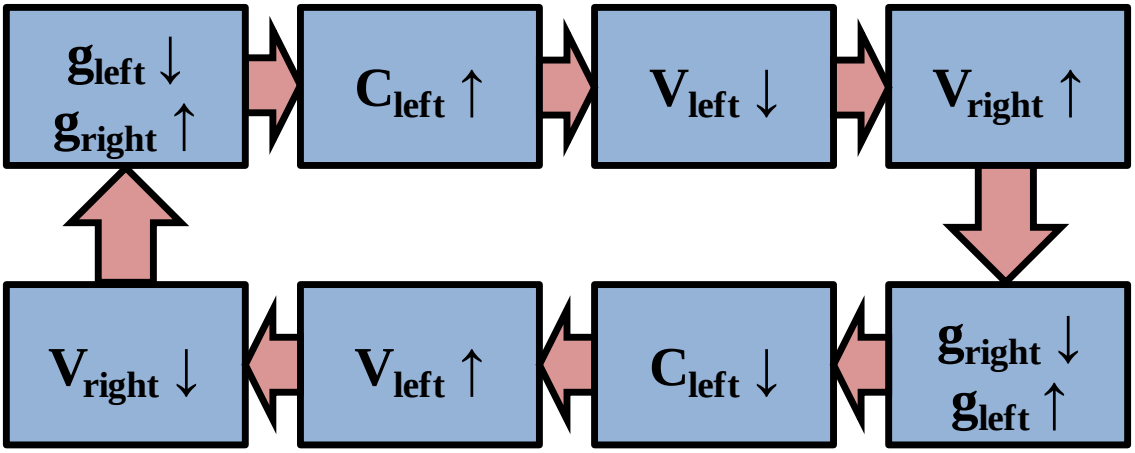

Fig. 4.3. Operating loop cycle of the feedback MEMS oscillator.

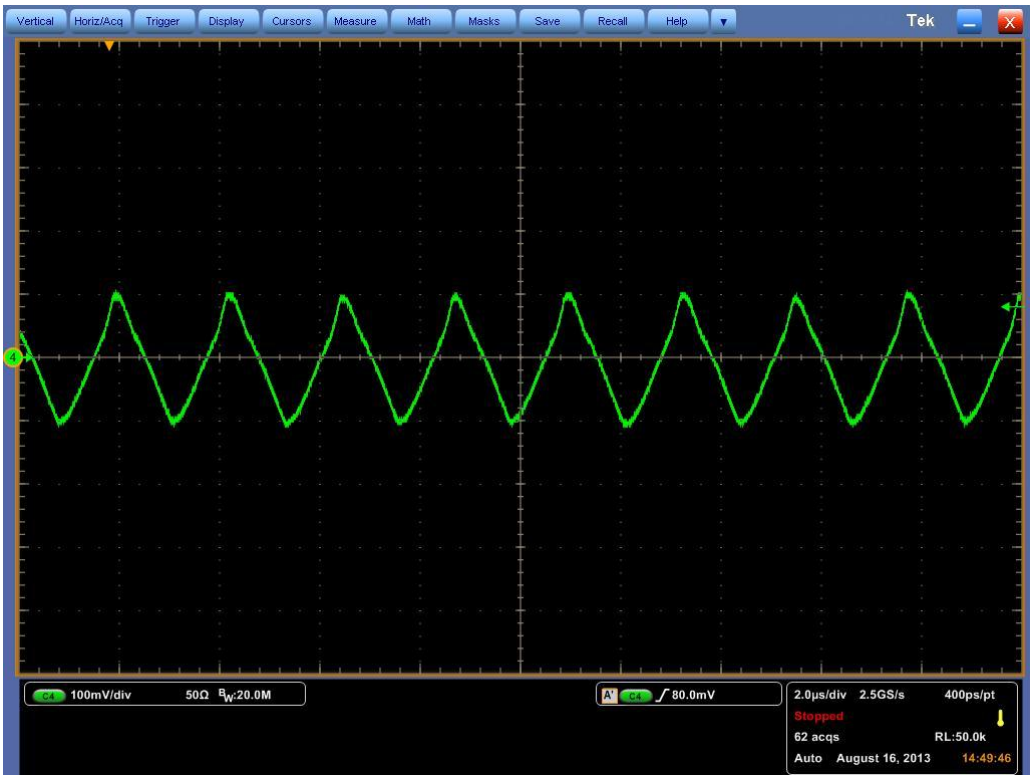

(a)

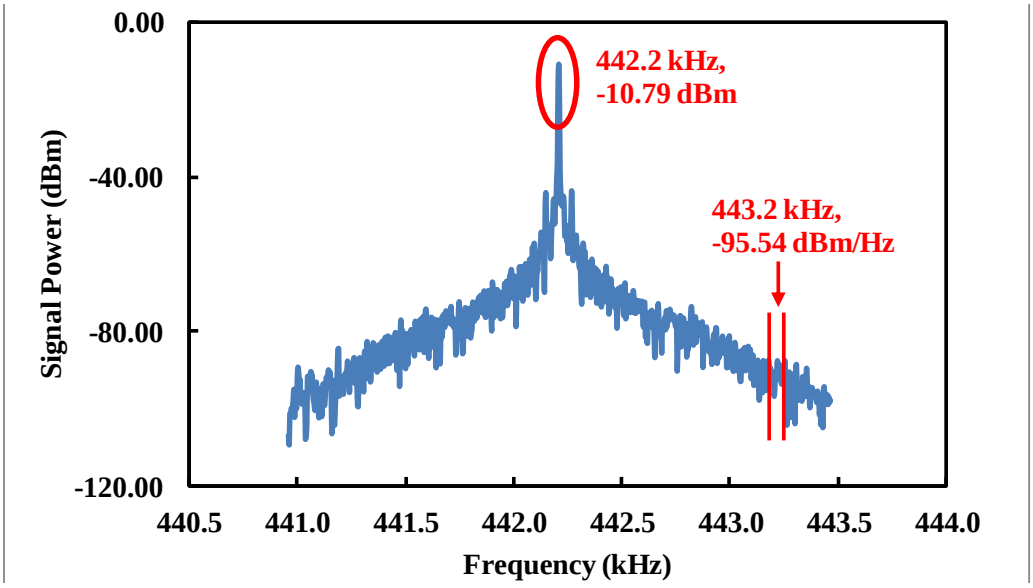

(b)

Fig. 4.4. Oscillator output RF signal characteristics. a) Output time domain oscillation waveform with 33 V DC biasing. b) Output signal power spectra with 33 V DC biasing showing peak frequency of 442.2 kHz, and phase noise of -84.75 dBc/Hz at 1 kHz offset.

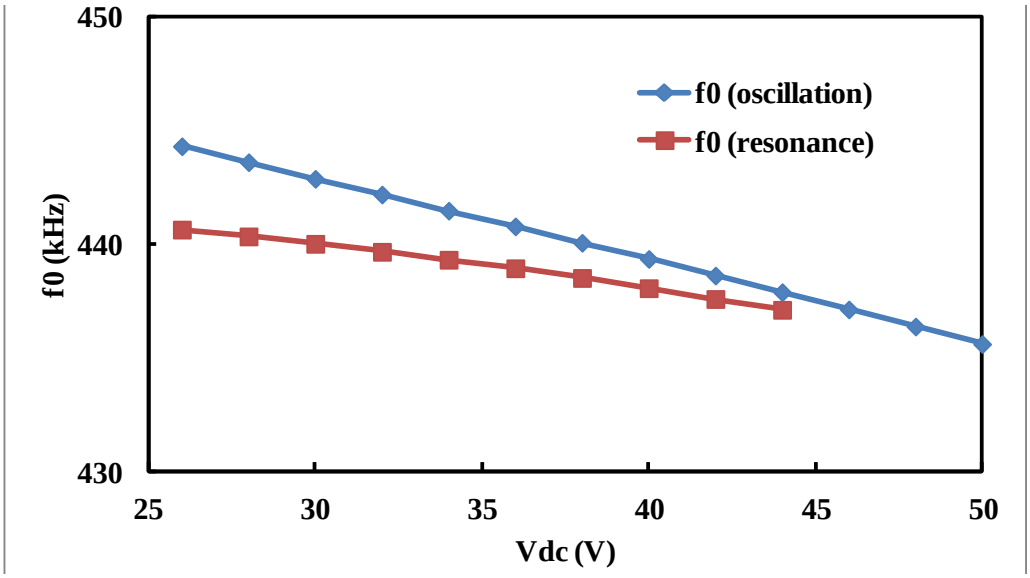

Fig. 4.5. Resonance frequencies and oscillation frequencies as a function of V_{DC} for the 200 μm long microbridge under 10 mTorr.

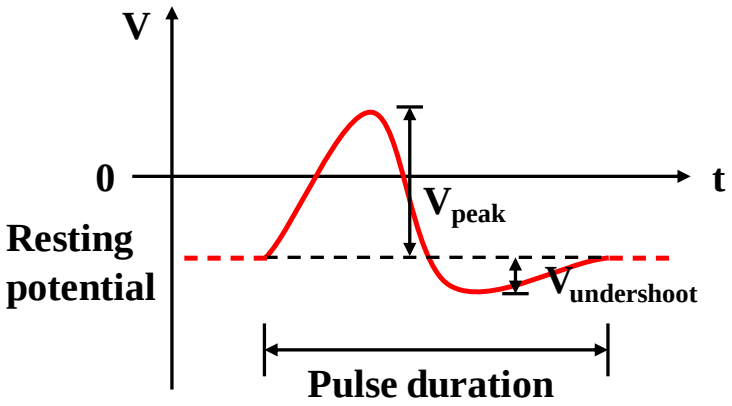

(a)

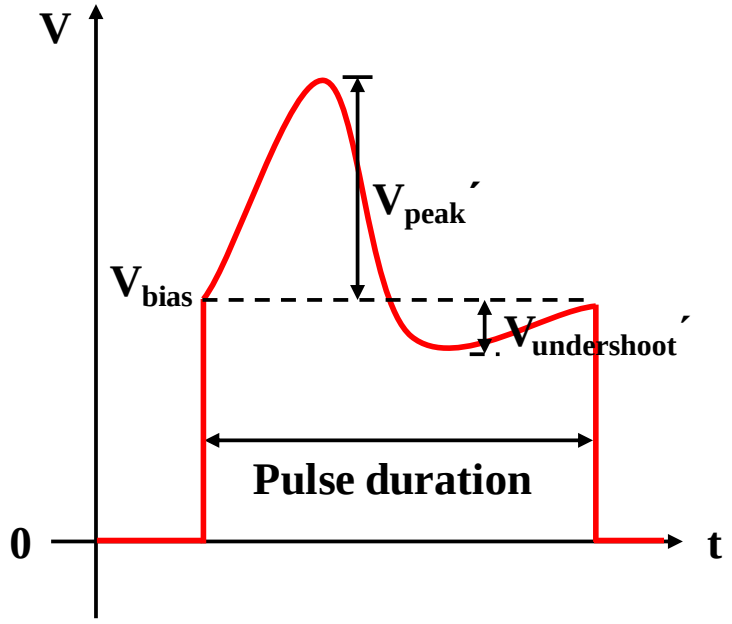

(b)

Fig. 4.6. Features of neural signal waveform. a) Original neural signal. b) Amplified and biased neural signal acting as DC biasing of the MEMS oscillator to form the action-potential-to-RF module.

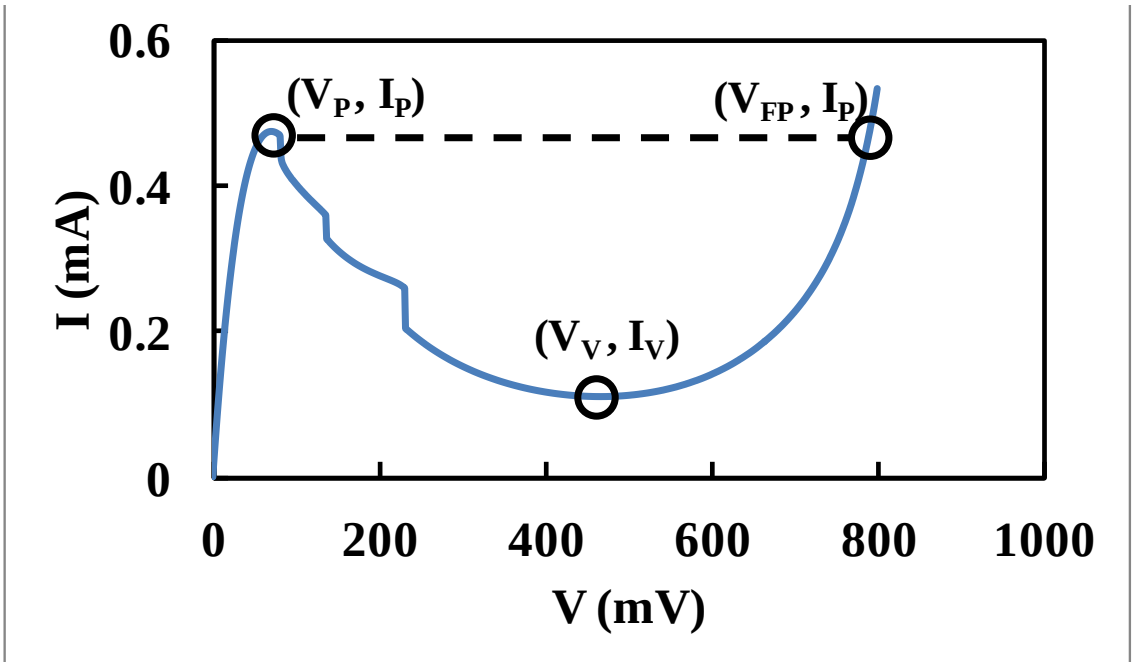

Fig. 4.7. I-V characteristics for tunnel diode 1N3561.

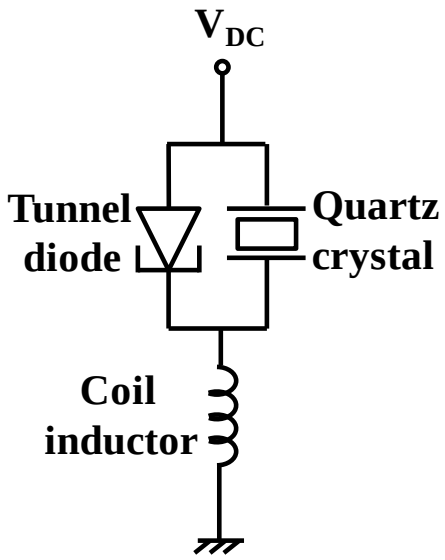

Fig. 4.8. Tunnel diode based oscillation circuit with frequency locking by quartz crystal.

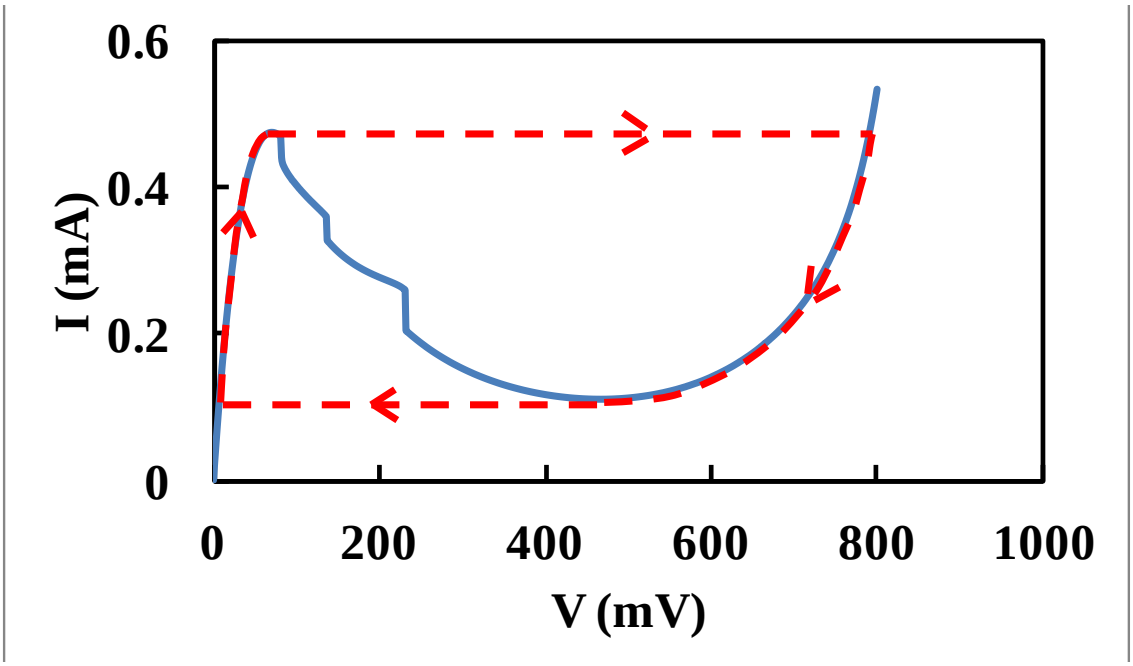

Fig. 4.9. Trajectory of I-V for tunnel diode oscillation circuit.

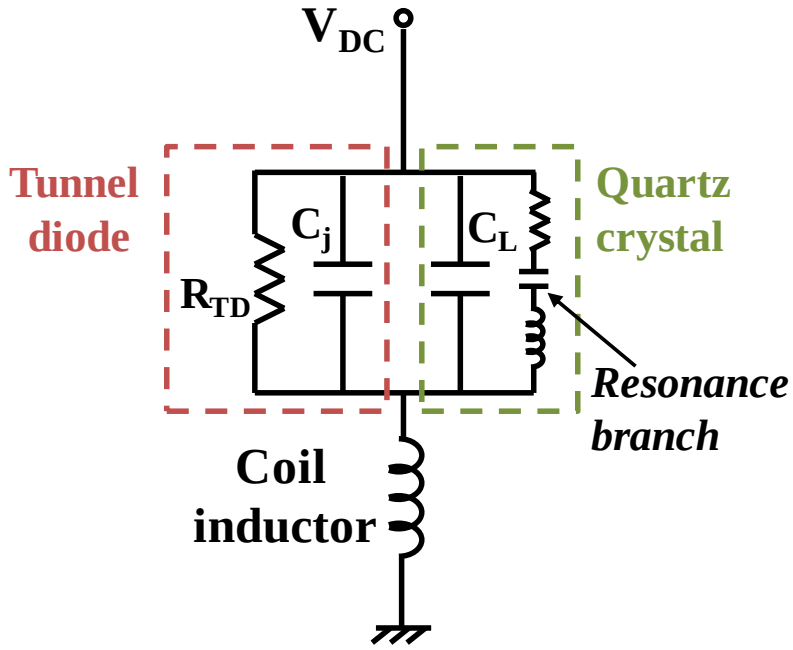

Fig. 4.10. Circuit model of quartz crystal based tunnel diode oscillation circuit.

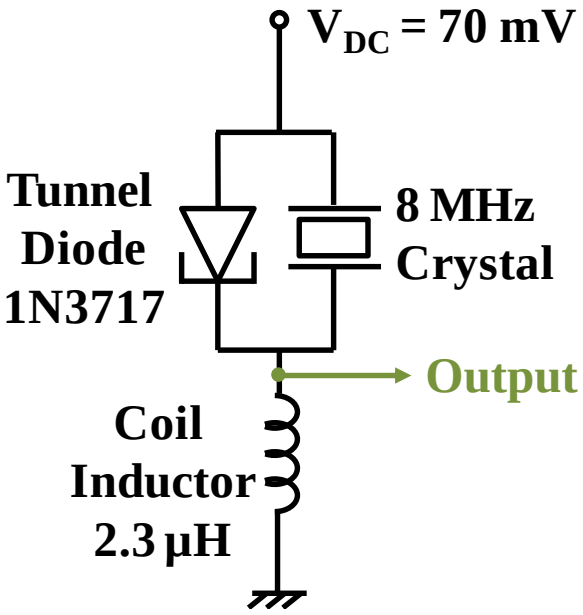

Fig. 4.11. A 8 MHz tunnel diode oscillation circuit.

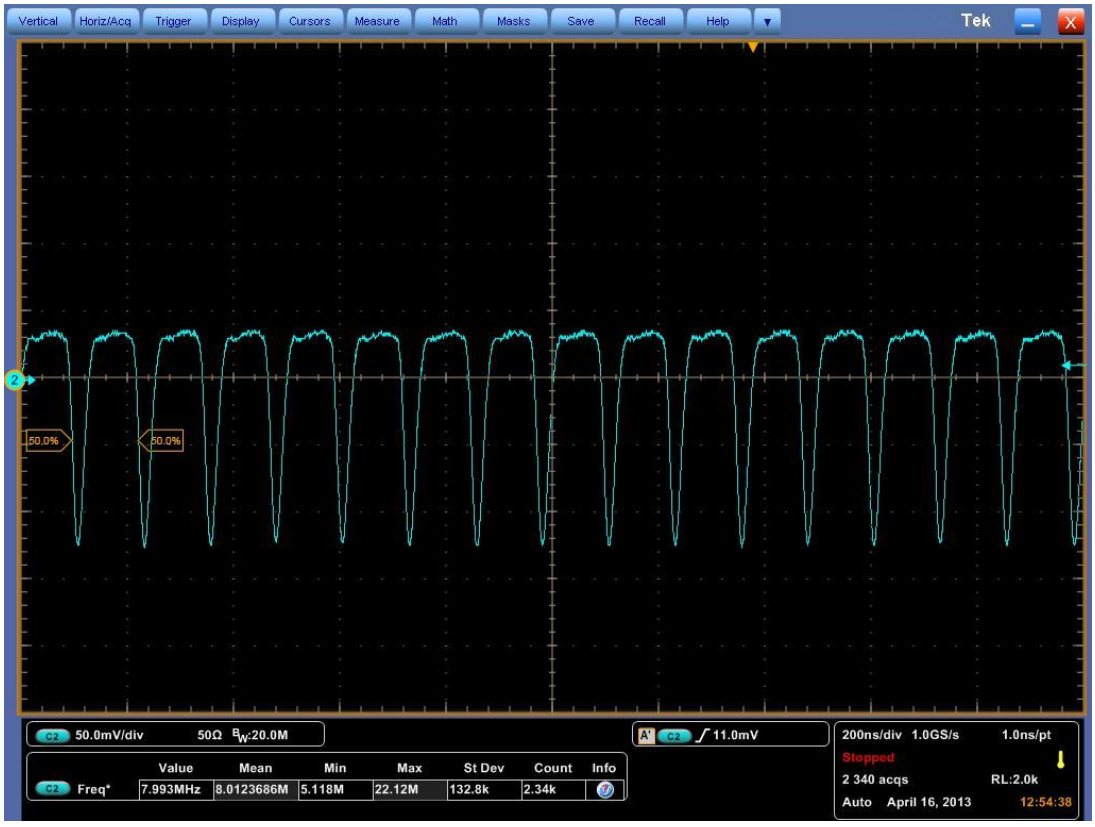

Fig. 4.12. 8 MHz oscillation waveform from tunnel diode circuit.

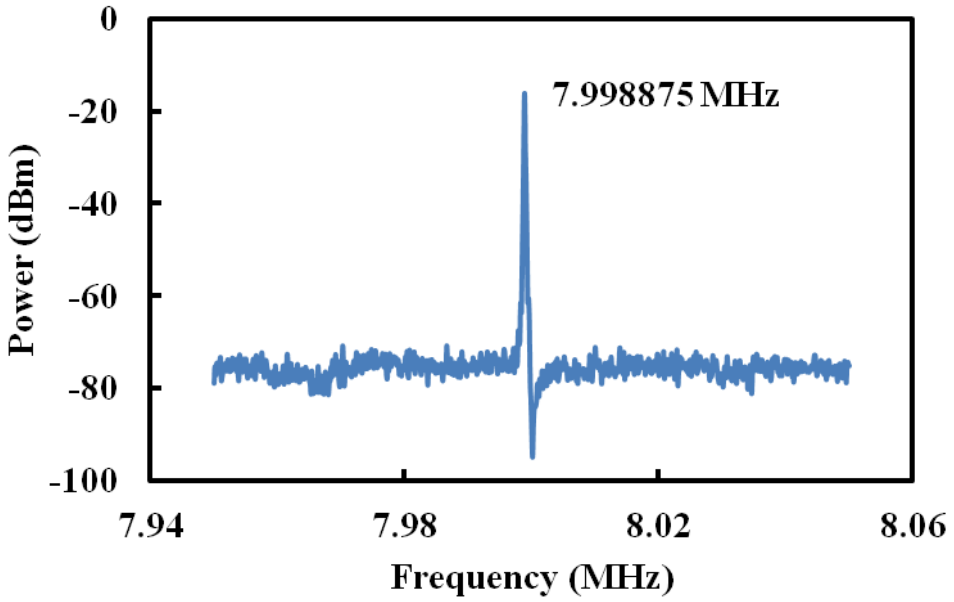

Fig. 4.13. 8 MHz oscillation spectra from tunnel diode circuit.

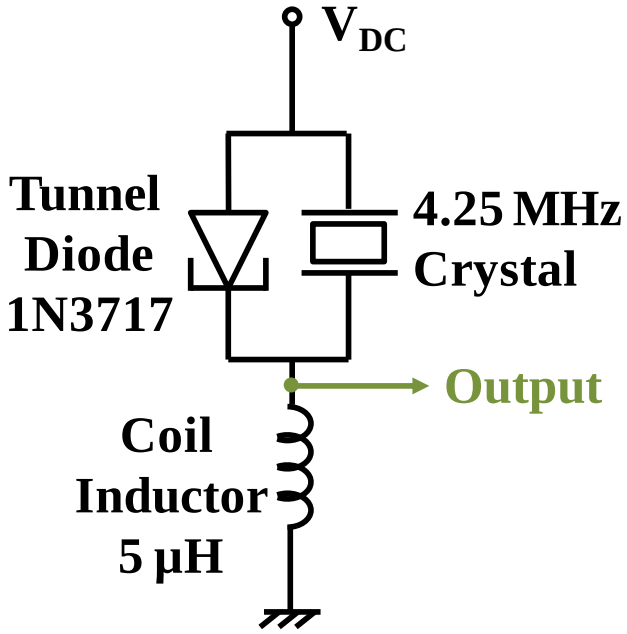

Fig. 4.14. A 4.25 MHz tunnel diode oscillation circuit for characterization of V_{DC} tuning.

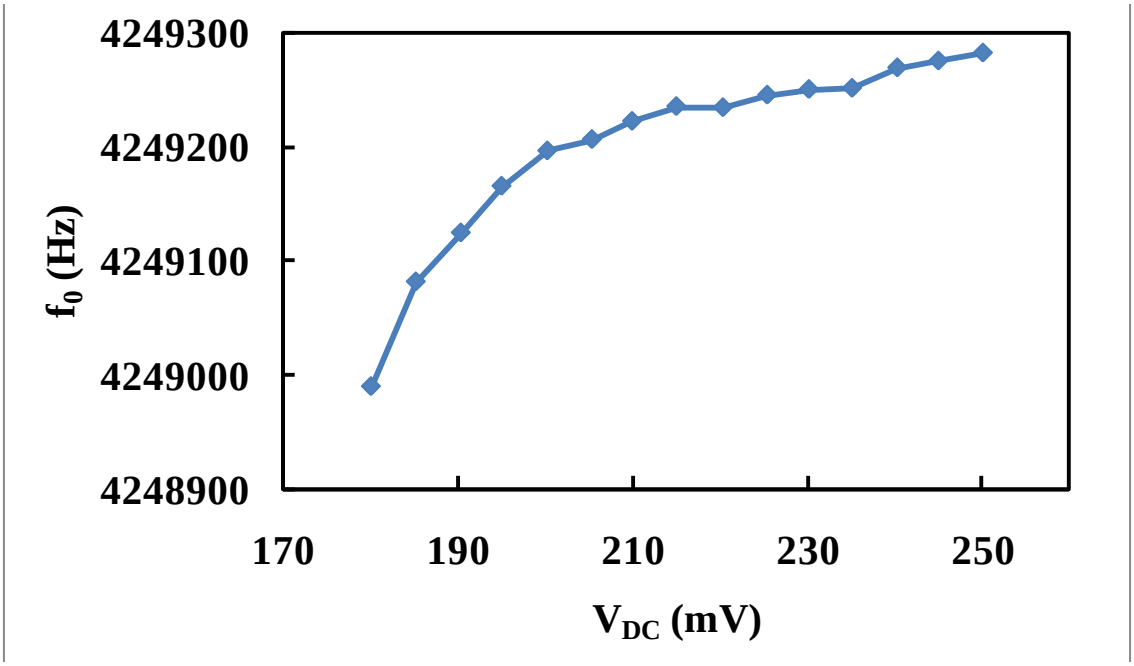

Fig. 4.15. Resonance frequency f_0 versus V_{DC} for quartz based oscillation circuit.

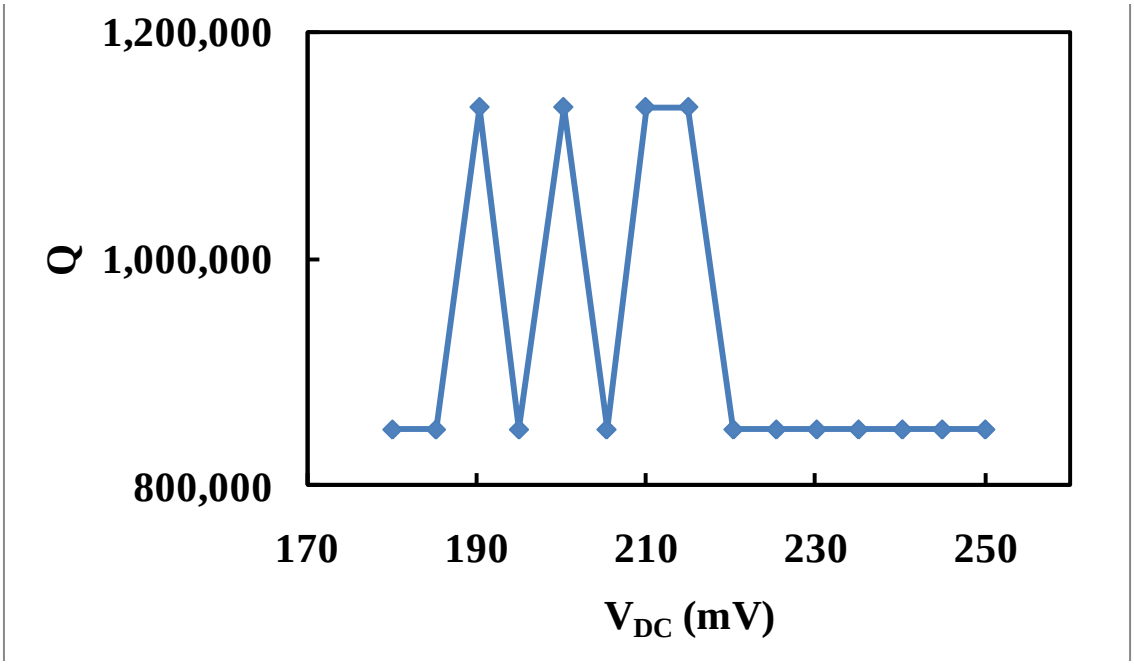

Fig. 4.16. Quality factor Q versus V_{DC} for quartz based oscillation circuit.

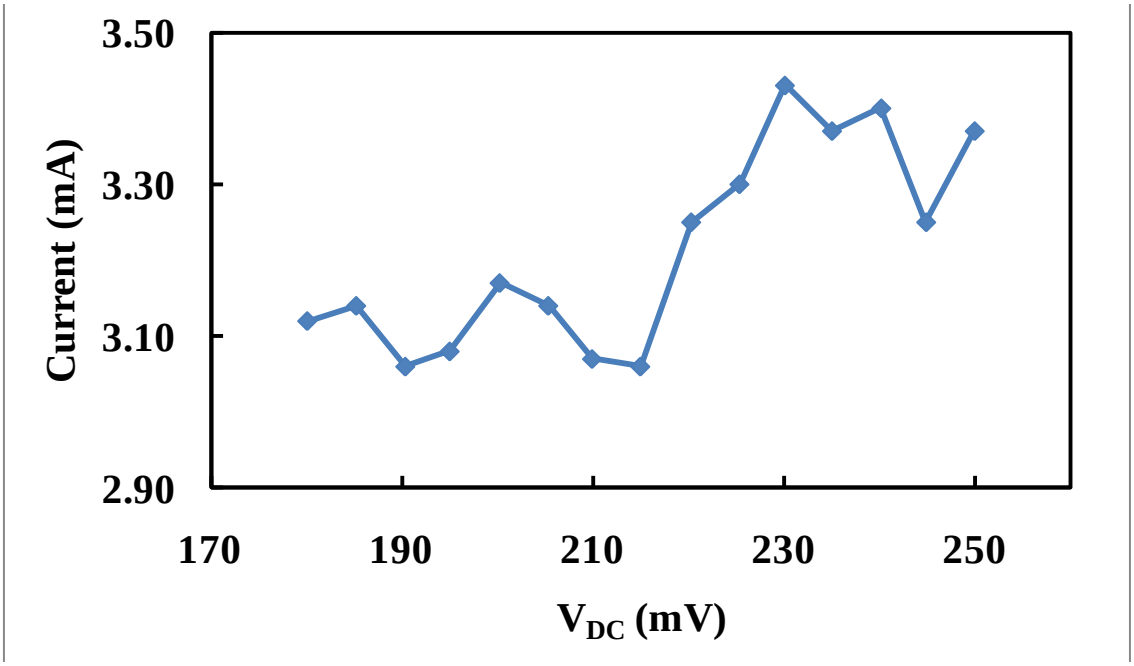

Fig. 4.17. Circuit current consumption versus V_{DC} for quartz based oscillation circuit.

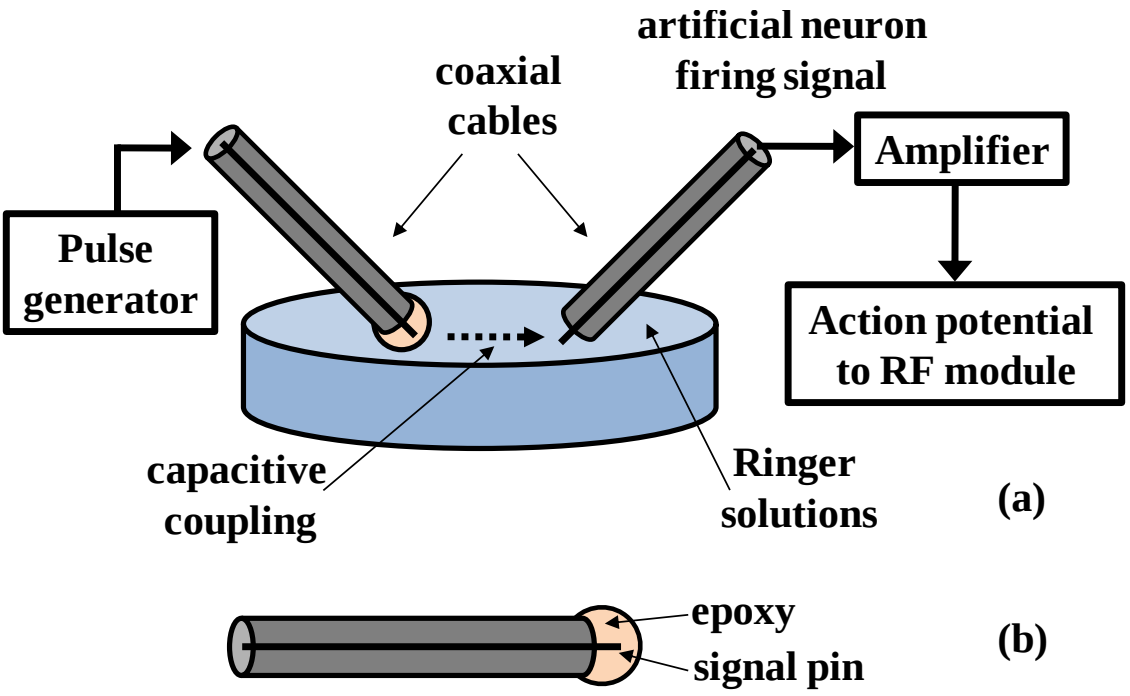

Fig. 4.18. Artificial neural signal generation set-up using coaxial cables. a) Schematic and b) detailed view.

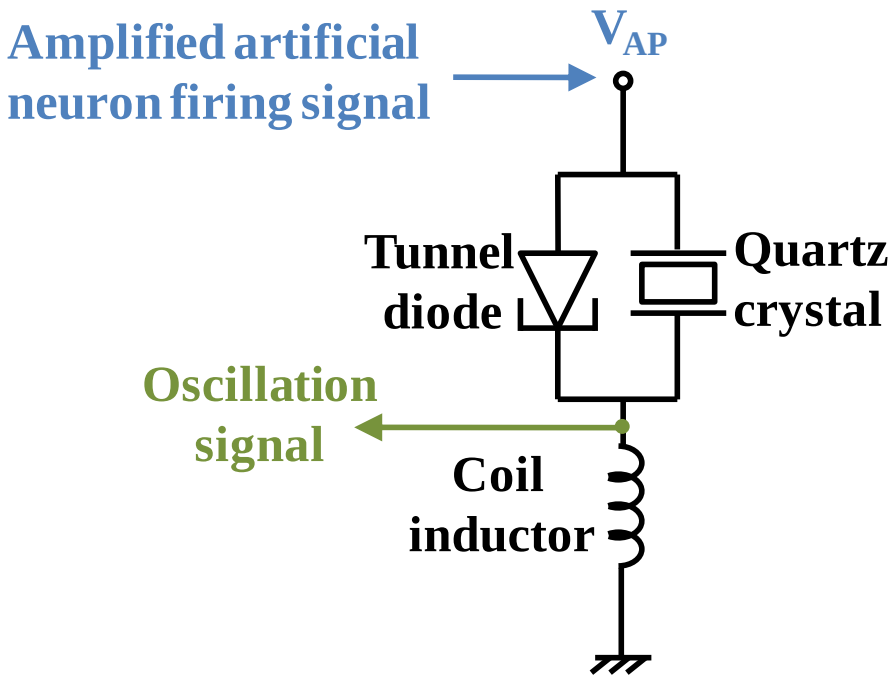

Fig. 4.19. Neuron action potential detection system based on tunnel diode circuit.

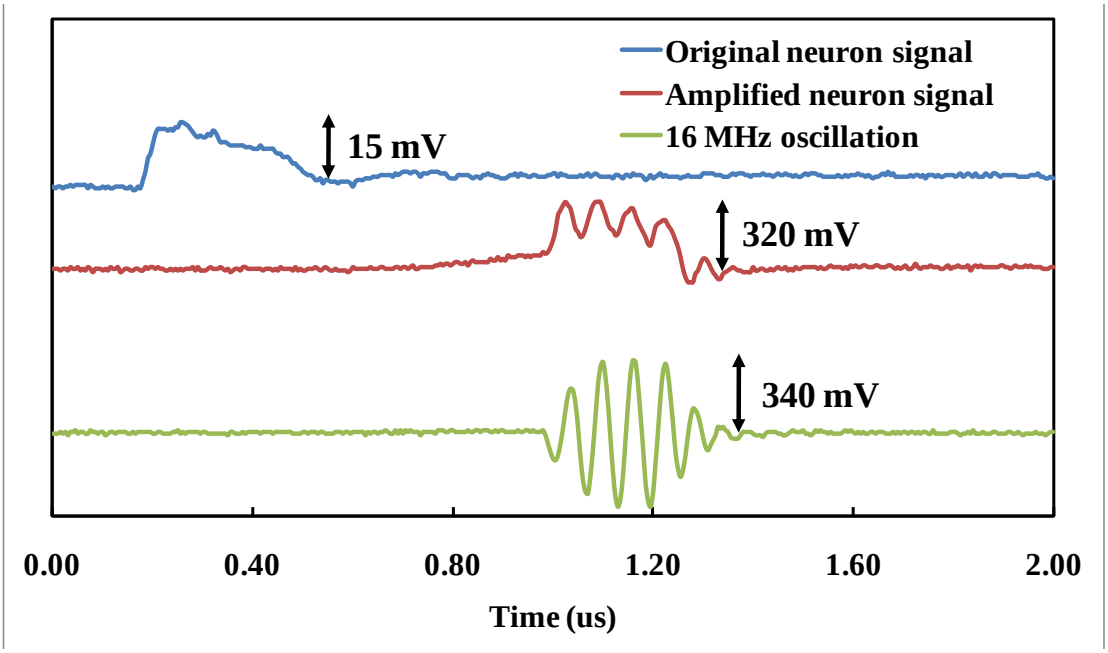

Fig. 4.20. Artificial neuron firing signals (original and amplified) and the modulated oscillations driven by positive neuron firing pulses. Voltage axis is not to scale.

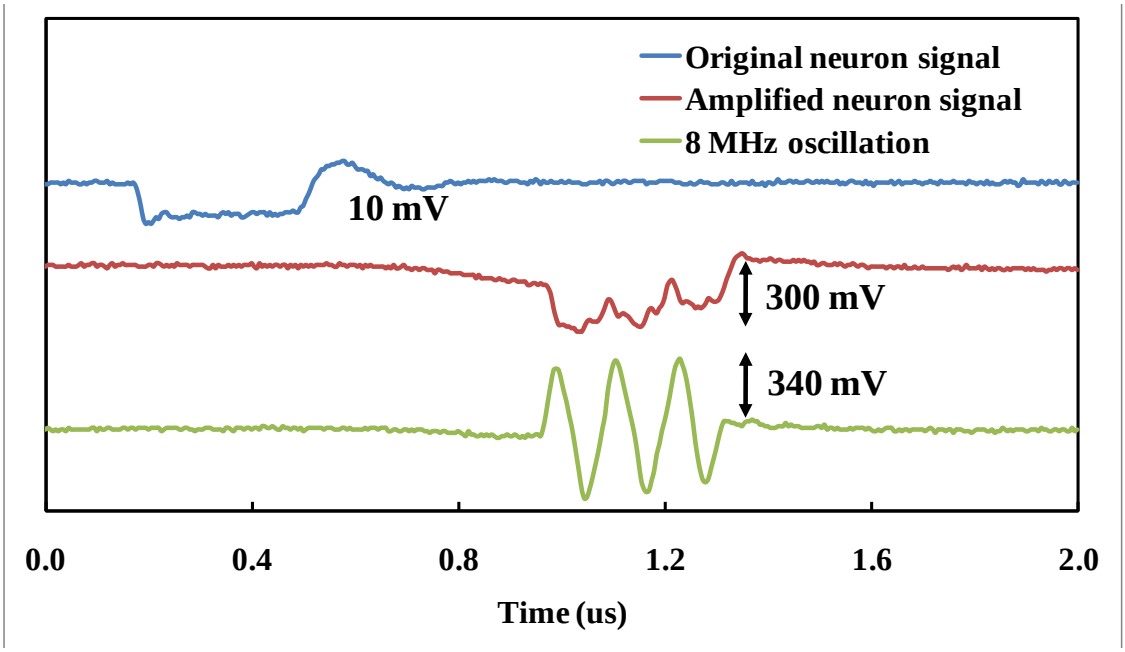

Fig. 4.21. Artificial neuron firing signals (original and amplified) and the modulated oscillations driven by negative neuron firing pulses. Voltage axis is not to scale.

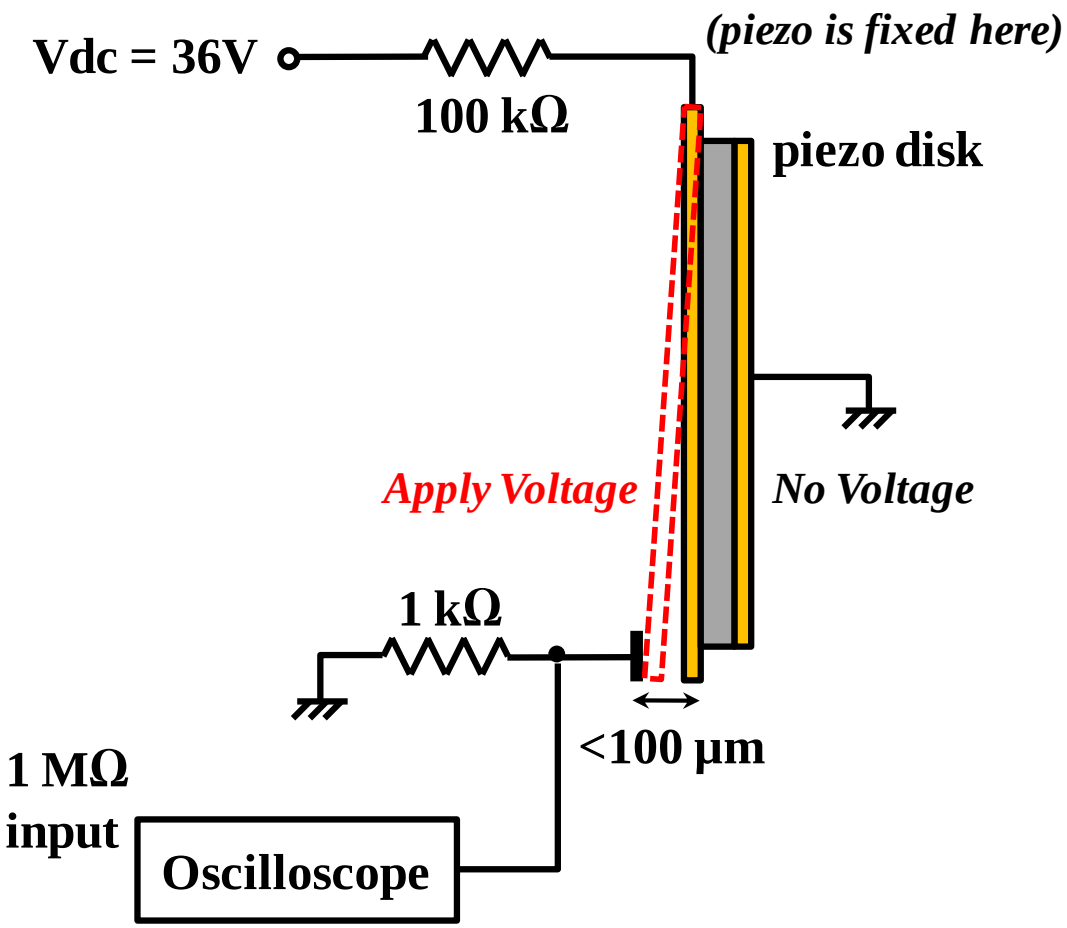

Fig. 4.22. Circuits for piezoelectric material based relaxation oscillator.

Fig. 4.23. Oscillation waveform of piezoelectric disk based relaxation oscillator.

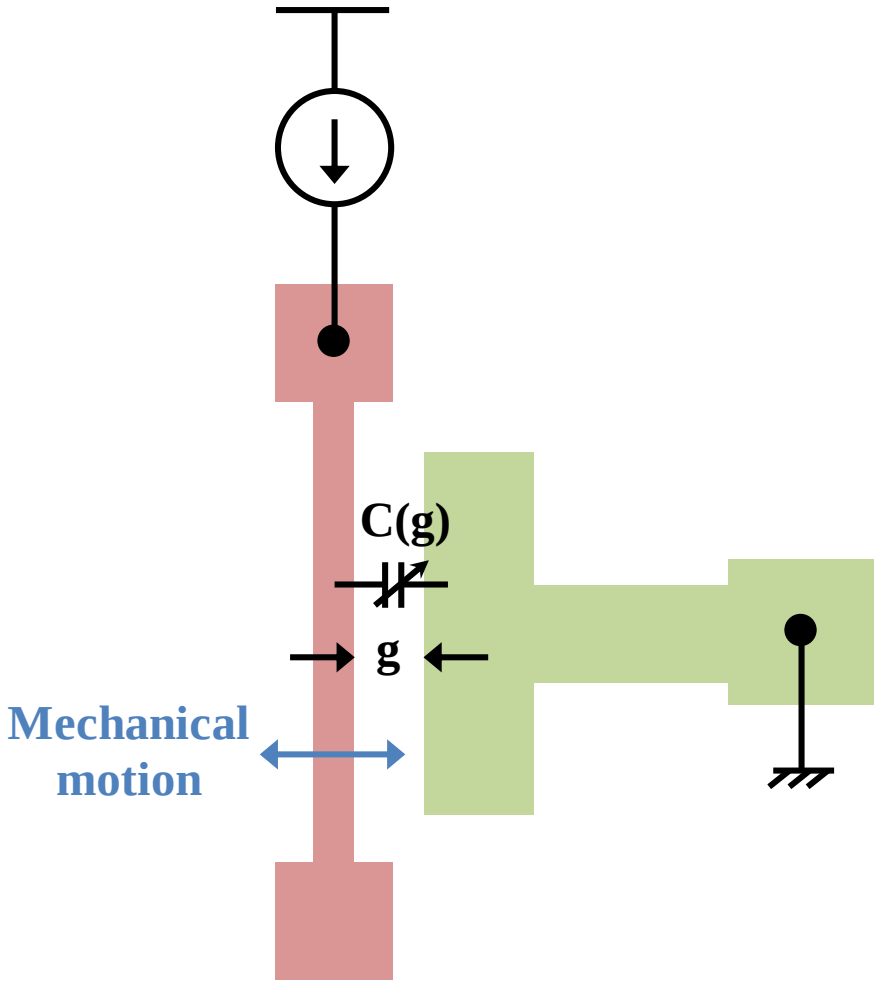

Fig. 4.24. MEMS DC-to-RF circuit.

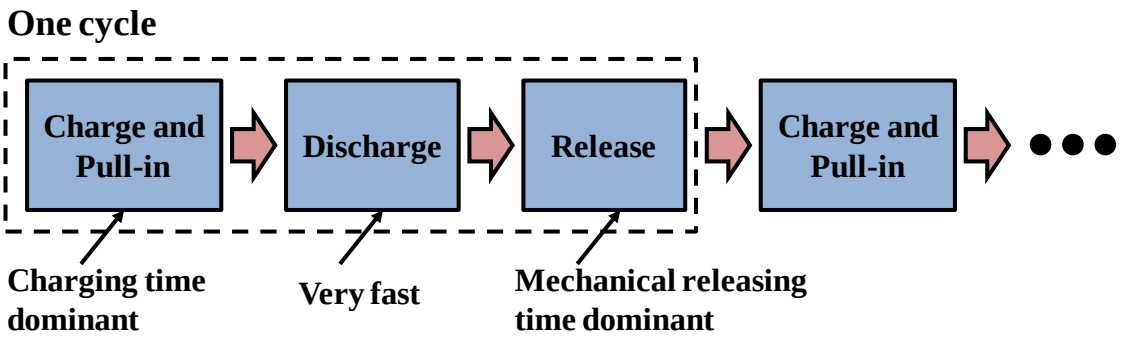

Fig. 4.25. Operating cycles of the MEMS DC-to-RF device.

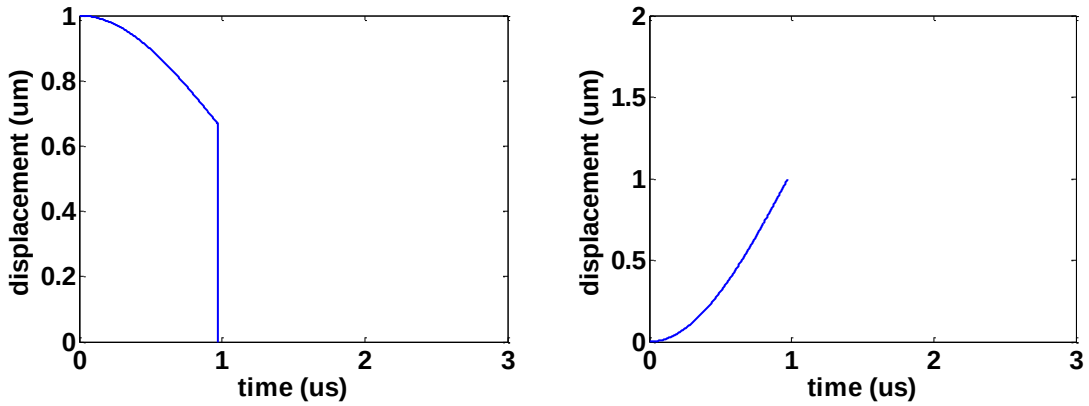

(a) (b)

Fig. 4.26. Bridge position versus time for pure mechanical a) pull-in, b) release, with TiW bridge of 300 µm long, 5 µm wide, 1 µm thick, and quality factor of 2,000.

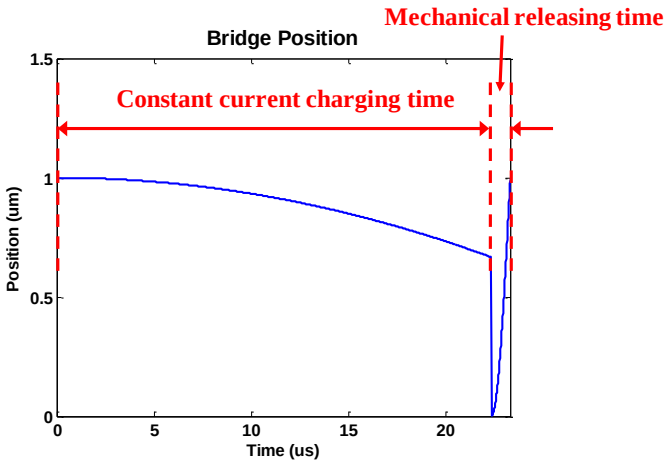

(a)

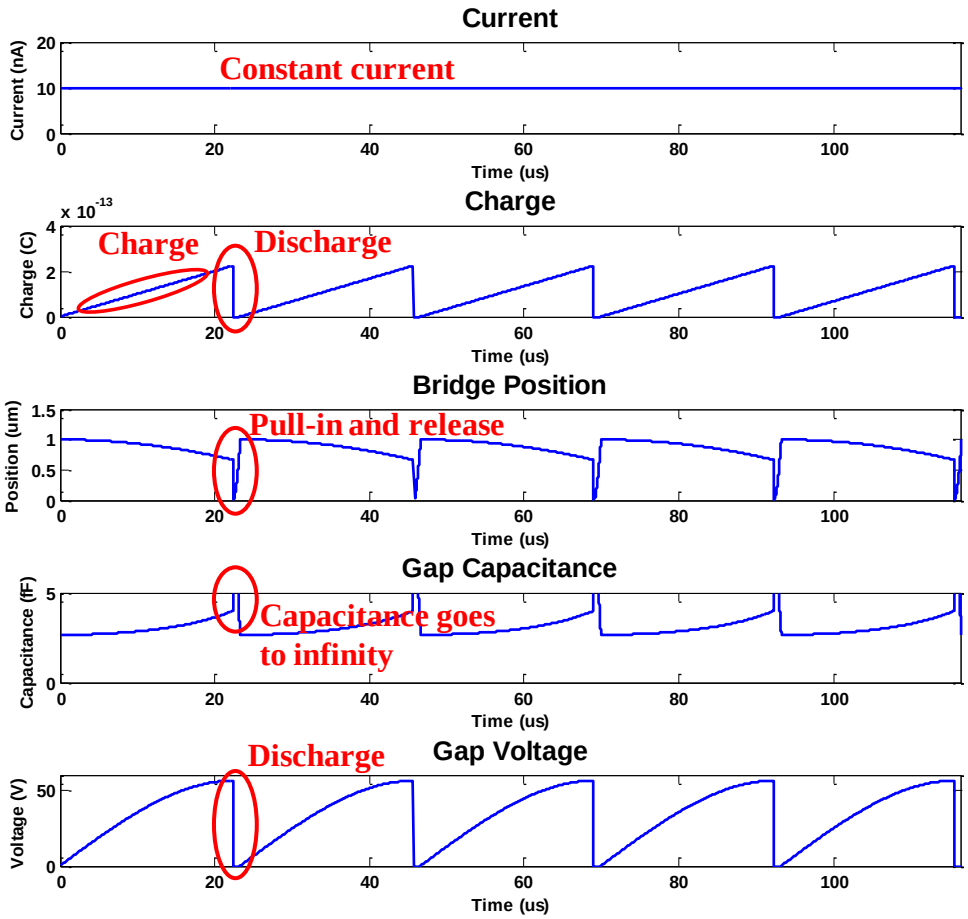

(b)

Fig. 4.27. Simulation results of the relaxation oscillator. a) Bridge position versus time showing electrical charging and mechanical releasing time. b) Current, charge, bridge position, gap capacitance and gap voltage versus time for sustainable oscillation.

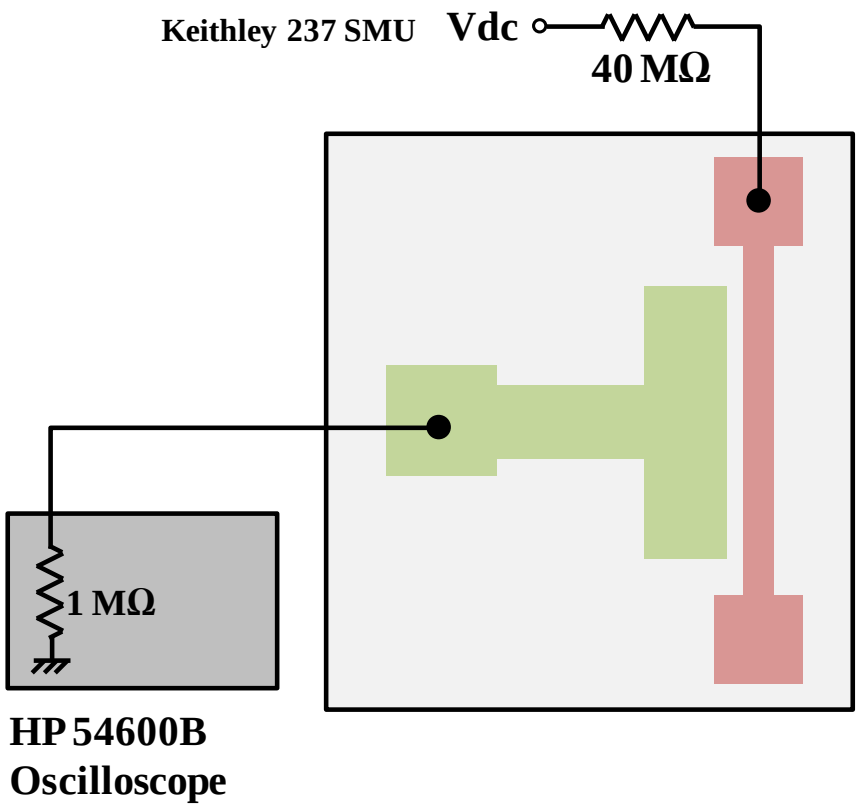

Fig. 4.28. Experimental set-up of MEMS DC-to-RF conversion.

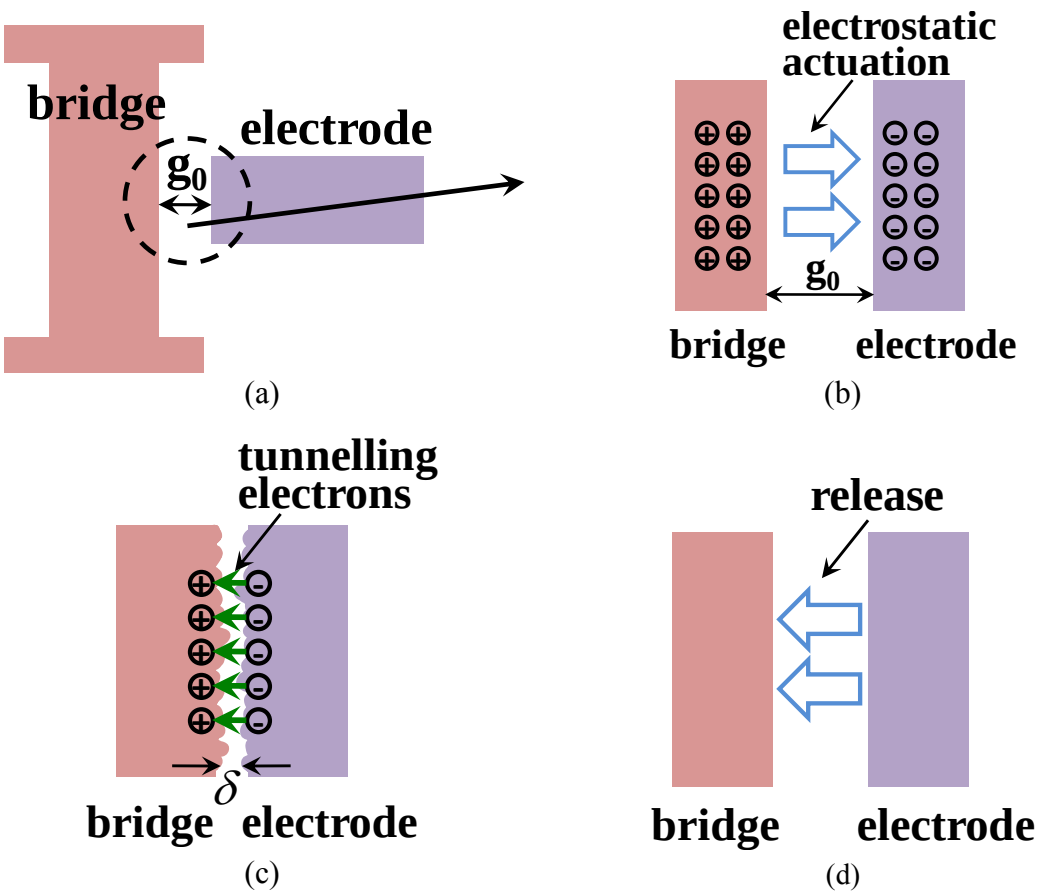

Fig. 4.29. Operation principles of the MEMS relaxation oscillator. a) Bridge-electrode pair with gap g_0. b) Constant-charge bridge clamping due to electrostatic actuation. c) Tunneling current discharge when gap δ is very small. d) Mechanical release of the bridge.

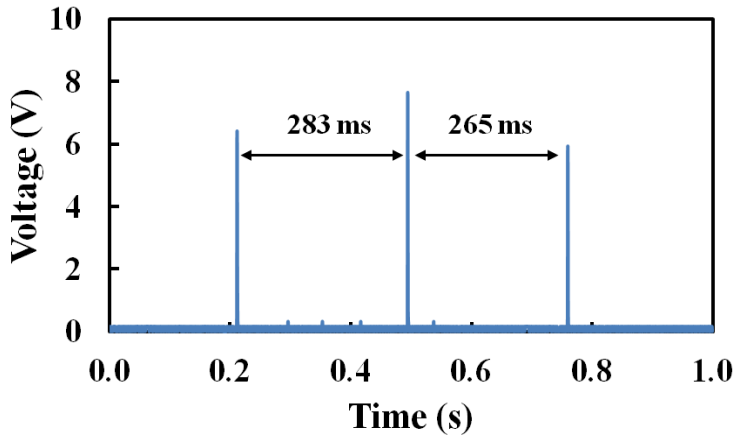

Fig. 4.30. Self-sustained pulsed oscillation waveform of a 300 μm long MEMS bridge.

4.7 References

[1] E.P. Quevy and R.T. Howe, "Redundant MEMS resonators for precise reference oscillators," *Digest of Papers - IEEE Radio Frequency Integrated Circuits Symposium*, Long Beach, CA, USA, pp. 113-116, 2005.

[2] C. Nguyen, "Integrated micromechanical circuits fueled by vibrating RF MEMS technology," *Proceedings - IEEE Ultrasonics Symposium*, Vancouver, BC, Canada, pp. 953-962, 2006.

[3] H.G. Barrow, T.L. Naing, R.A. Schneider, T.O. Rocheleau, V. Yeh, Z. Ren and C. Nguyen, "A real-time 32.768-kHz clock oscillator using a 0.0154-mm2 micromechanical resonator frequency-setting element," *2012 IEEE International Frequency Control Symposium, IFCS 2012, Proceedings*, Baltimore, MD, USA, pp. 277-282, 2012.

[4] C. Nguyen and R.T. Howe, "Integrated CMOS micromechanical resonator high-Q oscillator," *IEEE Journal of Solid-State Circuits*, Vol. 34, No. 4, pp. 440-455, 1999.

[5] Y. Lin, S. Lee, Z. Ren and C. Nguyen, "Series-resonant micromechanical resonator oscillator," *Technical Digest - International Electron Devices Meeting, IEDM*, Washington, DC, USA, pp. 961-964, 2003.

[6] K. Sundaresan, G. K. Ho, S. Pourkamali and F. Ayazi, "A two-chip 4-MHz microelectromechanical reference oscillator," *Proceedings - IEEE International Symposium on Circuits and Systems*, Kobe, Japan, pp. 5461-5464, 2005.

[7] W. Huang, Z. Ren, Y. Lin, H. Chen, J. Lahann and C. Nguyen, "Fully monolithic CMOS nickel micromechanical resonator oscillator," *Proceedings of the IEEE International Conference on Micro Electro Mechanical Systems (MEMS)*, Tucson, AZ, USA, pp. 10-13, 2008.

[8] T.L. Naing, T.O. Rocheleau, Z. Ren, E. Alon and C. Nguyen, "Vibration-insensitive 61-MHz micromechanical disk reference oscillator," *2012 IEEE International Frequency Control Symposium, IFCS 2012, Proceedings*, Baltimore, MD, USA, pp. 271-276, 2012.

[9] Y. Lin, S. Lee, S. Li, Y. Xie, Z. Ren and C. Nguyen, "60-MHz wine-glass micromechanical-disk reference oscillator," *Digest of Technical Papers - IEEE International Solid-State Circuits Conference*, San Francisco, CA, USA, Vol. 47, pp. 258-259+562, 2003.

[10] Y. Lin, S. Lee, S. Li, Y. Xie, Z. Ren and C. Nguyen, "Series-resonant VHF micromechanical resonator reference oscillators," *IEEE Journal of Solid-State Circuits*, Vol. 39, No. 12, pp. 2477-2491, 2004.

[11] H. Miri Lavasani, A.K. Samarao, G. Casinovi and F. Ayazi, “A 145MHz low phase noise capacitive silicon micromechanical resonator,” *Technical Digest - International Electron Devices Meeting, IEDM*, San Francisco, CA, USA, pp. 675-678, 2008.

[12] K. Sundaresan, G.K. Ho, S. Pourkamali and F. Ayazi, “A low phase noise 100MHz silicon BAW reference oscillator,” *Proceedings of the Custom Integrated Circuits Conference*, San Jose, CA, USA, pp. 841-844, 2006.

[13] R. Abdolvand, H. Mirilavasani and F. Ayazi, “Single-resonator dual-frequency thin-film piezoelectric-on-substrate oscillator,” *Technical Digest - International Electron Devices Meeting, IEDM*, Washington, DC, USA, pp. 419-422, 2007.

[14] G.K. Ho, K. Sundaresan, S. Pourkamali and F. Ayazi, "Temperature compensated IBAR reference oscillators,” *Proceedings of the IEEE International Conference on Micro Electro Mechanical Systems (MEMS)*, Istanbul, Turkey, pp. 910-913, 2006.

[15] A. Rahafrooz and S. Pourkamali, "Fully micromechanical piezo-thermal oscillators,” *Technical Digest - International Electron Devices Meeting, IEDM*, San Francisco, CA, USA, pp. 7.2.1-7.2.4, 2010.

[16] A. Rahafrooz and S. Pourkamali, "High-frequency thermally actuated electromechanical resonators with piezoresistive readout,” *IEEE Transactions on Electron Devices*, Vol. 58, No. 4, pp. 1205-1214, 2011.

[17] H.J. Hall, A. Rahafrooz, J.J. Brown, V.M. Bright and S. Pourkamali, "Thermally actuated I-shaped electromechanical VHF resonators,” *Proceedings of the IEEE International Conference on Micro Electro Mechanical Systems (MEMS)*, Paris, France, pp. 737-740, 2012.

[18] A. Rahafrooz and S. Pourkamali, “High frequency dual-mode thermal-piezoresistive oscillators,” *Proceedings of the IEEE International Frequency Control Symposium and Exposition*, San Francisco, CA, USA, 2011.

[19] A. Hajjam, A. Rahafrooz and S. Pourkamali, “Temperature compensated single-device electromechanical oscillators,” *Proceedings of the IEEE International Conference on Micro Electro Mechanical Systems (MEMS)*, Cancun, Mexico, pp. 801-804, 2011.

[20] M. Suster, W.H. Ko and D.J. Young, "An optically powered wireless telemetry module for high-temperature MEMS sensing and communication,” *Journal of Microelectromechanical Systems*, Vol. 13, No. 3, pp. 536-541, 2004.

[21] C.T. Van Degrift and D.P. Love, "Modeling of tunnel diode oscillators,” *Review of Scientific Instruments*, Vol. 52, No. 5, pp. 712-723, 1981.

[22] L. Chen and M. Tabib-Azar, "Neuron action potential detection with tunnel diode oscillation circuit," presented at *IEEE Sensors 2012*, Taipei, Taiwan, 2012.

[23] D. Gao, C. Carraro, R.T. Howe and R. Maboudian, "Polycrystalline silicon carbide as a substrate material for reducing adhesion in MEMS," *Tribology Letters*, Vol. 21, No. 3, pp. 226-232, 2006.

[24] D. Gao, W.R. Ashurst, C. Carraro, R.T. Howe and R. Maboudian, "Silicon carbide for enhanced MEMS reliability," *2004 Solid-State Sensors, Actuators, and Microsystems Workshop*, Hilton Head, SC, USA, pp. 192-195, 2004.

CHAPTER 5

RF COIL LINK FOR POWER AND DATA COMMUNICATIONS

5.1 Overview

Wireless power and data transmission are essential in a brain interfacing system. Transcutaneous powering, i.e., power transmission through the skin, is the objective we tried to achieve. In general, there are four types of wireless power transmission: radiative, conductive, capacitive and inductive [1].

Radiative transmission is essentially electromagnetic (EM) radiation. The receiver is usually located in the far-field. The generated EM wave from the source transmits on its own, without coupling between the transmitter and receiver. The antenna works the best when its dimension is a large fraction of the transmission wavelength. Considering the size restraints of the implanted system, the frequency should be in the range of tens of GHz. At this high frequency, power absorption by biological tissues is huge, and therefore there is large attenuation. Besides, implementation of a transmitter operating at tens of GHz is rather complex. Hence, radiative transmission is not a feasible option for transcutaneous powering.

Conductive power transmission requires a conductive medium to conduct current, like salty water. Near-field operation is usually adopted, while the transmission distance is short compared to the wavelength. A very similar way is capacitive power transmission. The only major difference is that the AC signal is needed in capacitive transmission (not necessary in conductive transmission), and hence a nonconductive medium can be used (like air gap or some biological tissues). However, for both of these two power transmission types, current will directly flow through the medium, the biological tissues. This introduces limitations on current density and power dissipated in the human body, and raises problems on health and safety regulations. Consequently, both conductive and capacitive power transmission are not suitable for transcutaneous powering.

This leaves us with only one choice: inductive power transmission. It is based on a magnetic induced electrical field. The distance and dimensions are short compared to a wavelength, and this method operates in the near-field. Inductive power transmission relies on strong inductive magnetic coupling, unlike the radiative power transmission (transmitter and receiver have no coupling). Inductive transmission usually operates under 10 MHz (with reasonable sizes for both implanted and external systems), in which power absorption by the human body is very small. Besides, unlike conductive/capacitive transmission, current in the passing and surrounding biological tissues is much less significant in inductive transmission. Major current distribution only exists in the high conductive induction coils, therefore, no stringent health safety restrictions exist.

In conclusion, considering system dimensions, power transfer efficiency and health safety regulations, inductive power transmission is the most appropriate type for

transcutaneous powering. The same arguments can be made for data transmission as well, only with a different transceiving direction (from the implanted system to the external system).

Lots of work has been done in transcutaneous powering with inductive coupling. The most common form of two-coil set-up has been thoroughly tested and analyzed [2-7]. Wang et al. [8] used ferrite-core coil in the implanted system for animal brain stimulation, achieving a transmission distance of 200 mm. Young [9] realized an adaptive RF powering system for biosensing microsystems implanted in untethered animals inside a cage, with RF power level information feedback, achieving stable DC power supply in the implanted system. RamRakhyani et al. [10-11] modeled and implemented a four-coil energy transfer system for biomedical implant applications. They used the architecture of driver-primary coil pairs and secondary-load coil pairs (total of four coils) and demonstrated a system with a transmission distance of 20 mm.

For this thesis work, we used air-core coils for the wireless powering and data communication of the neural interfacing system. Powering and data communication used frequencies several orders of magnitude apart to avoid interference. The following sections illustrate the design and realization of a highly-efficient coil telemetry link, with very small implanted coil (0.6 mm radius) and long distance (more than 40 mm) inductive coupling, suitable for both powering and data communications.

5.2 RF Link with Two Coils

We started with a simple two coils energy transmission. The transmission coil (called TX) was designed to be a large coil located outside the brain. The receiving coil (called

RX), on the other hand, would be very small since it would be implanted inside the skull. Radius of the RX coil was fixed at 0.6 mm, giving a 1.2 mm diameter, which is reasonably small for implantation. Both TX and RX coils were solenoid coils.

Both coils were placed inside parallel LC circuits, designed to have same resonance frequency for optimized energy transferring efficiency. The inductance of a solenoid is

$$L = \frac{\mu N^2 A}{l} \tag{5.1}$$

where μ, N, A and l are core permeability, number of turns, coil area and the height of coil (distance from the first turn to the last turn), respectively. Inductances of both coils were made to be 1.2 μH. Apparently, TX coil (large area) has a fewer number of turns than RX coil (small area). Both TX and RX coils were shunt with 100 nF tantalum capacitors. S11 reflection spectrum of the coils has been tested with a network analyzer (Agilent 4395A 10 Hz – 500 MHz Network Analyzer), as shown in Fig. 5.1, with peak at 455 kHz (for parallel LC circuits, impedance reaches maximum at resonance, and therefore maximum S11 value). S11 for both TX and RX coils were measured to ensure they have the same resonance frequencies.

The testing circuits for the two coil RF link is shown in Fig 5.2 [12]. A signal generator (Hewlett Packard 33120A 15 MHz Function/Arbitrary Waveform Generator, 50Ω output) provided power to the TX circuits, at 455 kHz (resonance frequency), with 10 V peak-to-peak. A digital oscilloscope (Tektronix DPO 7254 Digital Phosphor Oscilloscope, 50Ω input) read the output from the RX circuits. TX coils of different sizes were placed at different distances from RX coil (Fig. 5.3), and the output voltages (V_{out} of RX circuits) versus distance were obtained when RX coil was in a fixed position with 0.6 mm radius.

Fig. 5.4 shows the output peak-to-peak voltage as a function of TX coil's location for different radii of TX coils (all much larger than RX coil's) [12]. It can be seen that the smaller the TX coil radius (R_{TX}), the steeper the curves are, i.e., faster V_{out} attenuates with distance. Another thing to note is that for each TX – RX distance Z_{RT}, there exists an optimized R_{TX} for achieving maximum V_{out}. For example, for Z_{RT} < 13 mm, optimized TX coil has R_{TX} = 5 mm; for 13 mm < Z_{RT} < 28 mm, optimized TX coil has R_{TX} = 15 mm; for Z_{RT} > 28 mm, optimized TX coil has R_{TX} = 30 mm… meaning that the larger the TX – RX distance, the larger the TX coil needs to be to have optimized transmission, though apparently the optimized V_{out} decreases with the distance.

The above results can be explained by magnetic dipole theory. When R_{TX} >> R_{RX},

$$V_{out} = N_{RX} \frac{\mu_0 N_{TX} {R_{TX}}^2 \pi {R_{RX}}^2}{2\left({R_{TX}}^2 + {Z_{RT}}^2\right)^{3/2}} \frac{di}{dt}. \tag{5.2}$$

where N_{RX} and N_{TX} are the number of turns for the RX and TX coils, respectively, and i is the value of current through TX coil (detailed derivations in Appendix A). The equation has R_{TX} in both numerator and denominator, and it is easy to find that the optimized R_{TX} is proportional to Z_{RT}, which confirms the experimental results. Also, the behavior of V_{out} as a function of Z_{RT} follows the $1/{Z_{RT}}^3$ law when Z_{RT} >> R_{TX}, as expected.

5.3 RF Link with Three Coils

The power transfer efficiency at Z_{RT} = 70 mm, for R_{TX} = 30 mm was only 1.2×10^{-6} (based on V_{out} of 11 mV and input voltage of 10 V), which is very low. We need a way to boost the energy coupling efficiency for the brain interfacing system.

Inspired by the phenomenon of electromagnetically induced transparency (EIT), a way of enhancing energy coupling efficiency between two resonant objects by introducing a mediating resonant object with the same resonance frequency has been proposed and analyzed [14-16]. Hamam et al. [14] and Kim et al. [16] proved the enhancement of energy transfer efficiency with temporal coupled mode theory (CMT) [13]. We adopted the idea of introducing a mediating resonant object into the inductive coupling of the RF link in the hope of realizing much higher coupling efficiency.

The same testing set-up of two coil RF link was used, except a third, intermediate coil (called IM) was added (Fig. 5.5) [12]. Observing the EIT analog, the IM coil circuits were designed to have the same resonance frequency as the TX and RX. TX and RX coils were at fixed positions, with distance of 70 mm. TX and RX coils have radii of 44.5 mm and 0.6 mm, respectively. IM coils of different sizes were placed in-between TX and RX coils as shown in Fig. 5.6 ($Z_{RT} = Z_{RM} + Z_{MT}$), and the output voltages (V_{out} of RX circuits) versus IM coil location Z_{RM} (between IM and RX coils) were obtained.

Fig. 5.7 shows the output peak-to-peak voltage versus IM coil's location for different IM radii [12]. The tested radius of IM coil R_{IM} was always larger than R_{RX}, but can be either smaller or larger than R_{TX}. It can be seen that when there was no IM coil, the transmitted V_{out} was 10.8 mV; when the IM coil was introduced, however, V_{out} increased by a factor of 2 to 5 for different IM coil radii and location.

It can be seen that for IM coils of different sizes, the closer IM coil to RX coil, the larger the V_{out}. This is the result of strong coupling between the IM and RX coils when they are very close. Instead of "seeing" the tiny RX coil, the TX coil will "see" the new IM coil, which obviously generates larger V_{out}.

It can also be observed that for different IM coil location (Z_{RM}), there was an optimized IM coil radius to maximize V_{out}. Closer IM coil to RX coil (i.e., smaller Z_{RM}), smaller IM coil's radius R_{IM} for optimized V_{out}. For example, for Z_{RM} < 25 mm, optimized IM coil has R_{RX} = 15 mm; for Z_{RT} > 25 mm, optimized IM coil has R_{RX} = 30 mm. This can be explained noting that V_{out} is maximized when magnetic fluxes received by TX and IM from RX are equal. Fig. 5.6 shows the contour of IM coil for keeping a constant flux reception located between TX and RX coils. The equations for equal magnetic fluxes are:

$$\phi_{RT} = \frac{\mu_0 I {R_{RX}}^2 N_{RX} \pi {R_{TX}}^2}{2\left({R_{TX}}^2 + {Z_{RT}}^2\right)^{3/2}} = \phi_{RM} = \frac{\mu_0 I {R_{RX}}^2 N_{RX} \pi {R_{IM}}^2}{2\left({R_{IM}}^2 + {Z_{RM}}^2\right)^{3/2}} \tag{5.3}$$

where I is the current flowing through RX coil (detailed derivations in Appendix A). It is noted that (5.3) can be simplified to

$$\frac{{R_{TX}}^2}{\left({R_{TX}}^2 + {Z_{RT}}^2\right)^{3/2}} = \frac{{R_{IM}}^2}{\left({R_{IM}}^2 + {Z_{RM}}^2\right)^{3/2}} \tag{5.4}$$

Therefore, to keep the fluxes equal, larger Z_{RM} requires larger R_{IM}, which matches the experimental results.

For Z_{RM} = 10 mm and R_{IM} = 15 mm, the power transfer efficiency is now 3.0×10^{-5} (based on V_{out} of 55 mV and input voltage of 10 V), which is 25 times the efficiency for two coil RF link.

Based on the above results, we propose a structure of RF power link for the brain interfacing system, with the intermediate coil as power booster, as shown in Fig. 5.8 [12]. The IM coil should be as close to the RX coil as possible (close to the scalp as shown in Fig. 5.8), and the IM coil radius should be chosen in such a way to meet the constant magnetic fluxes criterion as illustrate above.

The above design and analysis is for the power link, in which the TX coil (in the external system) is much larger than the RX coil (implanted inside the brain). For the data link, the situation will be other way around: the TX coil is much smaller compared to the RX coil. However, the above design and calculations still hold, for the reason that the mutual inductance between TX and RX coils is always the same, i.e., $M_{TR} = M_{RT}$. Based on the derivations in Appendix A, the output voltage will also be the same. This ensures that the approach of applying mediating resonant coil for telemetry efficiency boosting works for the data link as well.

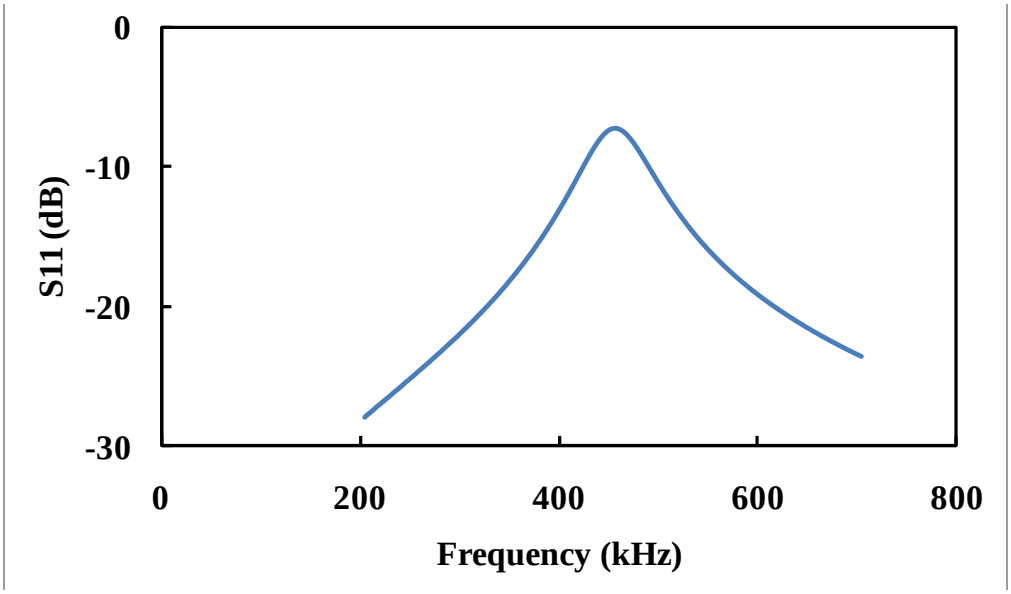

Fig. 5.1. S11 of parallel LC circuits with a 1.2 μH coil (radius of 44.5 mm) and 100 nF capacitor. Resonance frequency is 455 kHz, with Q of 7.

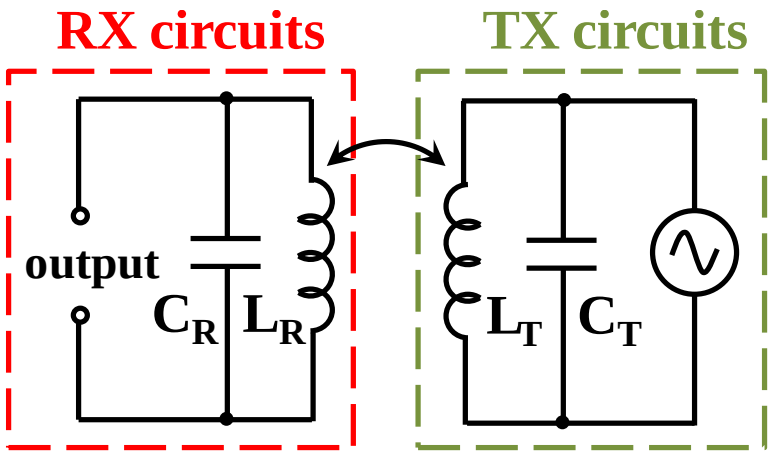

Fig. 5.2. Circuit diagram of transmitting (TX) and receiving coils (RX).

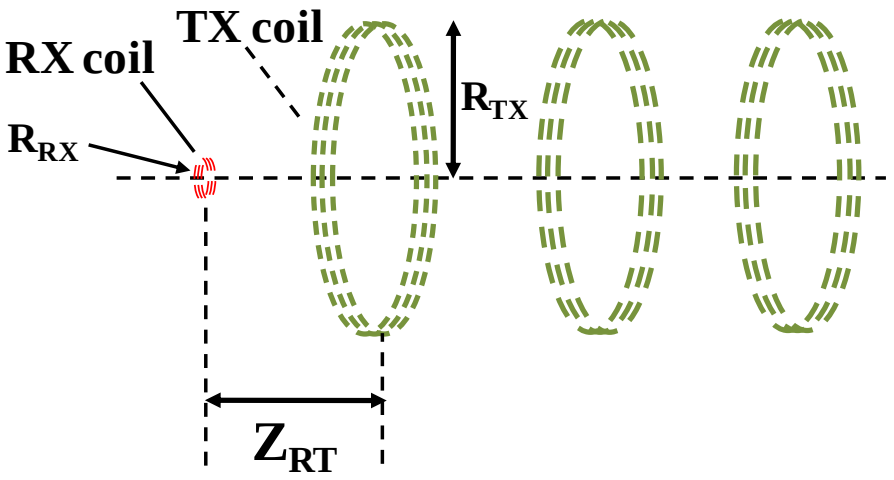

Fig. 5.3. RF link testing for two coils.

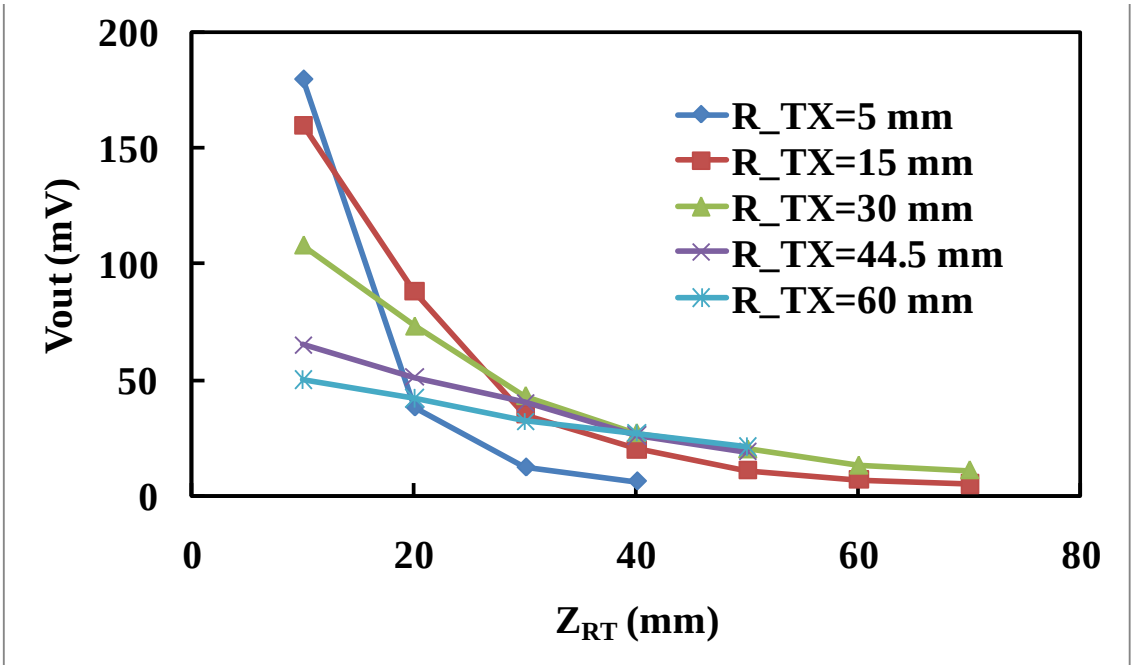

Fig. 5.4. Output peak-to-peak voltage versus TX coil location (Z_{RT}) for two coils RF transmission with different transmitting coil radii R_{TX}. R_{RX} was fixed at 0.6 mm.

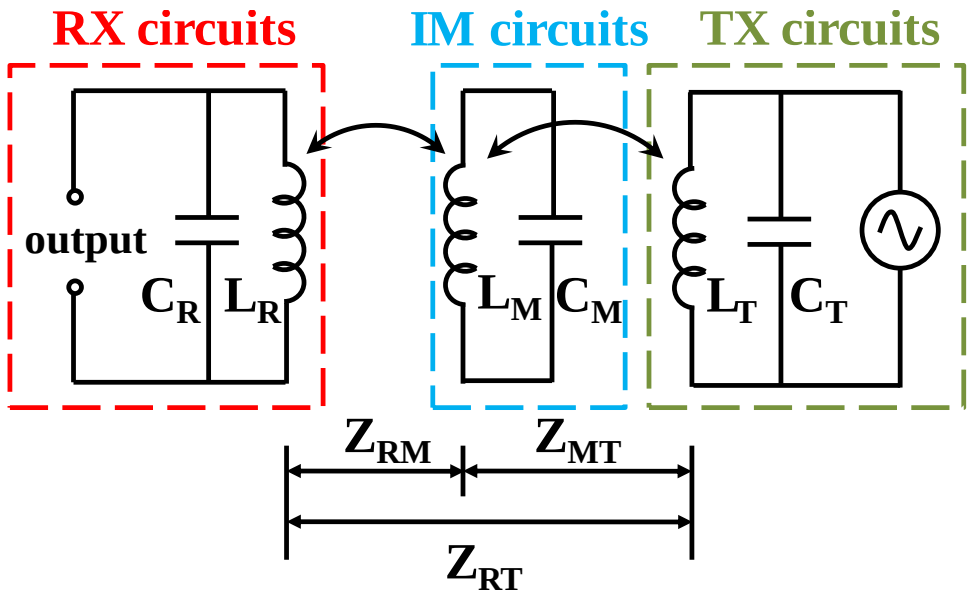

Fig. 5.5. Circuit diagram of transmitting (TX), receiving (RX) and intermediate coils (IM).

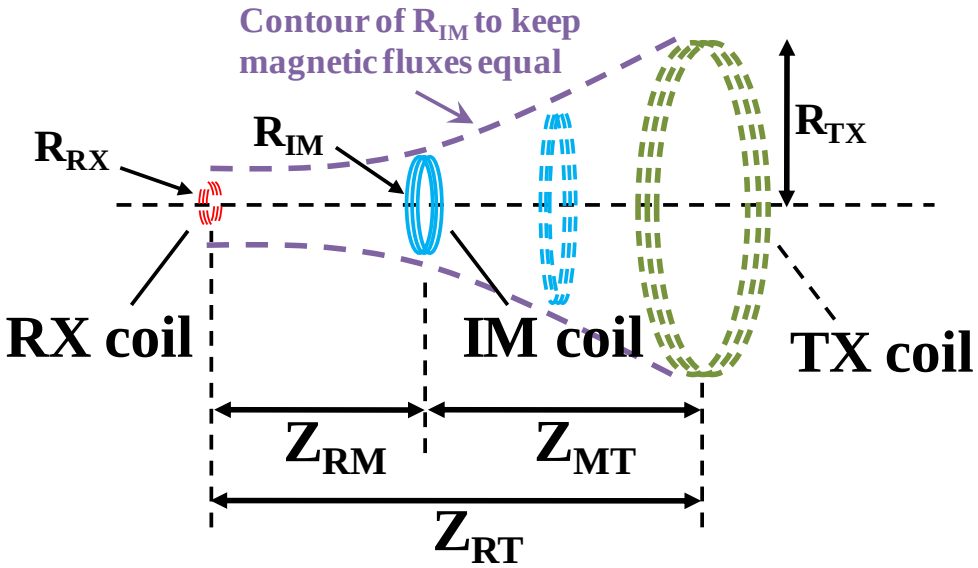

Fig. 5.6. RF link testing with three coils, including the intermediate coil.

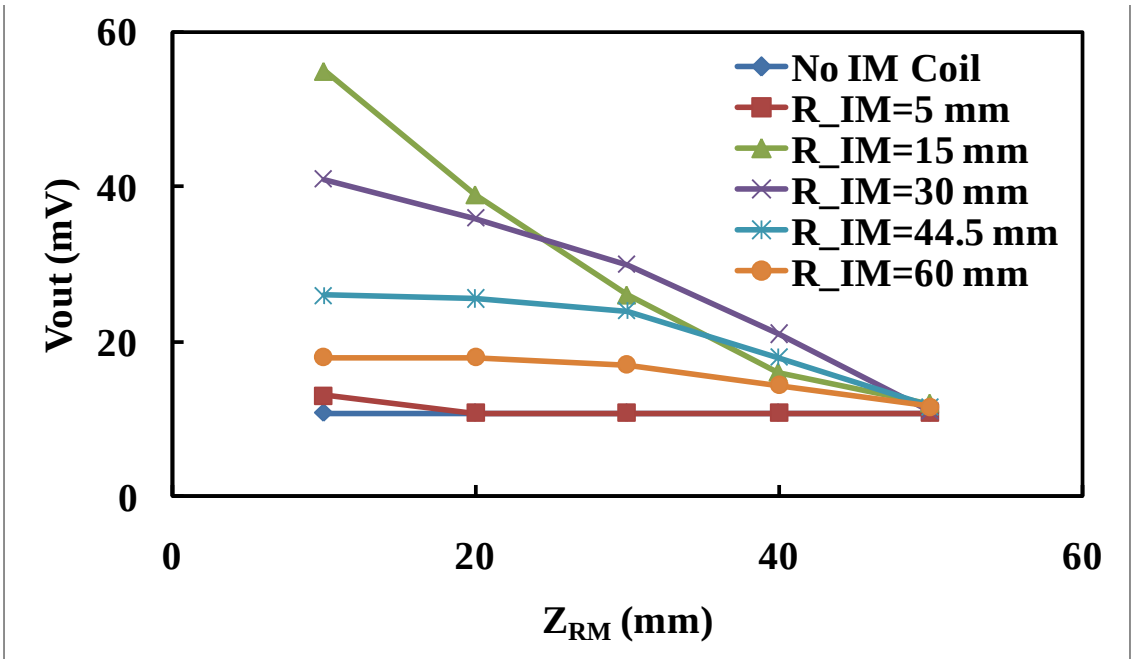

Fig. 5.7. Output peak-to-peak voltage versus intermediate coil location (Z_{RM}) for three coils transmission with different intermediate coil radii R_{IM}. $Z_{RT} = Z_{RM} + Z_{MT}$, fixed at 70 mm. R_{RX} and R_{TX} were fixed at 0.6 mm and 44.5 mm, respectively.

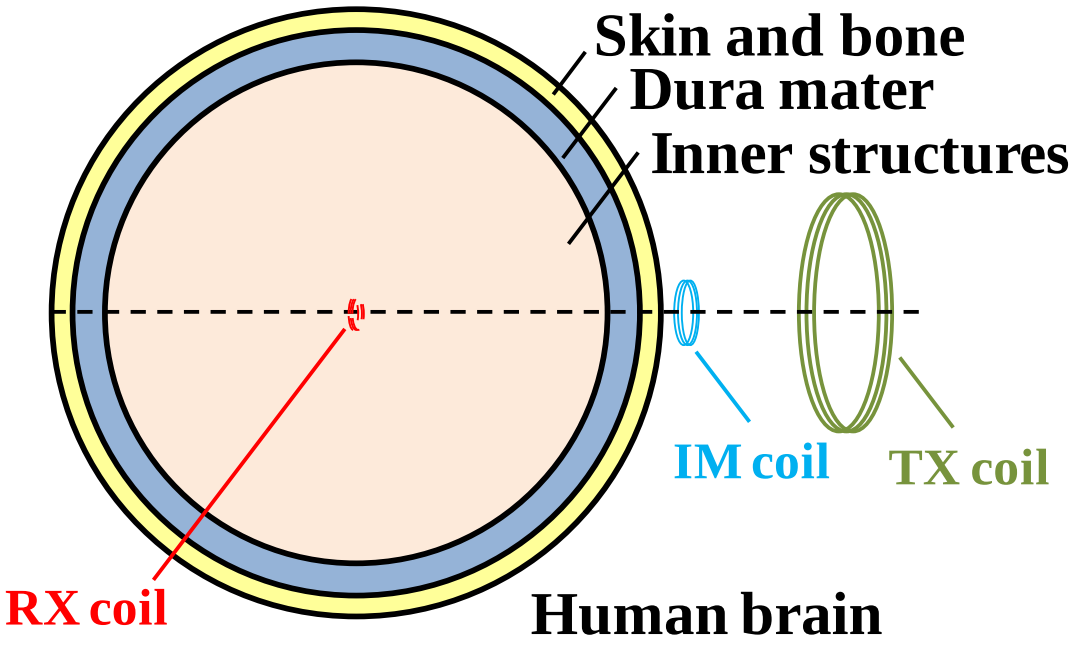

Fig. 5.8. Schematic of coils transmitting and receiving inside/outside human brain with intermediate coil as power booster.

5.4 References

[1] B. Lenaerts and R. Puers, *Omnidirectional Inductive Powering for Biomedical Implants*, Springer, 2009.

[2] A.P. Sample, D.A. Meyer and J.R. Smith, "Analysis, experimental results, and range adaptation of magnetically coupled resonators for wireless power transfer," *IEEE Transactions on Industrial Electronics*, Vol. 58, No. 2, pp. 544-554, 2011.

[3] A. Kurs, A. Karalis, R. Moffatt, J.D. Joannopoulos, P. Fisher and M. Soljacic, "Wireless power transfer via strongly coupled magnetic resonances," *Science*, Vol. 317, No. 5834, pp. 83-86, 2007.

[4] Y. Tak, J. Park and S. Nam, "Mode-based analysis of resonant characteristics for near-field coupled small antennas," *IEEE Antennas and Wireless Propagation Letters*, Vol. 8, pp. 1238-1241, 2009.

[5] K. Fotopoulou and B.W. Flynn, "Wireless powering of implanted sensors using RF inductive coupling," *Proceedings of IEEE Sensors*, Daegu, South Korea, pp. 765-768, 2006.

[6] M. Ghorbel, A.B. Hamida and J. Tomas, "CMOS RF powering system for cochlear implant," *3rd International Conference on Signals, Circuits and Systems, SCS 2009*, Medenine, Tunisia, pp. 1-4, 2009.

[7] W.J. Heetderks, "RF powering of millimeter- and submillimeter-sized neural prosthetic implants," *IEEE Transactions on Biomedical Engineering*, Vol. 35, No. 5, pp. 323-327, 1988.

[8] W. Wang, H. Hao, B. Ma, F. Liu, C. Hu and L. Li, "Design and analysis of a transcutaneous telemetry device for brain stimulator," *Proceedings of the Annual International Conference of the IEEE Engineering in Medicine and Biology Society*, Minneapolis, MN, USA, pp. 2153-2156, 2009.

[9] D. J. Young, "Wireless powering and data telemetry for biomedical implants," *Proceedings of the Annual International Conference of the IEEE Engineering in Medicine and Biology Society*, Minneapolis, MN, USA, pp. 3221-3224, 2009.

[10] A.K. RamRakhyani and G. Lazzi, "On the design of efficient multi-coil telemetry system for biomedical implants," *IEEE Transaction on Biomedical Circuits and Systems*, Vol. 7, No. 1, pp. 11-13, 2013.

[11] A.K. RamRakhyani, S. Mirabbasi and C. Mu, "Design and optimization of resonance-based efficient wireless power delivery systems for biomedical implants," *IEEE Transactions on Biomedical Circuits and Systems*, Vol. 5, No. 1, pp. 48-63, 2011.

[12] L. Chen and M. Tabib-Azar, "Optimization of wireless power transfer with intermediate resonant coil for interfacing with the central nervous system," presented at Progress In Electromagnetics Research Symposium (PIERS), Moscow, Russia, 2012.

[13] H.A. Haus and W. Huang, "Coupled-mode theory," *Proceedings of the IEEE*, Vol. 79, No. 10, pp. 1505-1518, 1991.

[14] R.E. Hamam, A. Karalis, J. D. Joannopoulos and M. Soljacic, "Efficient weakly-radiative wireless energy transfer: an EIT-like approach," *Annals of Physics*, Vol. 324, No. 8, pp. 1783-1795, 2009.

[15] A. Kurs, R. Moffatt and M. Soljacic, "Simultaneous mid-range power transfer to multiple devices," *Applied Physics Letters*, Vol. 96, No. 4, pp. 044102, 2010.

[16] J. Kim, H. Son, K. Kim and Y. Park, "Efficiency analysis of magnetic resonance wireless power transfer with intermediate resonant coil," *IEEE Antennas and Wireless Propagation Letters*, Vol. 10, pp. 389-392, 2011.

CHAPTER 6

THE COMPLETE WIRELESS SYSTEM

A completely wireless neural interfacing system is presented in this chapter. The first section discusses a wirelessly powered system based on tunnel diode oscillation circuit, which proves the concepts of neural signal amplification, wireless powering, inductive coupling, analog demodulation and computer data acquisition. The second section presents the results of neural interfacing system based on MEMS oscillator, which demonstrates the feasibility of neural signal modulated FM signal generation and signal restoration with digital signal processing techniques.

6.1 Wirelessly Powered Neural Interfacing System Based on Tunnel Diode Oscillator

A wireless neural interfacing system with tunnel diode oscillator was built. An artificial neuron signal was generated with benchtop instruments, treated with a wirelessly powered internal system, wirelessly transmitted to the external system, restored and displayed in the computer interface (Fig. 6.1). Neural signal undershoot is not considered in the development of this system.

An artificial neuron signal was generated with a function generator (Agilent 33250A). The minimum amplitude of pulse that can be generated is 1 mV, while typical extracellular neuron signal is 500 μV [1]. Therefore, a voltage division with ratio of 0.5 was applied after the output of the function generator. The generated pulse had 500 μV amplitude, 500 μs duration, 1 μs rise/fall time, and 10 ms period, which resembles a typical extracellular neuron signal characteristic (Fig. 6.2). This artificial neuron signal was then fed into a neuron amplifier circuit.

The neuron amplifier chip was wirelessly powered with an RF link along with a full-wave rectifier, as shown in Fig. 6.3. The RF link was made of two identical coils, with separation distance of 5 mm. Each coil has a diameter of 14 cm, 20 turns, inductance of 167 μH and series resistance of 5 Ω (measured by HP 4284A Precision LCR Meter at 10 kHz, 1 V bias, Ls - Rs mode). The transmitting coil was powered by a signal generator (HP 33120A) with 180 kHz, 10 Vpp sinusoidal wave (50 Ω output), while the receiving coil was fed to the full-wave rectifier to convert AC to DC. Germanium diode 2N1517 was used as the rectifying diode for its very low turn on voltage of 267 mV. A capacitor of 47 μF was used to low pass the rectified signal, providing clean DC output to the neuron signal amplifier. The DC output was measured to be 3 V, which is enough for powering the neuron signal amplifier.

The efficiency of the RF powering link can be calculated with the measured output DC voltage. The impedance of the transmitting coil at 180 kHz was ωL = 189 Ω, which implies the peak voltage across the transmitting coil from the signal source was VpTX = 10 Vpp × 2 × 189 Ω / (189 Ω + 50 Ω) × 0.5 = 7.9 V. The peak voltage across the receiving coil, on the other hand, can be calculated based on turn-on voltage of

germanium diode and the efficiency of the full-wave rectifier: V_{pRX} = 3 V / (2 / π) + 0.267 V = 5.0 V. Therefore, the efficiency of the RF powering link is V_{pRX} / V_{pTX} = 63%, which is reasonable considering the separation distance and the air-core nature of this RF link.

Low-power op-amp of LT6202 from Linear Technology was chosen as the neuron signal amplifier with ultra low noise voltage of 1.9 $nV/\sqrt{Hz}$. The op-amp was powered up by the air-core transformer as described above with 3 V. Fig. 6.4 shows the neuron signal amplification circuit. Resistors RD1 = RD2 = 1 kΩ for voltage division for 500 μV neuron signal generation. Gain of 1,000 was achieved using negative amplification circuit with R1 = 100 Ω and R2 = 100 kΩ. A 0.5 μF capacitor was used at the output to filter out interference from the wireless power source. The amplified neuron signal, which is shown in Fig. 6.5, was then passed to the action potential to RF module.

The action-potential-to-RF module used is based on tunnel diode as shown in Fig. 6.6, with coil inductor of 2.3 μH and series resistance of 0.35 Ω (measured by HP 4284A Precision LCR Meter at 10 kHz, 1 V bias, Ls - Rs mode). Tunnel diode 1N3717 was used as the active component, which is the same tunnel diode used in Chapter 4, with its measured I-V parameters shown in Table 4.1. Input to the action potential to RF module was the amplified neuron firing signal. No shunt capacitor was connected to the tunnel diode, meaning that the oscillation frequency would be determined by the tunnel diode's intrinsic junction capacitance along with the coil inductor. The output from the coil inductor is neuron signal modulated RF oscillations, which is suitable for wireless transmission, as shown in Fig. 6.7a. Zoomed-in waveform is shown in Fig. 6.7b, indicating oscillation frequency of 23.734 MHz. Using equation of $f_{osci} = \frac{1}{2\pi\sqrt{LC}}$ along

with oscillation frequency and coil inductance, the tunnel diode's junction capacitance was found to be 19.6 pF, which is very close to the manufacturer specification of 25 pF as shown in Table 6.1.

The neuron signal modulated RF signal was transmitted and received by the external system, with schematics shown in Fig. 6.8. A coil of 2.3 μH inductance (same as the coil in the action potential to RF module of the internal system) was placed 1 cm away. The received RF signal is shown in Fig. 6.9. The envelope of this RF signal needs to be detected in order to restore the original neuron firing signal. To do this, the signal was first amplified with an RF amplifier (Mini-Circuits ZFL-500, 0.05 - 500 MHz), and then passed through a demodulator, i.e., envelope detector. The demodulator is composed of a germanium diode (2N1517, turn on voltage of 267 mV), and then the input capacitance of a low-noise amplifier (Stanford Research System 560 Low-noise Preamplifier), which is 25 pF. Besides acting as a capacitor, the amplifier was also used as a filter, with frequency range of 10 - 1 MHz, to preserve harmonics brought with the square wave shape of the neuron signal. The output of the preamplifier, which is also the recovered neuron firing signal, is shown in Fig. 6.10.

The output of the SR560 amplifier was then connected to the data acquisition board of USB-1208LS (Measurement Computing). The rate was set to 8000 per second (maximum), which is enough to illustrate the recovered neuron signal. Fig. 6.11 shows a LabVIEW 2009 interface with three pulses of the restored neuron firing signals.

Power consumption of the internal system is equivalent to that of the neuron signal amplifier. The amplifier of LT6202 operated with 2.3 mA current under 3 V supply, meaning that the chip's power consumption was $P_{amp} = 3\ V \times 2.3\ mA = 6.9\ mW$, which

is also the power consumption of the internal system. However, the RF powering link and rectifier are not ideal; therefore, the power from the signal source in the external system is higher. The signal source provided 20 Vpp to the load of 50 Ω and 189 Ω (impedance of the transmitting coil as calculated before) in series, consuming power of $P_{external}$ = (20 V / $2\sqrt{2}$)^2 / (50 Ω + 189 Ω) = 209 mW. This implies a power efficiency of P_{amp} / $P_{external}$ = 3.3%, which is very low; however, the external system can be assumed to have unlimited power supply and therefore this is not an issue.

6.2 Neural Interfacing System Based on MEMS Oscillator

In this section, results of a neural interfacing system based on MEMS positive feedback oscillator are presented, illustrating complete neural signal modulation and demodulation.

As demonstrated in section 4.4, DC biasing of the MEMS oscillator can be modulated with processed neural signal to create FM signal output which bears the neural signal information. Sensed neuron pulse signals can be amplified and biased easily within the internal system (Fig. 6.12a). The pulse duration, however, should be kept around the 1 ms range [1].

To demonstrate the concept of neural signal modulation with the benchtop instruments based MEMS oscillator, the pulse duration was scaled. The input processed artificial neural signal is shown in Fig. 6.12b, which was programmed directly into the Keithley 237 Source Measure Unit (DC biasing of the MEMS oscillator). The programmed waveform consists of 50 points, each point having a delay of 70 ms. The pulse duration is 3.5 s for one neural spike. The biasing voltage is 34 V, while V_{peak} and

$V_{undershoot}$ are 15 V and 2.8 V, respectively. The complete neuron interfacing system with MEMS oscillator, in which the two RF coils have the same inductance of 22 μH, with separation of 2 cm, is shown in Fig. 6.13.

The artificial neural signal shown in Fig. 6.12b was applied to the DC biasing of the oscillator circuit, and the received signal from the RF coil inductive coupling link is shown in Fig. 6.14. The waveform has almost constant envelope, and the frequency is modulated by the DC biasing neural signal. The received signal has a peak voltage of 10 mV, while the transmitted signal (after the buffer) has a peak voltage of 100 mV. Therefore, the voltage transfer efficiency is 10%, while the power transfer efficiency is 1%. The received waveform was then processed with Matlab to obtain the frequency information by fast fourier transform (FFT). The time domain sample rate is 2 MHz, which is about 4 times the oscillation frequency (~ 440 kHz), satisfying Nyquist sampling theorem. The FFT window size is set to 50,000. The resulting frequency versus time waveform is shown in Fig. 6.15a. Using the mapping between frequency and DC voltage in Fig. 4.19, the neural signal waveform is restored after subtracting biasing voltage (Fig. 6.15b). It can be seen that the restored neural signal matches the input signal well, for the most part. The duration of the restored signal is shorter than the input signal by 9%, as a result of the response time limitation of the MEMS oscillator, which will be discussed in the following section. The rms error between the input and restored neural signal is found to be 0.66 V for one neural pulse. With peak neural voltage of 15 V, the normalized error is 0.66 V / 15 V = 4.4%.

The original neural signal was biased 34 V before being connected to the MEMS bridge as the modulation signal, because the MEMS resonator needs a minimum turn-on

voltage for proper feedback operation. However, 34 V is pretty high for operation inside a living organism, for example, the brain. So it is necessary to minimize the bias voltage, to both reduce internal system power consumption and make the system more feasible for bio-implantation applications, which will be discussed in the Further Work chapter.

The time duration of the input artificial neural pulse is 3.5 s, which is scaled from the usual 1 ms duration of an actual neural signal. It was found to be very hard to further reduce the total pulse duration while maintaining the correct FM oscillation output. This is the result of the long response time of the MEMS positive feedback oscillation circuit set-up, due to 1) benchtop instrument amplifier and connecting cables introducing delays in each loop cycle; 2) small device current (lateral resonator), leading to long charging time. The first limitation can be easily overcome by integrating CMOS sustaining amplifier with the MEMS resonator on the same substrate, thereby reducing the loop delay time greatly. This integration can be achieved with common CMOS analog circuit design techniques and will not be discussed in this dissertation. The second limitation, however, can be solved by new MEMS device design, which will be discussed in detail in the Further Work chapter, along with the turn-on voltage reduction discussion.

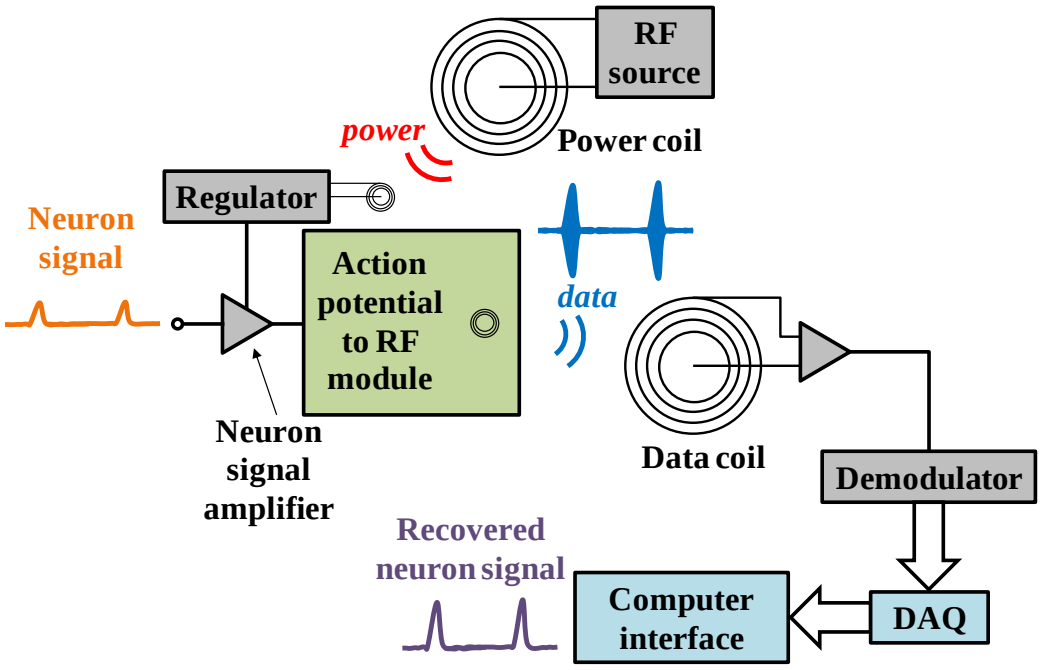

Fig. 6.1. Schematic of the wireless neural interfacing system with tunnel diode oscillator.

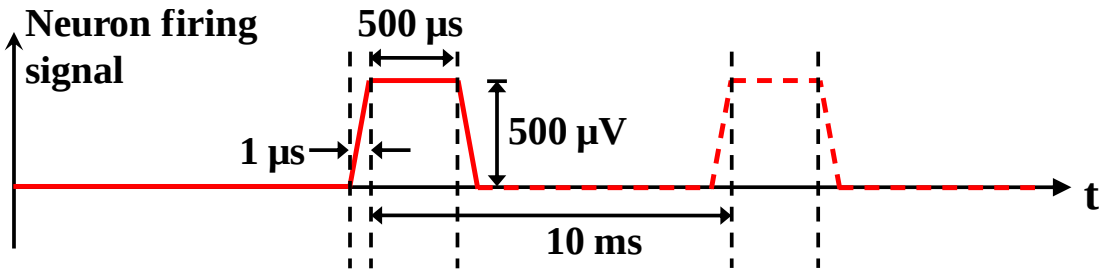

Fig. 6.2. Artificial neuron firing signal (ignoring overshoot).

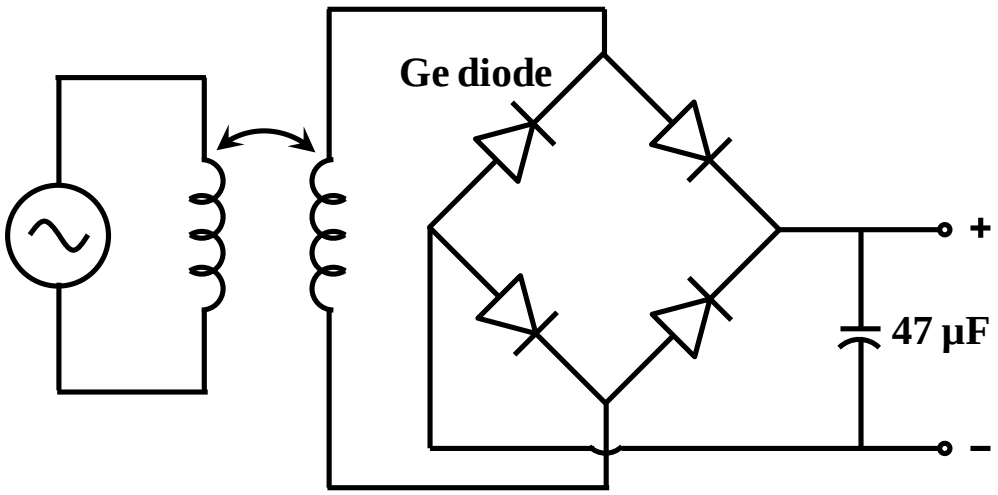

Fig. 6.3. Full-wave rectifier circuit for powering neuron signal amplifier.

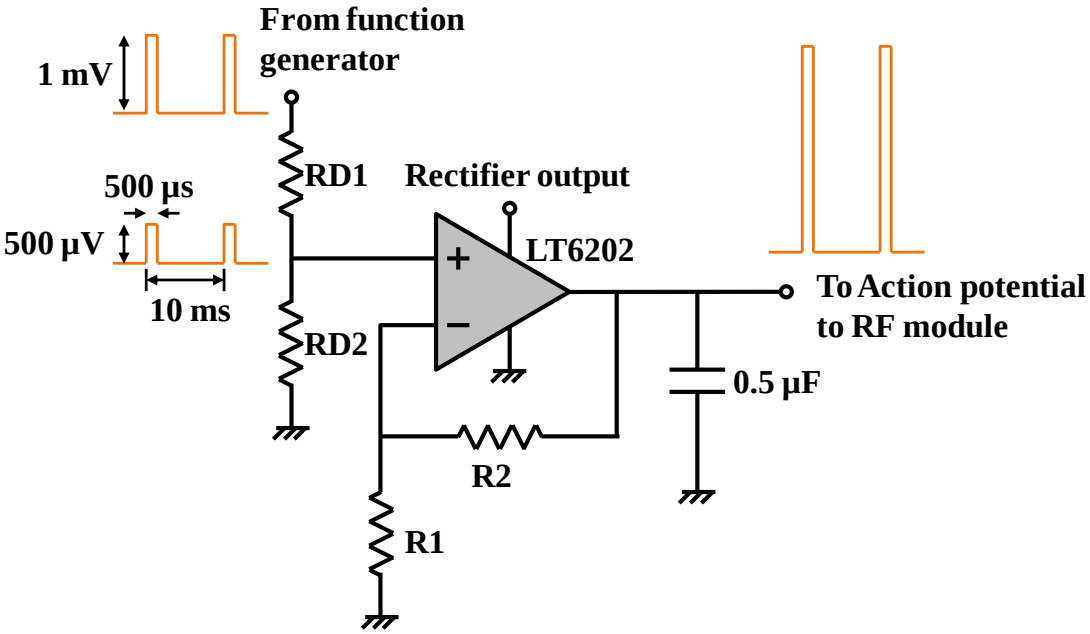

Fig. 6.4. Circuit schematics of neuron signal generation and amplification. RD1 = RD2 = 1 kΩ for voltage division. R1 = 100 Ω, R2 = 100 kΩ, which achieves gain of 1,000.

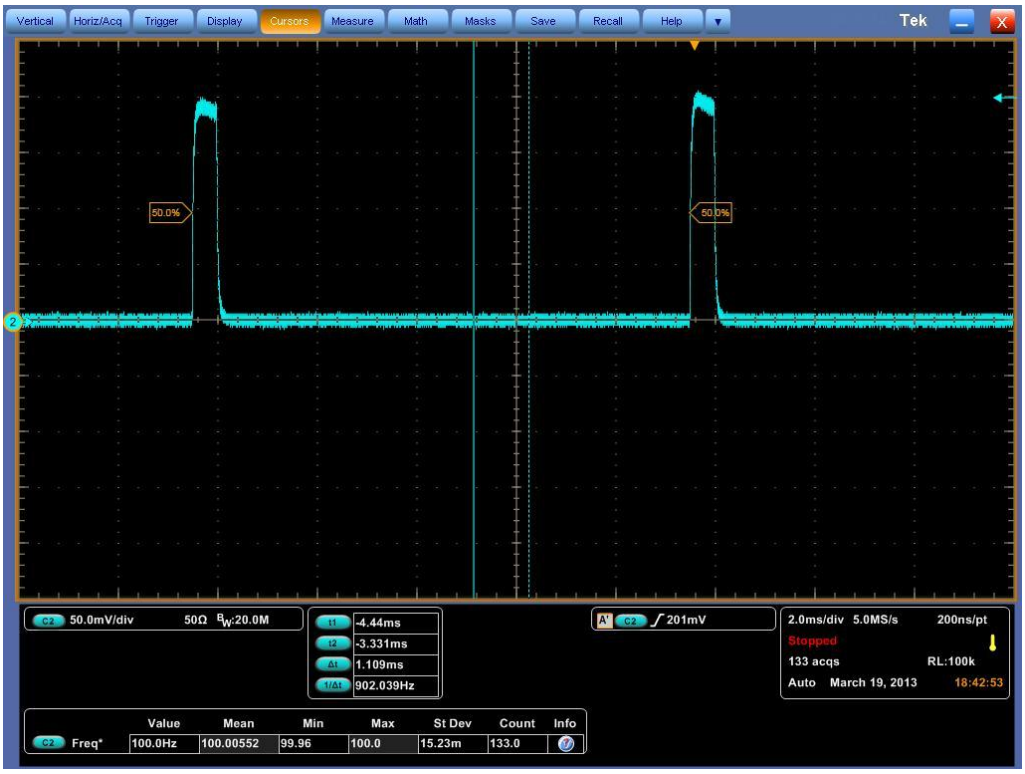

Fig. 6.5. Amplified neuron signal, which acts as input to action potential to RF module.

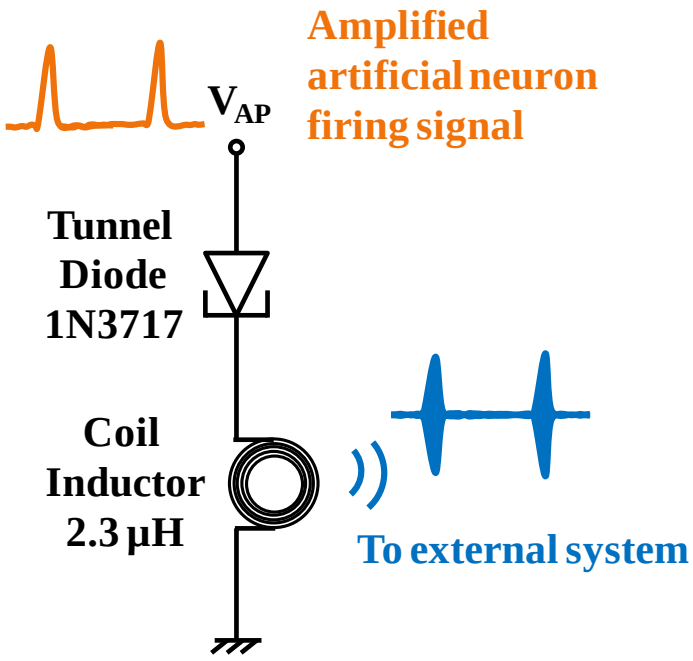

Fig. 6.6. Action potential to RF module based on tunnel diode.

(a)

(b)

Fig. 6.7. Modulated RF signal output. a) Neuron signal modulated RF signal across the coil inductor, generated by action potential to RF module. b) Zoomed-in RF waveform showing oscillation frequency of 23.734 MHz.

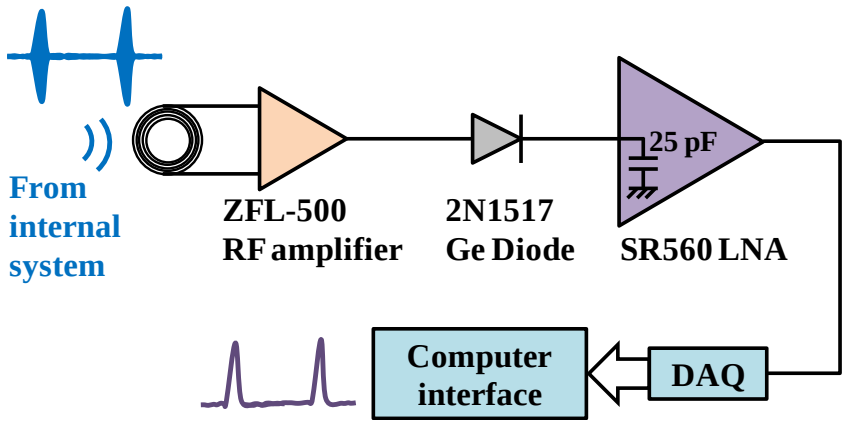

Fig. 6.8. Analog receiving circuitry of the external system, recovering detected neuron signal.

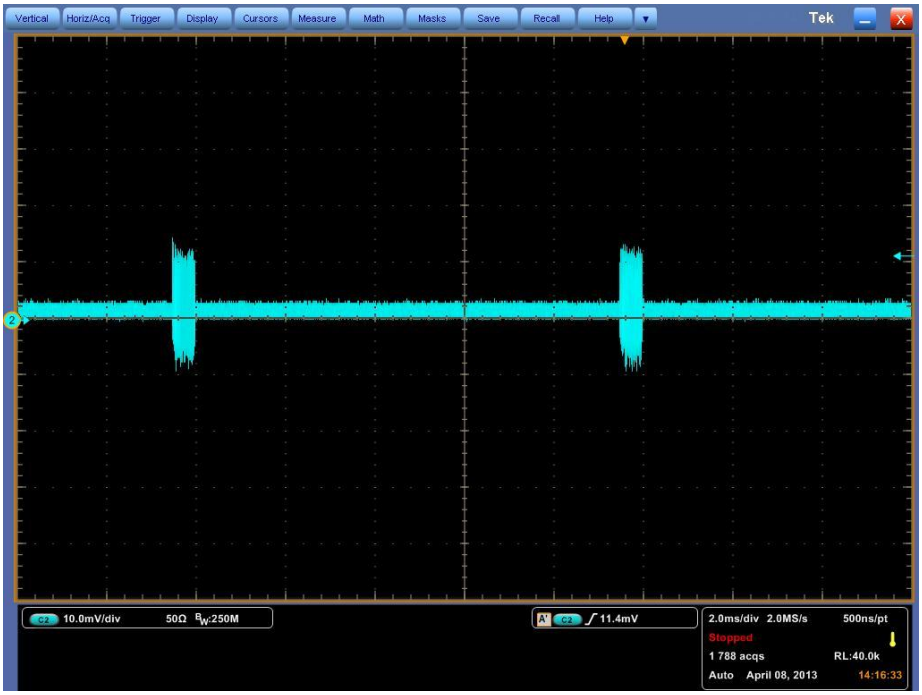

Fig. 6.9. Neuron signal modulated RF signal detected by the coil inductor of the external system, separated with the internal system's coil inductor by 1 cm.

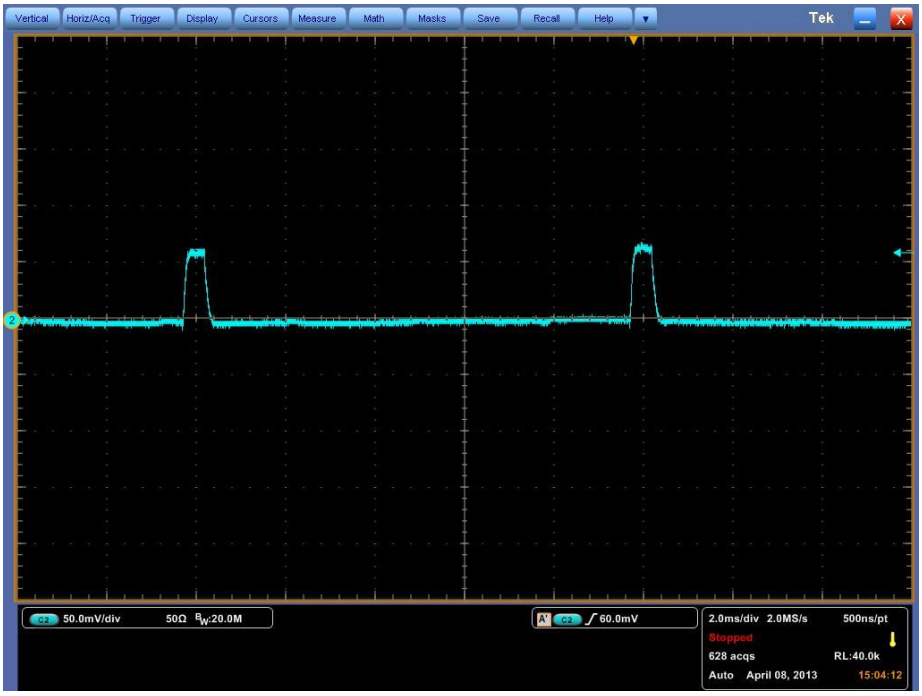

Fig. 6.10. Recovered neuron signal after SR560 low noise amplifier.

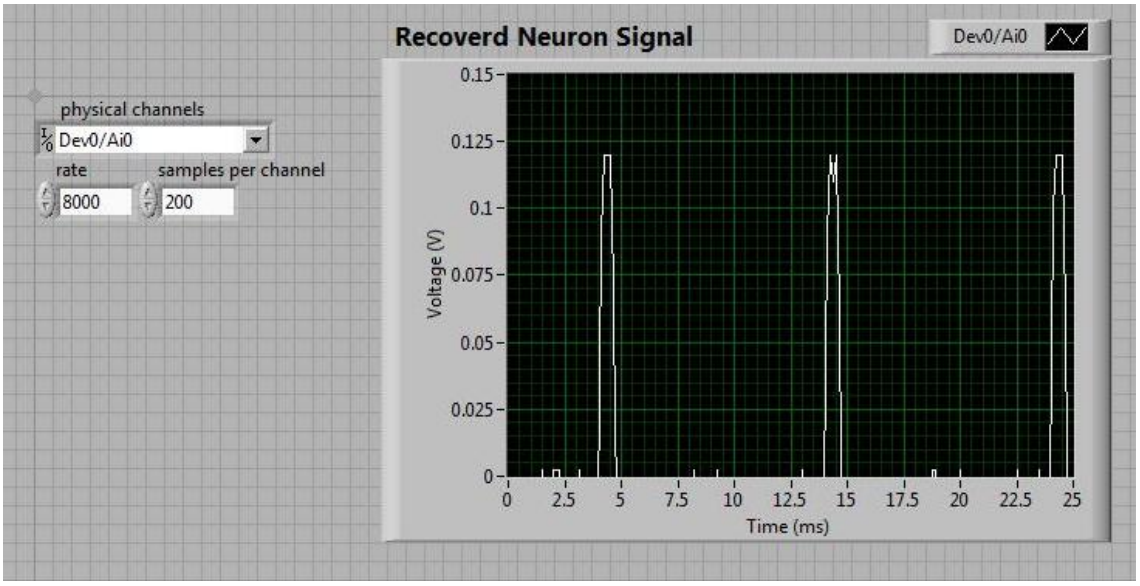

Fig. 6.11. Recovered neuron signal waveform shown in LabVIEW 2009 interface with data acquisition board of USB-1208LS.

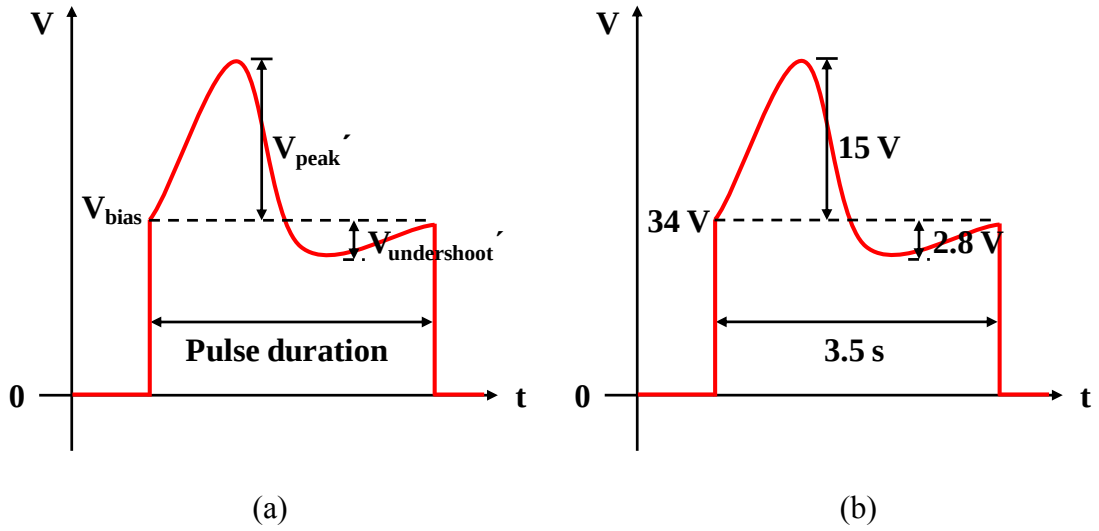

Fig. 6.12. Parameters of neural signal waveform. a) Processed neural signal waveforms. b) Processed artificial neural signal acting as DC biasing of the MEMS oscillator, with V_{peak}' = 15 V, $V_{undershoot}$' = 2.8 V, V_{bias} = 34 V and pulse duration = 3.5 s.

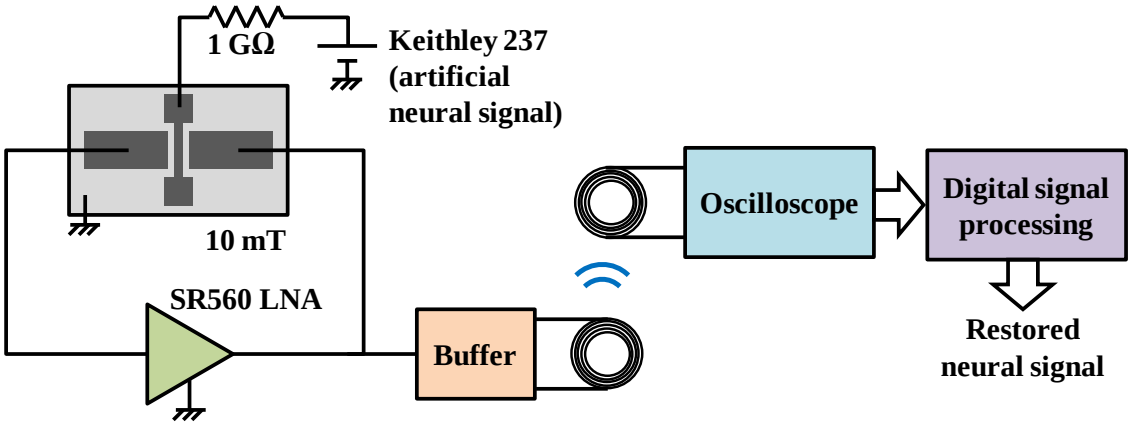

Fig. 6.13. Neuron interfacing system based on MEMS oscillator with wireless data transmission and neural signal restoration.

Fig. 6.14. Received oscillation waveforms with frequency modulated by artificial neural signal, to be processed with DSP techniques to restore the neural signal.

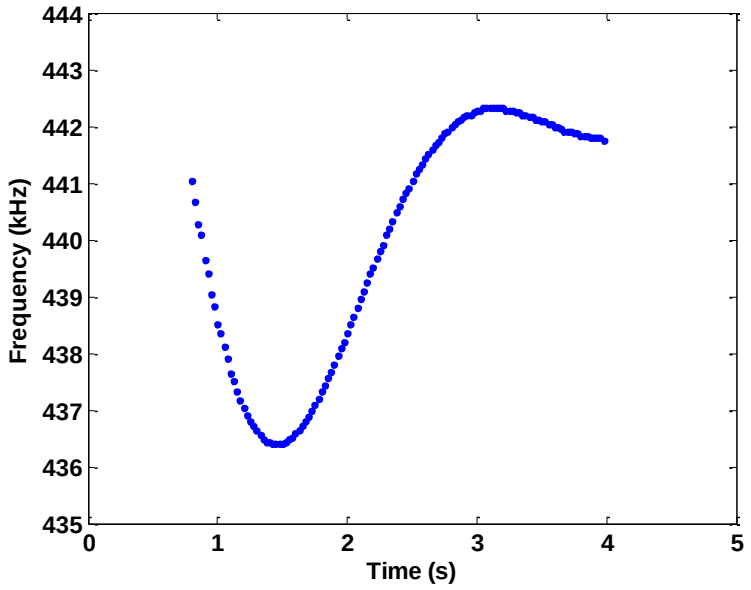

(a)

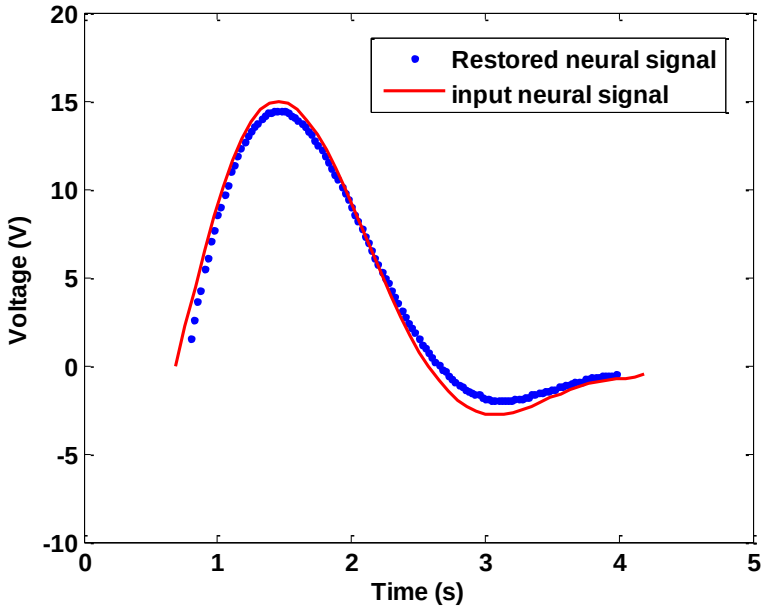

(b)

Fig. 6.15. Decoded neural signal information. a) Calculated frequency values of the time domain signal in Fig. 6.14. b) Restored neural signal voltages mapped from the frequencies, along with artificial neural signal input (bias voltage subtracted).

6.3 References

[1] R.R. Harrison, P.T. Watkins, R.J. Kier, R.O. Lovejoy, D.J. Black, B. Greger and F. Solzbacher, "A low-power integrated circuit for a wireless 100-electrode neural recording system," *IEEE Journal of Solid-State Circuits*, Vol. 42, No. 1, pp. 123-133, 2007.

CHAPTER 7

CONCLUSIONS

This thesis realizes a complete wireless microsystem for brain interfacing, based on a microelectromechanical system. Components of the neuron sensing system include TiW fixed-fixed bridge resonator, MEMS oscillator based action-potential-to-RF module, and high-efficiency RF coil link for power and data transmissions.

TiW fixed-fixed bridge resonator on glass substrate was fabricated and characterized as a signal filter inside the system. The resonator possesses resonance frequency of 100 - 500 kHz, with a quality factor up to 2,000 inside vacuum conditions. The effect of surface conditions on its quality factor was studied with 10s nm Al_2O_3 layer deposition with ALD. It was found that the resonator's quality factor decreased with increasing surface roughness, which was the result of thicker Al_2O_3 coating.

Action-potential-to-RF module was realized with two approaches. The first approach was based on MEMS oscillator with TiW bridge. Oscillation signal with frequency of 442 kHz and phase noise of -84.75 dBc/Hz at 1 kHz offset was obtained. The DC biasing of the MEMS device is around 34 V to have stable oscillation. To further reduce the actuation voltage, better MEMS structure needs to be realized, which will be discussed in the next chapter. The second approach took advantage of a tunnel diode oscillation circuit which produced neural action-potential-modulated-RF output with a quality factor of

800,000 and power consumption as low as 0.21 mW. The MEMS oscillator approach is preferable due to its high quality factor, small device footprint, easier IC-compatible fabrication processes, and larger tuning range.

Besides the above two approaches, a novel concept of MEMS relaxation oscillator was also proposed. Feasibility of the relaxation oscillator was demonstrated with a macrosize piezoelectric device based system. Dynamic analysis of the MEMS DC-to-RF conversion system was presented, giving the criterion for sustainable self-oscillation. With only a constant current source, the system can generate oscillation of 10s Hz. The performance can be greatly improved once the contact stiction problem is solved by a smaller size of air-gap and lower actuation voltage.

High-efficiency RF coil link for power and data communications were designed and realized. Based on the coupled mode theory (CMT), introducing the intermediate resonance coil has increased the voltage transfer efficiency by 5 times.

Finally, complete neural interfacing systems were demonstrated with board-level integration, one with MEMS oscillator, the other with tunnel diode circuitry. The systems consist of both internal and external systems, wireless powering, wireless data transfer, artificial neuron signal generation, neural signal frequency modulation and demodulation, and computer interface displaying restored neuron signal.

CHAPTER 8

FURTHER WORK

Further works include 1) design and analysis of next-generation MEMS device for action-potential-to-RF module; 2) realization of MEMS amplifier based on gate control of tunneling current with MEMS TiW cantilever; 3) considerations for in vivo brain interfacing system implementation.

8.1 Next-Generation MEMS Device for Action-Potential-to-RF Module

As discussed in section 6.2, it is imperative to reduce both the turn-on voltage and feedback response time of the MEMS oscillator. Both these requirements can be met by decreasing the motional resistance of the MEMS resonator, to that end, increasing the MEMS device capacitance.

For feedback operation to work, the gain of the sustaining amplifier should be larger than the sum of the loop loss, including resonator motional resistance, resistance of the amplifier and other sources of loss. For a fixed amplifier gain, smaller loss means larger net gain through one loop cycle, fewer loop cycles to achieve saturation and stable oscillation, and therefore, faster oscillation response time. Hence, decreasing the motional

resistance, which is the dominant part of loop loss, enables faster feedback oscillator response.

The definition of motional resistance for the MEMS resonator is

$$R_{motion} = \frac{V_{ACdrive}}{|i_o|} \tag{8.1}$$

in which $V_{ACdrive}$ is the AC driving voltage, and i_o is the output sensing current. $V_{ACdrive}$ depends on the external input, which is the noise level of the sustaining amplifier in the case of the MEMS feedback oscillator. Output sensing current, i_o, on the other hand, is device dependent, using the lateral bridge in Fig. 8.1 as an example:

$$i_o(t) = \frac{\partial Q_{sense}}{\partial t} = V_{DC}\frac{\partial C_{sense}}{\partial t} = V_{DC}\varepsilon_0\omega_0\frac{A}{g^2}X_m sin\omega_0 t \tag{8.2}$$

in which V_{DC}, ω_0, A, g and X_m are the DC bias, device resonance frequency, sensing area, instantaneous gap size and bridge displacement.

The bridge displacement X_m can be calculated as

$$X_m = \frac{F}{k}Q \tag{8.3}$$

in which F, k and Q are the electrostatic actuation force, bridge spring constant and resonator quality factor, respectively. The electrostatic force F can be expressed as

$$F = \frac{1}{2}\varepsilon_0\frac{A}{g^2}V^2 \tag{8.4}$$

where V is the electrostatic actuation voltage. Combine (8.2) (8.3) (8.4), and it can be seen that

$$i_o(t) \propto \frac{A^2}{g^4} \tag{8.5}$$

assuming constant resonance frequency, spring constant and quality factor. We can see that large sensing area and small gap size can tremendously increase the sensing current, and therefore, decrease the motional resistance.

Based on the above analysis, in order to bring down the turn-on voltage and feedback response time of the MEMS oscillator, devices with larger sensing area and smaller gap size should be used. Larger sensing area can be achieved by making the device thicker for lateral resonator, or using proof mass structure for vertical resonator. Narrowing the gap size is process dependent, but is generally easier in a vertical resonator where sacrificial layer thickness can be better controlled.

For the next generation of MEMS device, the ratio of A / g^2 will be increased by 100 times, which leads to 10 times smaller turn-on voltage and 10,000 times smaller motional resistance. The feedback response time will then be in the μs range, and can be easily modulated with ms pulse duration neural signal.

8.2 Tunneling Current Based MEMS Amplifier

When DC voltage is applied across a very small gap (10s to 100s nm), tunneling current will conduct, instead of getting an open circuit. Tunneling current is very sensitive to the gap distance, which can be utilized to realize a high gain MEMS amplifier. In this section, a MEMS tunneling current (MTC) based amplifier has been proposed and studied.

Tunneling current can be characterized with the well-known Fowler-Nordheim equation [1-2]:

$$j_{field} = \frac{A_{FN}\beta^2 E^2}{\phi t^2(y)} exp\left[-\frac{B_{FN}\phi^{3/2}\upsilon(y)}{\beta E}\right] \tag{8.6}$$

where j_{field} is the current density, while the variables are electric field E, coefficient $\upsilon(y)$ and surface condition parameter β. For ideally flat gap surface, β is 1; for rough surface, β is 55 [1]. Both E and $\upsilon(y)$ are voltage and gap size dependent. The equation shows that

tunneling current goes up exponentially with smaller gap size and larger voltage. For the dimensions of the fabricated TiW bridge, which has 5 μm width and 1 μm thickness, corresponding tunneling current versus gap size at different voltages were plotted for different surface conditions (Fig. 8.2). It can be seen that a rougher surface (larger β) leads to larger tunneling current for the same voltage.

The tunneling current can be modulated by changing the gap size with gate voltage, with schematics shown in Fig. 8.3. The electrostatic force applied to the cantilever by the electrode is

$$F_e = \frac{1}{2}\varepsilon_0 {V_G}^2 \frac{A}{{g_0}^2} \tag{8.7}$$

where V_G is the gate voltage, A is the electrode area, and g_0 is the original gap size. Considering the cantilever's spring constant

$$k = E\frac{W^3 t}{4L^3} \tag{8.8}$$

where W, t and L are the width, thickness and length of the cantilever, respectively. Therefore, the tip displacement of the cantilever is

$$\Delta g = \frac{F_e}{k} \tag{8.9}$$

Assume that after gate voltage actuation, the new gap size is

$$g' = \sqrt{{g_0}^2 \pm \Delta g^2} \tag{8.10}$$

Therefore, DC gate control on tunneling current can be calculated by substituting g' into the Fowler-Nordheim equation. Equ. (8.10) shows that the gap size can be either increased or decreased with gate voltage depending on whether the MEMS bridge is actuated in-plane or out-of-plane. Fig. 8.4 shows calculated gate control of the tunneling

current versus gap size at fixed β of 30 for the case of increasing gap size with gate voltage.

Gap of around 200 nm was created in the TiW fixed-fixed bridge with forced breaking by 1 μm probe tip (Fig. 8.5). Resonance spectra of the microbridge and the cantilever (after creating tunneling gap), shown in Fig. 8.6, were tested inside a 10 mT vacuum. It can be seen that the resonance frequency of the cantilever is around one-third of the bridge with the same length, which can be explained as the result of bridge stress releasing and the theory of mechanical spring constant calculation.

Tunneling current I-V plot of the device with no gate control is shown in Fig. 8.7, along with theoretical I-V based on Fowler-Nordheim equation with parameters of: $\beta = 23$, $A_{FN} = 1.54 \times 10^{-6}$, $B_{FN} = 6.87 \times 10^{7}$, $\phi = 4.5$ V.

Fig. 8.8 shows the shifting of I_{ds}-V_{ds} curve with different gate controls, in which larger gate voltage resulted in smaller drain-source current, meaning that the gap was made larger by gate actuation. The transconductance as a function of V_{ds} is shown in Fig. 8.9. It can be seen that around $V_{ds} \sim 12$ V, the absolute value of transconductance becomes very large due to the exponential rise in the Ids. This device can also operate with very low power consumption and since it does not have metal-metal hot contact, it is expected to last much longer than MEMS DC switches.

8.3 In Vivo Brain Interfacing System Implantation

To implant the MEMS wireless system inside the brain, special consideration should be given to device packaging. First of all, like almost all MEMS devices, hermetic packaging is required to keep the necessary vacuum conditions inside the chip. The high

quality factor of the MEMS resonator relies on good hermetic packaging. Secondly, the device package needs to have good biocompatibility in order to reside inside the organism without damaging the surrounding tissues. PDMS silicone rubber is a good choice. It is transparent, nontoxic and has recognized biocompatibility for human implantation [3]. Therefore, hermetic MEMS device packaging covered with PDMS silicone rubber will be the focus of in vivo brain interfacing system implantation.

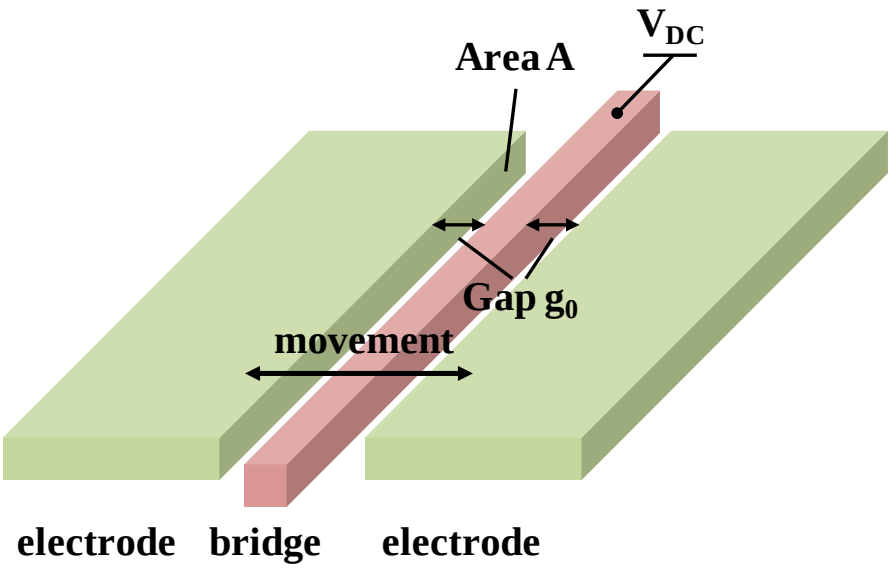

Fig. 8.1. Structure of MEMS fixed-fixed bridge lateral resonator.

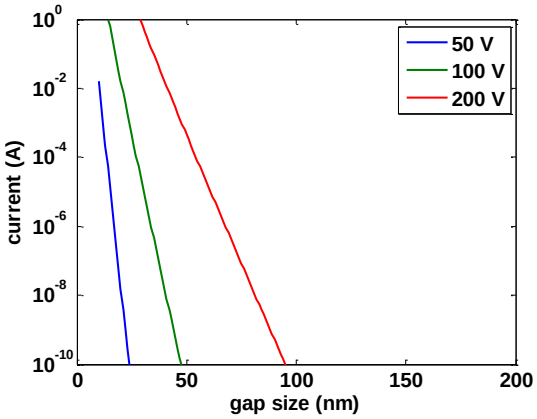

(a)

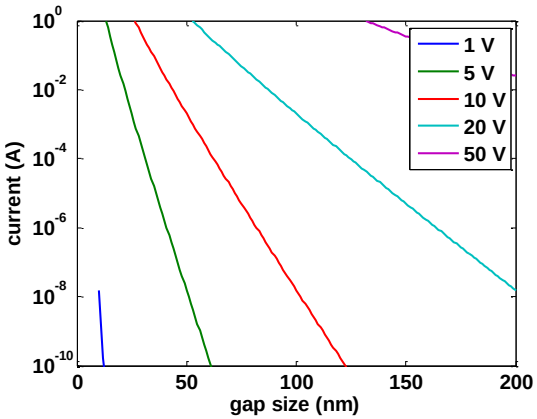

(b)

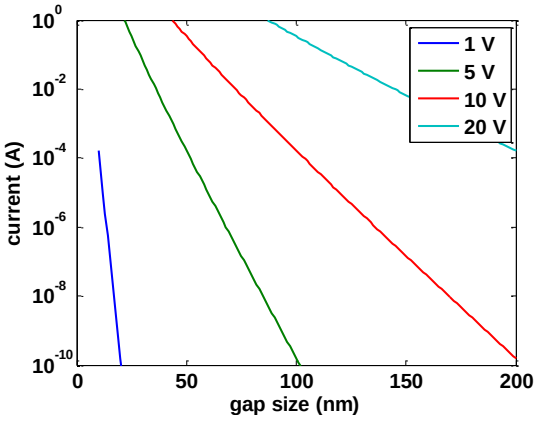

(c)

Fig. 8.2. Tunneling current versus gap size at different voltages for 5 μm wide, 1 μm thick gap, with a) β = 1; b) β = 30; c) β = 50.

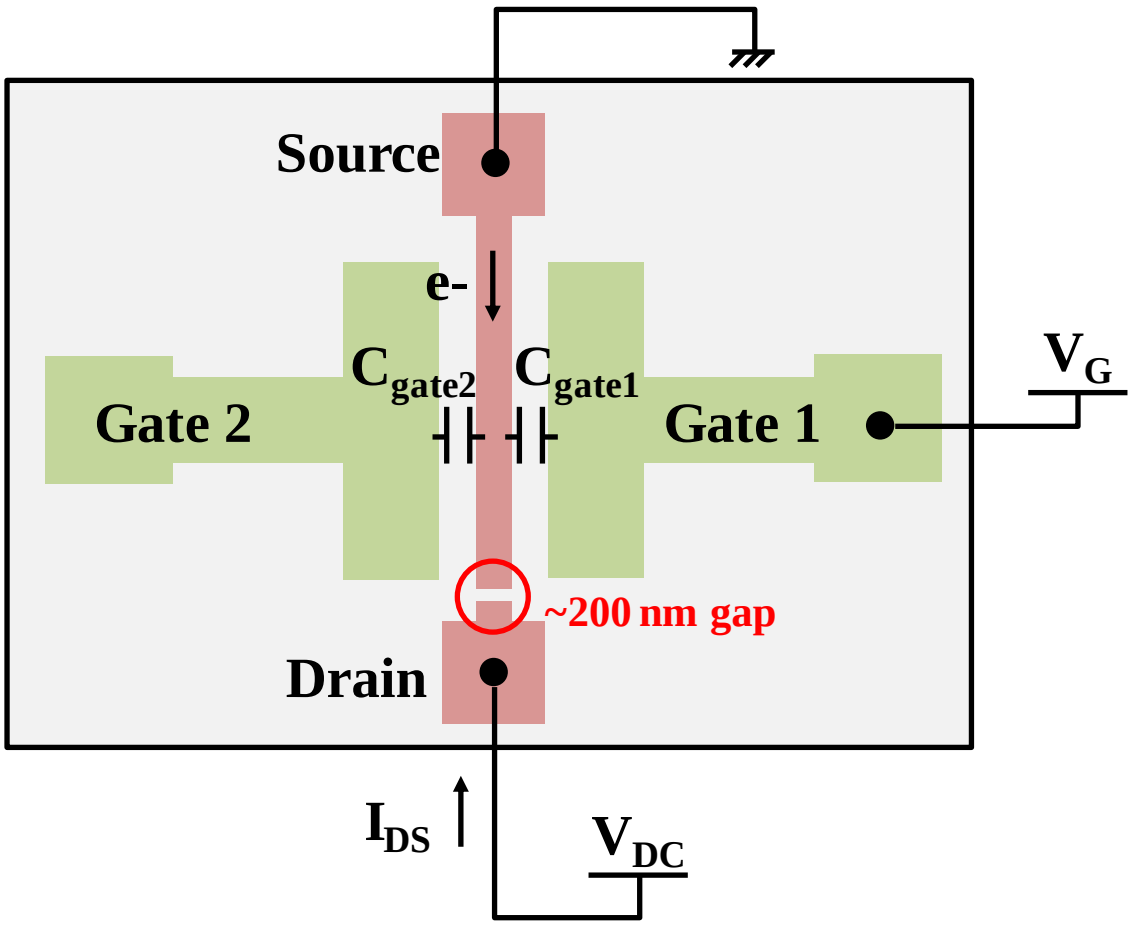

Fig. 8.3. DC Schematics of the MEMS tunneling current (MTC) amplifier.

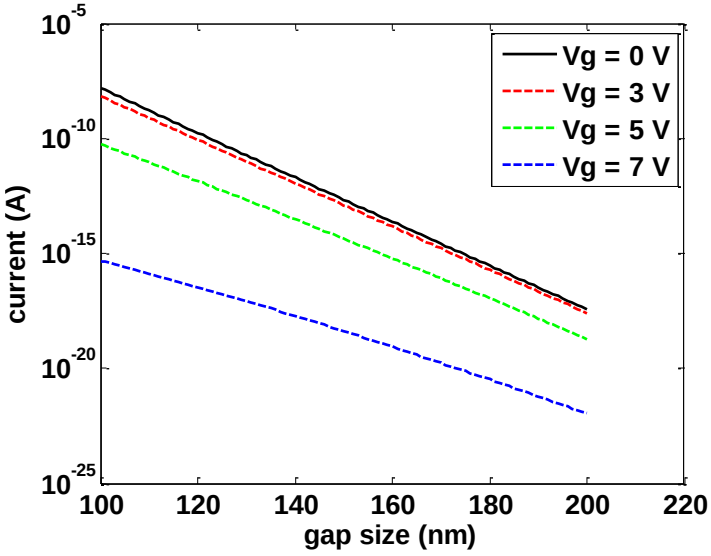

(a)

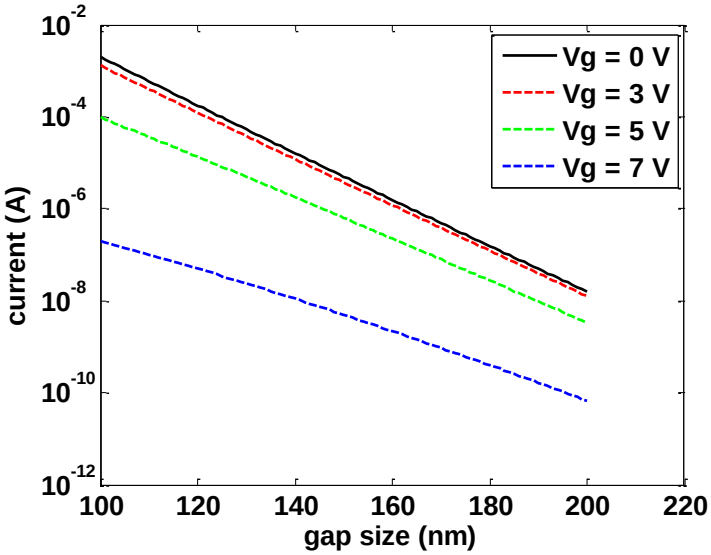

(b)

Fig. 8.4. Tunneling current versus gap size at different gate voltages for 5 μm wide, 1 μm thick gap, with fixed β of 30, with a) V_{DC} = 10 V; b) V_{DC} = 20 V.

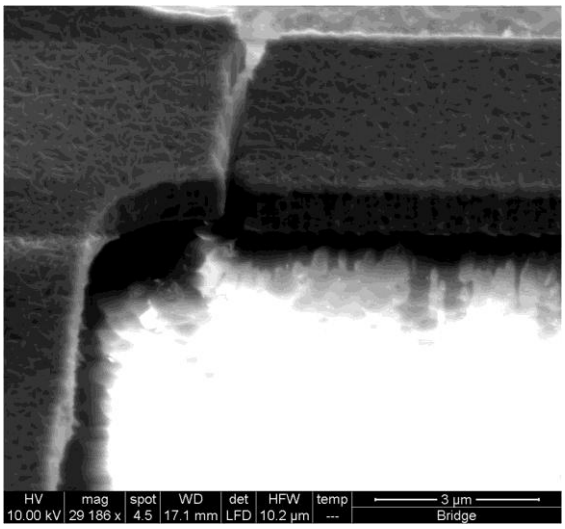

(a)

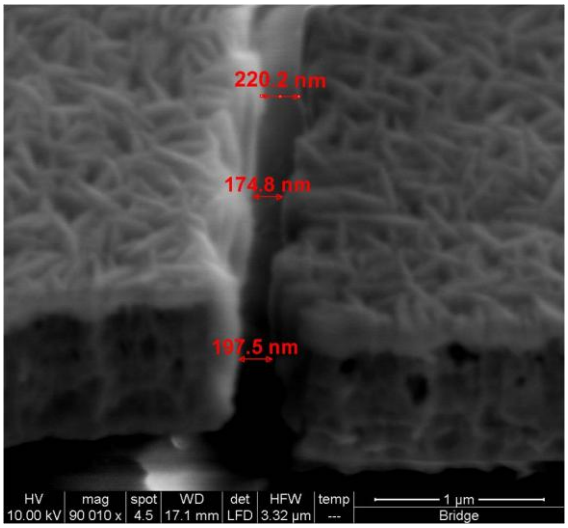

(b)

Fig. 8.5. SEM pictures of gap features of MEMS bridge. a) 200 nm gap for tunneling current creation. b) Zoomed-in SEM of the gap.

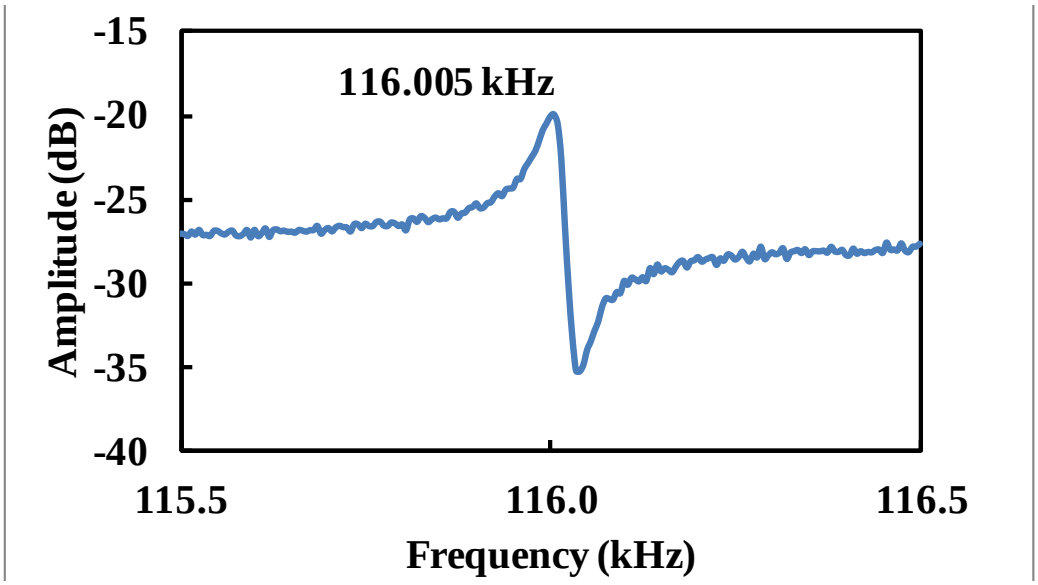

(a)

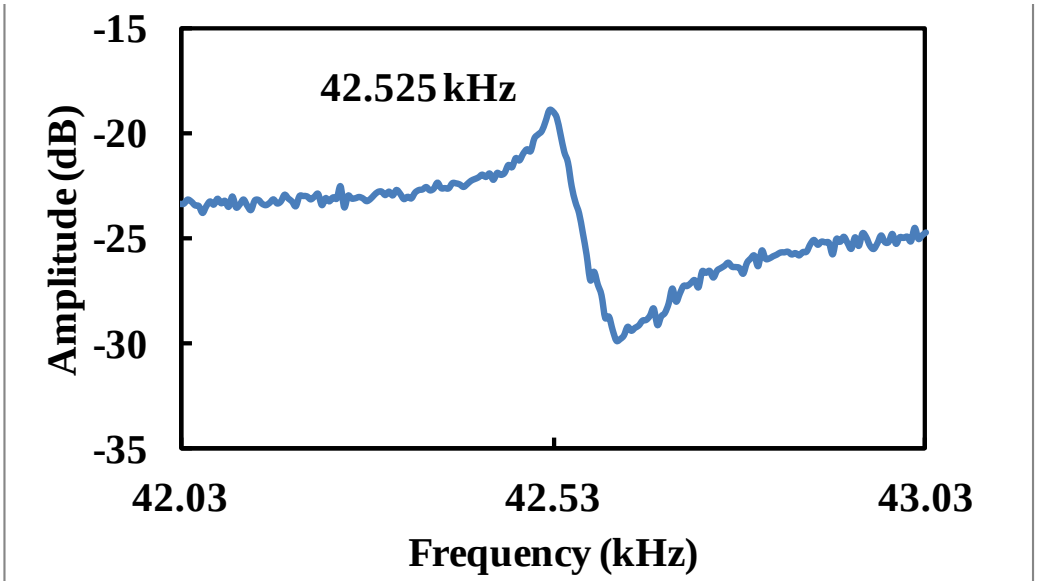

(b)

Fig. 8.6. MEMS device resonance tested inside 10 mT vacuum. a) 500 µm long bridge. b) 500 µm long cantilever.

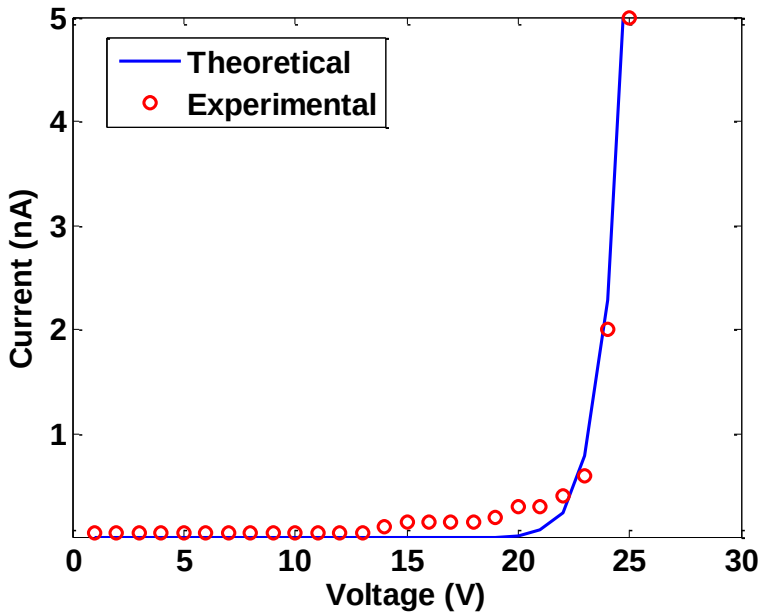

Fig. 8.7. Experimental and theoretical (Fowler-Nordheim) I-V of the MTC at $V_g = 0$ V.

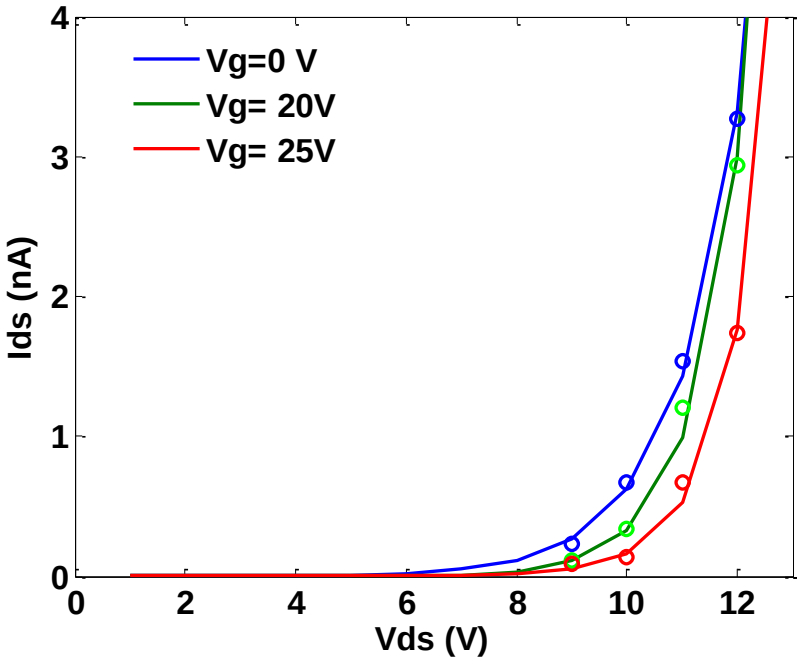

Fig. 8.8. I_{ds}-V_{ds} of the above MTC as a function of gate voltage.

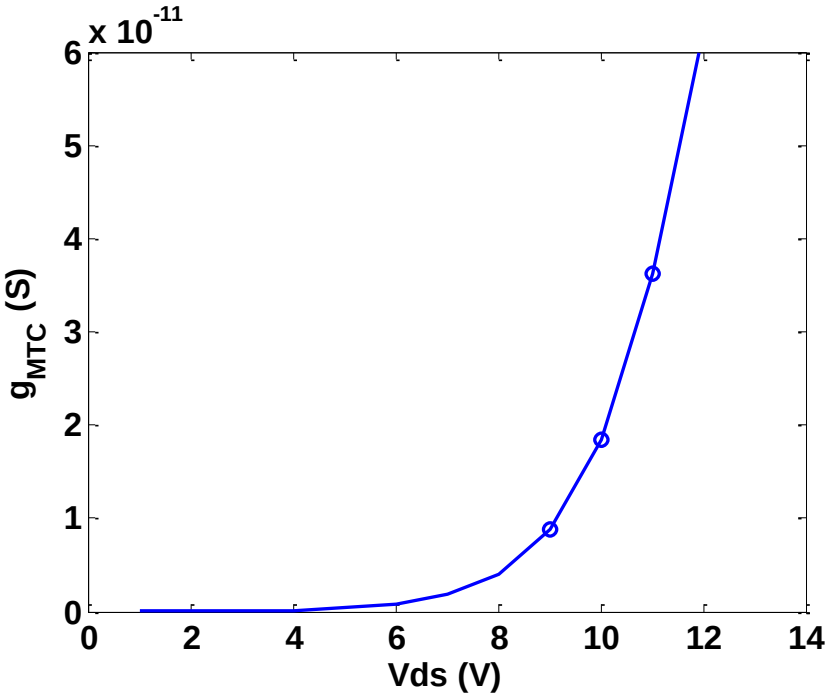

Fig. 8.9. Transconductance as a functioin of Vds of the above MTC.

8.4 References

[1] D.B. Go and D.A. Pohlman, "A mathematical model of the modified Paschen's curve for breakdown in microscale gaps," *Journal of Applied Physics*, Vol. 107, No. 10, pp. 103303, 2010.

[2] W.S. Boyle and P. Kisliuk, "Departure from Paschen's law of breakdown in gases," *The Physical Review*, Vol. 97, No. 2, pp. 255-259, 1955.

[3] B.D. Ratner, A.S. Hoffman, F.J. Schoen and J.E. Lemons, *Biomaterials Science: An introduction to Materials in Medicine (2nd Edition)*, Elsevier, 2004.

APPENDIX

EXPRESSIONS DERIVATIONS OF MAGNETIC FLUX THROUGH A COIL BY A MAGNETIC DIPOLE

This section will derive the expressions of magnetic flux received through a large coil (called coil 1) generated by a very small coil (called coil 2). Coil 2 can be considered as a magnetic dipole if $R_2 \ll R_1$.

It is know from classical physics that the magnetic flux density produced by a single turn magnetic dipole is

$$\boldsymbol{B}(\boldsymbol{r}) = \frac{\mu_0}{4\pi}\left(\frac{3\boldsymbol{r}(\boldsymbol{m}\cdot\boldsymbol{r})}{r^5} - \frac{\boldsymbol{m}}{r^3}\right) \tag{A.1}$$

where $\boldsymbol{r}$ is the vector pointing from the dipole to the specific location, $\boldsymbol{m}$ is the magnetic moment $\boldsymbol{m} = I \cdot \boldsymbol{S}$, with I the current value and $\boldsymbol{S}$ the area vector of the magnetic dipole (with direction perpendicular to the area surface). For the case where the two coils are parallel to each other, the magnetic flux received by coil 1 will be the integration of the perpendicular portion of $\boldsymbol{B}(\boldsymbol{r})$ (the direction of the area vector $\boldsymbol{S}$) over the area of coil 1

$$\phi = \int_0^{R_1} B(r)_{Zdirection} 2\pi R_k dR_k \tag{A.2}$$

where

$$B(r)_{Zdirection} = \frac{\mu_0}{4\pi}\left(\frac{3r\left(I\pi {R_2}^2 r\frac{\sqrt{r^2-{R_k}^2}}{r}\right)}{r^5}\frac{\sqrt{r^2-{R_k}^2}}{r} - \frac{I\pi {R_2}^2}{r^3}\right)N_2 \tag{A.3}$$

considering that the number of turns for coil 2 is N_2.

With all the information, expressions of magnetic flux ϕ received by coil 1 can be derived

$$\begin{aligned}
\phi &= \int_0^{R_1} B(r)_{Zdirection} 2\pi R_k dR_k \\
&= 2\pi\frac{\mu_0}{4} I{R_2}^2 N_2 \int_0^{R_1} \frac{1}{r^3}\left(2 - \frac{3{R_k}^2}{r^2}\right) R_k dR_k \\
&= 2\pi\frac{\mu_0}{4} I{R_2}^2 N_2 \int_0^{R_1} \frac{1}{\left({R_k}^2+{Z_{12}}^2\right)^{\frac{3}{2}}}\left(2 - \frac{3{R_k}^2}{{R_k}^2+{Z_{12}}^2}\right) R_k dR_k \\
&= 2\pi\frac{\mu_0}{4} I{R_2}^2 N_2 \frac{{R_k}^2}{\left({R_k}^2+{Z_{12}}^2\right)^{\frac{3}{2}}}\Bigg|_0^{R_1} \\
&= \frac{\mu_0 I{R_2}^2 N_2 \pi {R_1}^2}{2\left({R_1}^2+{Z_{12}}^2\right)^{\frac{3}{2}}}
\end{aligned} \tag{A.4}$$

where Z_{12} is the distance between the two coils. Equation (A.4) is the expression for magnetic flux through coil 2 generated by coil 1.

With the expression for magnetic flux ϕ, output voltage expressions can be obtained very easily with theory of magnetically coupled circuits. If coil 2 is the transmitter, and coil 1 is the receiver, then

$$M_{12} = N_1\frac{d\phi_{21}}{di_2} \tag{A.5}$$

$$v_{out} = v_1 = M_{12}\frac{di_2}{dt} \tag{A.6}$$